VOID FORMATION IN COPPER AND SELENIUM ION IRRADIATED MOLYBDENUM

by

RICHARD STEVEN CHERNOCK

B.S. Brown University, 1973

Submitted in partial fulfillment of the requirements
for the degree of
MASTER OF SCIENCE IN MATERIALS ENGINEERING
at the
Massachusetts Institute of Technology
September 1978

Signature of Author ....Signature redacted........
Department of Materials Science and Engineering
August 11, 1978

Certified by ......Signature redacted....................
Thesis Supervisor

Accepted by ....Signature redacted.......
Chairman, Departmental Committee on Graduate Students

ABSTRACT

VOID FORMATION IN COPPER AND SELENIUM ION IRRADIATED MOLYBDENUM

by

RICHARD STEVEN CHERNOCK

Submitted to the Department of Materials Science and Engineering on August 11, 1978 in partial fulfillment of the requirements for the degree of Masters of Science.

Molybdenum samples were bombarded with copper and selenium ions as a part of a round-robin study of the effects of dissimilar ion irradiation in molybdenum. The samples were irradiated to nominal damage levels of 2 and 20 dpa with 5 MeV ions in a tandem Van der Graaf accelerator at a temperature of 900°C (.4 Tm).

A sample preparation technique was developed to examine the void structure at the peak damage depth ($\sim .75\mu$) in a transmission electron microscope. This involved the use of a pulsed electropolisher as well as interferometric microscopes for calibrated front surface removal. Electron microscopy was performed with the aim of characterizing the resulting void distributions. The foil thickness was measured with a stereo parallax technique and the void size distribution with a Zeiss particle size analyzer. The results of the void distribution characterization are tabulated within, as well as characteristic micrographs and distribution curves. This size distribution was found to have a mean value of $\sim 40\text{Å}$. The void number densities ranged from $1.83\text{x}10^{22}$ to $1.62\text{x}10^{23}$ voids/m^3, with a void volume fraction from .232% to 1.38%.

Results of theoretical calculations of void nucleation rates are given and compared favorably with the experimental data. Calculations of the damage and bombarding ion concentrations versus depth are also described.

Thesis supervisor: Kenneth C. Russell
Title: Professor of Metallurgy

TABLE OF CONTENTS

TABLE OF CONTENTS (Cont'd.)

TABLE OF CONTENTS (Cont'd.)

LIST OF FIGURES

LIST OF FIGURES (Cont'd.)

LIST OF FIGURES (Cont'd.)

LIST OF TABLES

ACKNOWLEDGEMENTS

The author wishes to thank Professor Kenneth C. Russell for his advice and guidance which greatly assisted this project. Professor John Van der Sande gave much needed help on electron microscopy, without which this could not have been completed. Both Dr. A. J. Garrett Reed and Mr. Robert Allen assisted greatly in teaching the practial details of electron microscopy, as well as pointing out the idiosyncracies of their respective microscopes.

Dr. J. A. Sprague is to be thanked for his help with the problems encountered in configuring the interferometric electroplisher. Mr. Manfred Lichtensteiger was very helpful in demonstrating the use of the Zeiss interferometer microscope, an essential instrument in the specimen preparation. When this broke down, Professor August F. Witt gave much assistance in arranging a substitute. Mr. F. Fitzgerald of Draper Laboratories generously donated time for the attempt to use the Dektak surface profilometer.

The author also wishes to extend his appreciation to Linda Sayegh for her assistance in typing this report.

CHAPTER 1

INTRODUCTION

A topic of primary concern in the area of reactor design is that of materials integrity. Materials in the core will be subjected to an intense neutron flux at temperatures up to 650°C. For thermal reactors, the main problems encountered have been: corrosion, irradiation creep and irradiation embrittlement. The initial liquid metal breeder reactor designs took these factors into account. Then, in 1967, Cawthorne and Fulton (1) reported a new irradiation induced phenomenon--macroscopic swelling due to void formation--which has serious consequences in both breeder and CTR design philosophies.

The core of a Liquid Metal Fast Breeder Reactor (LMFBR) will be subjected to a high neutron fluence in a liquid sodium environment at temperatures ranging to above 650°C. It has been experimentally found that the temperature regime for void swelling is from .3 - .55 of the melting temperature for most metals. Unfortunately, the metals originally chosen for structural components, primarily austenitic stainless steels--types 304, 316, 321--fit the above temperature requirements and exhibit large degrees of irreversible swelling at reactor operating temperatures.

A good example of the severity of the problems caused by the swelling of stainless steel is the bowing of fuel assemblies in the original (bottom restraint only) core design. The degree of swelling is a strong function of both fluence and temperature. Radial flux and temperature distributions in a typical core resemble chopped cosine curves with the maximum coinciding with the centerline. It is clear that a fuel assembly with a different flux and temperature on opposite sides will swell differentially--leading to bowing. It has been estimated (2) that the fluence variation across a subassembly in a core edge position is such that the peak doses on opposite faces of the wrapper are 52 and 19 displacements per atom (dpa) after two years. Fig. 1 shows the expected unrestrained bowing at end of life, ignoring any mechanical interactions between components.

A more realistic estimate (2), allowing mechanical interactions, results in about 25 mm deflection at the shoulder. A maximum gap of 5 mm exists at this level. Clearly, this deformation must be taken into account in order to allow removal of the fuel assemblies. By far, the most attractive technique to resolve the LMFBR core problem is to mitigate swelling.

The controlled thermonuclear reactor (CTR) poses even more serious demands on materials--especially those in the first wall. The neutron spectrum from the D-T fusion reaction is very heavily peaked at 14.1 MeV--a much higher energy than in an LMFBR. The first wall will not only be subjected to a 14 MeV neutron flux of about $4x10^{14}$ n/cm^2 sec (5), but simultaneously a flux of less energetic neutrons, particles from both the plasma and blanket and photons. The operating temperature of the first wall will be limited primarily by what the materials can handle. Refractory metals, such as molybdenum, pose an attractive partial solution. By raising the melting point of the material, the lower limit of the temperature regime for void swelling is also raised. In the case

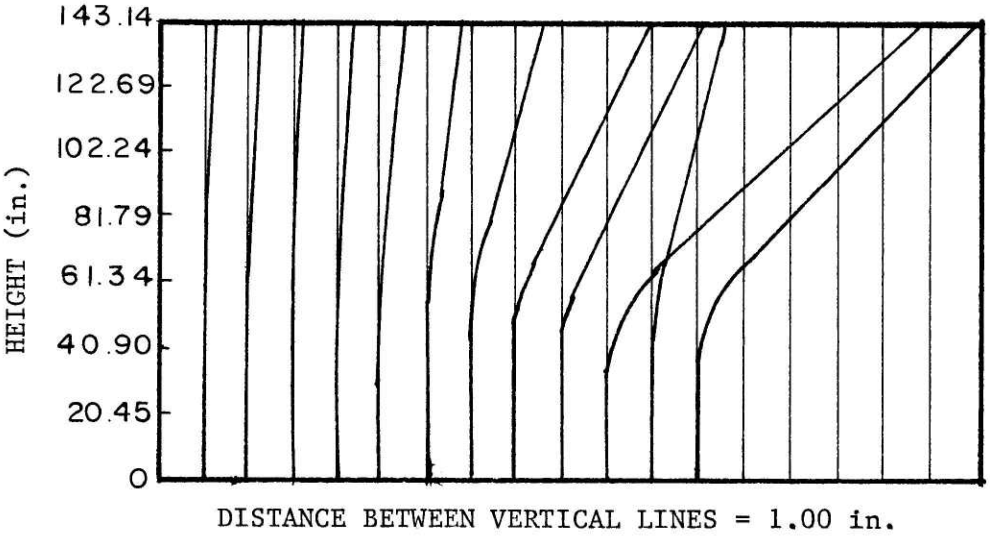

Figure 1 Free bowing of fuel assemblies due to differential elongation

of molybdenum (Tm=2883°K), the lower limit would be expected to be in the vicinity of 590°C. Even in view of this, it would be naive to believe that void swelling would not be encountered. A better knowledge of the swelling behavior of first wall candidate materials--especially the refractories--would be very helpful.

Since no type of CTR has yet been made operational, experiments on void swelling must necessarily be simulations of the expected conditions. Of the irradiation sources available--neutron, ion and electron--it would at first seem that neutrons would be the most suitable. Unfortunately, this type of irradiation suffers from a number of serious drawbacks. The samples often become highly radioactive, requiring hot cell facilities to process them after exposure. This makes post-irradiation testing difficult. Instrumenting the exposure is also difficult, in that the flux will affect many of the devices used to monitor the samples.

Exposure to a CTR spectrum is especially difficult, as very few facilities exist that produce 14 MeV neutrons. As would be expected, time on these facilities is valuable, making long term tests impractical, if not impossible. Another complication is that the neutron flux in these test facilities is about three orders of magnitude lower than that projected for the first wall (5), extending tests to a reasonable fluence beyond acceptable time limits.

Charged particle accelerators have seen wide use in the simulation of neutron damage (5-12), since they overcome many of the above mentioned difficulties. There is little, if any, induced radioactivity, so the samples may be handled directly after testing. The particle beam is well defined, so that there are minimal problems with the instrumentation.

Nearly all of the exposure variables are controllable. A major advantage is the markedly higher displacement rate--as much as three orders of magnitude higher (6)--requiring shorter, more reasonable exposure times.

Of course, there are drawbacks involved in charged particle simulation. Foremost amongst these is the difficulty of accurately correlating the results obtained with those from neutron exposures. The interaction of charged particles with the sample is very different than for neutrons. Not only is the collision process of a different nature, but the resulting damage distribution is also different. As yet, there is no accurate way to reconcile these differences, but some correlation schemes have evolved that are useable.

The last mentioned simulation technique--electron bombardment--has one very attractive feature. It is typically performed in a high voltage electron microscope (HVEM), allowing the evolution of a damage structure to be observed in real time. Once again, the damage rate is much higher than exists in a reactor. The major drawback of this technique is what makes it marginally useful in simulating neutron damage. Due to the low mass (and relatively low energy--typically 1 MeV) of the electrons, each contributes at most two displacements. Comparing this to approximately two hundred displacements per neutron, it is obvious that the damage production is very different. The major use of this technique is to observe the formation of the damage structure, attempting to only loosely correlate the dose to neutron terms.

The present experiment involving the irradiation of molybdenum by copper and selenium ions is part of an attempt to increase the available knowledge of charged particle simulation of neutron damage. Until this program, there had been no attempt to correlate not only ions with neutrons, but also the effects of different ions bombarding a given material. Attempts were made to standardize the irradiation conditions as much as possible, in order to have a basis for comparison. Molybdenum was chosen as the material to be studied, due to its attractiveness for CTR applications.

CHAPTER 2

THEORY

2.1. Radiation Damage Structure

Before mentioning void formation, a brief summary of the irradiation damage structure is necessary. An irradiation damage structure, as referred to here, is defined as a deviation from perfect crystalline structure caused by incident, energetic particles. This deviation is caused by interactions between the incident particles and lattice atoms. In non-fissile materials, each interaction will have one of three possible effects (13, 14)--thermal spikes, atomic displacements or transmutations--depending on the amount and type of energy transfer. By the simple model of Kinchen and Pease, if the energy transferred in an elastic collision is below a threshold displacement energy (E_d), a thermal spike will occur--an excitation of the vibration of the atoms in a localized volume surrounding the collision event. Although this doesn't create a damage structure, it may provide thermal activation energy for other processes.

If the energy transferred is above E_d, the struck lattice atom is irreversibly ejected from its lattice position (termed a Primary Knock-On-Atom - PKA). This PKA moves through the lattice and is capable of creating further displacements and thermal spikes. Clearly, what was stated above for the incident particle is now true for PKA's with the exception of a differing interaction mechanism due to the charge. When the energy of the colliding particle decays sufficiently for its mean free path to approach the interatomic spacing, a displacement cascade is created--a region where nearly every atom has been displaced at least once. Calculations by Brinkman (15) and Beeler (16) have shown that a displacement cascade consists of a vacancy rich core surrounded by an interstitial rich mantle--in part due to correlated collisions.

The third type of interaction involves non-elastic collisions, nuclear reactions with the matrix material forming transmutation products, as well as (n,α) reactions forming helium. The latter reaction has the higher importance, as helium has a very low solubility in most materials causing the formation of small gas bubbles, although small quantities of other products may have a significant effect on void formation. These bubbles will occur mainly in CTR and LMFBR environments due to the higher energy neutron spectra encountered. It is suspected (6) that this helium plays an important part in initially nucleating voids which subsequently grow by vacancy condensation.

The major effect of irradiation on crystalline materials is the creation of Frenkel pair defects, resulting in a supersaturation of point defects. These point defects can coalesce into stable aggregate structures. For example, the free energy of formation of a divacancy is less than twice the free energy of a mono-vacancy. Furthermore, a cluster of three or more vacancies is thought to be sufficient to be immobile. The types of defect aggregates that can be formed are as follows: (mono, di, tri, ...) vacancies, (mono, di, tri, ...) interstitials, voids, gas bubbles, disk-shaped cavities, faulted dislocation loops, perfect dislocation loops and stacking fault tetrahedra.

2.2. Void Nucleation and Growth

During irradiation, a large number of atoms are displaced from their normal lattice sites, creating Frenkel pair defects. A large majority of these defects recombine almost immediately. Those which surve this process migrate through the matrix and are lost by either recombination or voids. It is these vacancies which migrate to the voids (or to void embryos at an earlier stage) that are responsible for void growth.

In most metals, the temperature regime for void swelling extends from ∿.3Tm to ∿.55Tm (17). Below this range, the vacancy mobility is low. Due to the much higher mobility of interstitials, recombination is a much more likely fate for a vacancy than its arrival at a sink. At temperatures above .55Tm, the thermal vacancy concentration is larger than that produced by irradiation, removing the necessary condition of vacancy supersaturation required for void nucleation.

2.2.1. Void Nucleation

A large number of mechanisms have been proposed to explain the nucleation of voids (4). These include nucleation on pre-existing sites (20), processes involving displacement spikes (21), nucleation on gas bubbles (or with the assistance of gas atoms) (1, 22, 23) and homogeneous nucleation. Although each may apply in certain situations, it is clear that no one of these mechanisms can be solely responsible for all cases of nucleation. For example, electron irradiation is capable of producing voids (7) although no displacement cascades are produced. Similarly, many studies (such as the present one), have produced voids with no gas present. A nucleation theory allowing all of these mechanisms to contribute (where appropriate) would be the most sensible approach to the problem.

Russell (19) has formulated such a theory. Void nucleation is approached through irreversible thermodynamics, considering the time rate of change of the concentration of a species in the appropriate phase space. Characterizing the void by the number of vacancies (n) and impurity atoms (x) that it contains, consideration of the appropriate fluxes results in the following master equation:

$$\frac{\partial \rho(n,x)}{\partial t} = \int\int\{ \rho(n',x')\ \omega(n,x/n',x') - \rho(n,x)\omega(n',x'/n,x)\partial n'\partial x' \quad (2.1)$$

where $\rho(n,x)$ = number density of voids of n vacancies and x impurity atoms

$\omega(n,x/n',x')$= frequency with which an (n',x') void becomes an (n,x) void and

$\omega(n',x'/n,x)$= frequency of the reverse transition.

Only transitions involving single vacancies and gas atoms will be considered.

Since this study does not involve preinjection of gas, homogeneous nucleation in the absence of gas would be the approach to consider. With inert gas included, a complicated nodal line analysis would be needed (19). Here, Eqn. 2.1 is used as a starting point, with the void flux in size space ($J_n(n)$) as the important parameter. This is related to the number density of (n) voids by:

$$\frac{\partial \rho(n)}{\partial t} + \frac{\partial J(n)}{\partial n} = 0 \qquad (2.2)$$

resulting in:

$$J_n(n) = \beta_v^\circ \, n^{1/3} \, \rho'(n) \, \frac{\partial[\rho(n)/\rho'(n)]}{\partial n} \qquad (2.3)$$

where:

$$\rho'(n) \equiv N\exp(-\Delta G'(n)/RT) \qquad (2.4)$$

$$\Delta G'(n) = kT \sum_{j=n}^{n} \ln(\beta_i^\circ/\beta_v^\circ + \exp(\frac{1}{kT}\frac{\partial \Delta G^\circ(j)}{\partial j})) \qquad (2.5)$$

= activation barrier for void nucleation.

The steady state nucleation rate is given by:

$$J_s = Z'\beta_v^\circ \, n_K'^{\,1/3} \, N \exp(-\Delta G_K'/RT) \qquad (2.6)$$

where Z' = Zeldovich factor, $\Delta G_k'$ = peak height of the activation barrier and subscript "k" represents quantities evaluated at the critical void size (max ΔG'(n)). For homogeneous nucleation, the effect of excess interstitials on $\Delta G_k'$ is modest when $S_v(1-\beta_i^\circ/\beta_v^\circ) \gtrsim 2$ and may be ignored. This results in a simple expression for the peak free energy:

$$\Delta G_k' = (16\pi\Omega^2\gamma^3)/3(kT)^3(\ln S_v)^2 \qquad (2.7)$$

where Ω = atomic volume, γ = surface energy, S_v = vacancy supersaturation (C_v/C_v^e). Various pre-exponential factors in Z' and β_v° combine to yield $\sim$K, so that

$$J_s^\circ = (K/\Omega)\exp(-16\pi\Omega^2\gamma^3/3(kT)^3(\ln Sv)^2 \qquad (2.8)$$

where K = the atomic displacement rate. This expression for the steady state nucleation rate is relatively easy to work with, the only term requiring evaluation is the vacancy supersaturation. This may be computed by the methods of Brailsford and Bullough (24) by considering the rate of loss of vacancies to sinks in the material.

Of more practical interest is the terminal void number density, since this will be the number of voids present in the material after the irradiation exposure. This cannot be arrived at by simply multiplying the steady state nucleation rate by the irradiation time, since nucleation only occurs during part of the irradiation. There is a necessary incubation time for the start of nucleation and at some point in their growth, the voids will stop any further nucleation. This will be due to an increase of the sink strength for vacancies, of which the void contribution is:

$$k_c^2 = 4\pi \bar{r}_c \rho_c \tag{2.9}$$

where $\bar{r}_c$ = average void radius and ρ_c = total void number density. In order to strictly compute the cut-off of void nucleation, a time dependant nucleation rate must be considered. This would make the calculations very involved and appropriate only for the material parameters used.

By assuming steady state conditions hold during irradiation (β_i°, β_v°, J_s and non-void sink densities constant), the situation simplifies greatly. For negligible thermal vacancy emission from voids, the void growth rate is given by (24):

$$\dot{r} = D_v C_v (1-\beta_i^\circ/\beta_v^\circ)/r \tag{2.10}$$

By consideration of a time dependant sink strength, a terminal void number density can be obtained:

$$\rho_c = J_s t = (3k_c^2/8\pi)^{2/3} \left[J_s^\circ/2D_v C_v(1-\beta_i^\circ/\beta_v^\circ)\right]^{1/3} \tag{2.11}$$

It may appear at first that the above equation is circular - $k_c^2=f(\rho_c)$, but there is an easy approach in the case of homogeneous nucleation. One may choose the void sink strength as that required to decrease the nucleation rate by a factor of ∿10. Referring to Eqn. 2.8, a vacancy supersaturation needed for this reduction may easily be calculated. Then, k_c^2 required for this lower supersaturation may be determined directly.

2.2.2. Void Growth

The growth rate of existing voids is simply a function of the difference in net arrival rate of vacancies and iterstitials. A void may grow by adding a vacancy or emitting an interstitial; shrink by adding an interstitial or emitting a vacancy. Since the vacancies and interstitials are created at an equal rate by irradiation and their attraction to voids is nearly equal, it is clear that in order for voids to grow, there must be preferential absorption of interstitials at some other sink. The stress field of a dislocation will attract an interstitial more strongly than a vacancy, resulting in a higher annihilation rate for interstitials. It has been estimated that a ratio of sink strengths (vacancy/interstitial) on the order of .9 to .99 is sufficient to allow a large amount of void growth.

As mentioned earlier, Brailsford and Bullough (24) have obtained an expression for the void growth rate:

$$\dot{r} = D_v C_v (1-\beta_i^\circ/\beta_v^\circ)/r \qquad (2.12)$$

In order to calculate the arrival rates at voids, all other sinks must be considered. These sinks include; grain boundaries, precipitate boundaries, matrix dislocations, irradiation induced dislocation loops and solute atoms. For a more detailed discussion of this, the reader should refer to Brailsford and Bullough (18, 24).

2.3. Correlation

As mentioned previously, one of the problems with simulating neutron induced damage is the correlation of the results obtained. On the atomic scale, the processes occurring during heavy ion irradiation are quite different from neutrons. The displacement rate is typically orders of magnitude higher, while the peneration depth is in terms of microns rather than centimeters. The fundamental difference between fast neutron and charged particle irradiation is the elastic scattering cross-section (6). For neutrons, the cross-section is typically $10^{-24} cm^2$ - due to the larger spatial extent of the charge interations, the cross-section for ions may be as much as six orders of magnitude higher. The most important result of this is in the mean free path between collisions. For ions, this may be as low as 100 Å, greatly reducing the range where damage is produced in the sample. Another problem stemming directly from the charge on the incident particles is the very different PKA spectrum (5). This will influence the distribution of secondary displacements.

Assuming that the obvious measures are taken in setting up the simulation--such as assuring that the required small sample size will not have a detrimental effect, the need for a correlation technique to relate the results to neutron conditions exists. Unfortunately, there is no technique available today to accurately interpret the results. Present attempts fall within the following areas: (1) comparison of damage structure, (2) comparison on a displacement basis and (3) comparison on a rate basis.

Comparison of the damage structure was used by Mitchell (9) in a study of 16 MeV proton, 14 MeV neutron and fission neutron damage in copper. As the name implies, equivalence in properties is assumed under conditions which yield equivalent structures. Although it is applicable to a limited number of comparisons without great difficulty, development of a correlation over the entire range of variables encountered would be quite laborious. Correlations would be expected to be rather poor in the case of dynamic mechanisms, as these depend on the supersaturation of point defects (not considered) as well as the damage structure.

A more sophisticated technique is based on a comparison of the total displacements (dpa) experienced by the sample. This is generally done on a theoretical basis using relations similar to those in Appendix 1, although experimentally determined cross-sections may be used. This technique suffers from a number of defects. The accuracy is certainly no greater than the theories or data used to determine the number of displacements, which can be rather poor. Correlations of this type also ignore any effects of dose rate. The formation of many different types of damage structures are strongly dose rate dependant--notably void formation and growth.

The concept of a temperature shift attempts to take displacement rate into account. This is based on the assumption that damage production at one rate will be equivalent to that produced at a different rate and temperature. Straalsund(25) has applied this concept to a simple model of void growth to find an equivalence between high and low damage rates. A simple relation for this is:

$$T_2-T_1 = (RT_2^2/Q)\ \ell n(G_2/G_1)/(1+[(RT_2/Q)\ell n(G_2/G_1)] \qquad (2.13)$$

where T_2 = the temperature associated with the free defect generation rate G_2, T_1 = the temperature associated with the free defect generation rate G_1 and Q = vacancy migration energy, assuming that the kinetics are limited by this. In order for a technique of this type to be used, the formation and growth kinetics of the appropriate structural features must be known--a difficult task, due to imprecise knowledge of the kinetics.

It would appear that the most successful correlation technique at present would be a combination of the dpa and temperature shift techniques. This would yield a correlation which approaches the real situation better than either alone. Many factors would still be left out, most notably solute trapping effects. As noted in the initial stages of the BCC ion correlation experiment (26), irradiations of molybdenum with different ions at the same damage level and damage rate resulted in appreciably different structures. The above modified technique would not handle this properly.

2.4. Electron Microscopy - Image Formation from Voids

The following discussion assumes that the reader is at least passingly familiar with the theories of image formation in transmission electron microscopy (TEM). Hirsch et al. (27) is an excellent reference source for this. The features of the cavities which produce contrast in a TEM are: (1) a region of differing electron potential and scattering characteristics from the matrix and (2) possibly strain induced in the matrix due either to the mismatch between internal pressure and surface tension or to solute segregation. The major modes of imaging cavities; mass thickness contrast, phase contrast and strain contrast; will be discussed in the following sections.

An important parameter in the discussion of contrast formation is the extinction distance (ξ_g). From the kinematical approach (27), the extinction distance represents the thickness of the sample traversed by the electron beam where all of the intensity in the incident beam has been reflected into the diffracted beam. Consideration of what happens past this point shows one of the major drawbacks of the kinematical theory. The expression for the extinction distance is as follows:

$$\xi_g = \pi V_c \cos\theta / \lambda F_g \tag{2.14}$$

where V_c = volume of the unit cell, θ = Bragg angle (for electrons, $\cos\theta \sim 1$), λ = relativistic wavelength of the electrons and F_g = structure factor for the reflection considered. Table 1 lists the extinction distances for various reflections in molybdenum.

2.4.1. Mass Thickness Contrast

Electrons which pass through a column containing a cavity traverse a smaller distance in the matrix than those which do not. Since the intensity of an electron beam is a function of the thickness of the material that it passes through, there will be a difference in intensity between columns which pass through a cavity and those which do not. The phase factor of the electron beam is also a function of the thickness of

TABLE 1

Extinction Distances in Molybdenum

REFLECTION	EXTINCTION DISTANCE (Å)
110	226
200	318
211	396
220	467
310	536
222	606
321	677
400	748

the material that it passes through, contributing to contrast. This can be avoided if the exit surface of the sample is imaged (in-focus imaging). The contributions of phase contrast will be taken up in the next section.

The first consideration (28) will be an empty, penny shaped cavity of thickness t_2. The cavity will be situated in a sample of thickness: $t=t_1+t_2+t_3$. Without going into the wave equations, the intensity of a beam passing through the perfect crystal may be expressed as:

$$I^P_{t,s} = I_{t,s}(t_1+t_2+t_3) \tag{2.15}$$

where $I_{t,s}$ refers to either the bright field intensity (I_t) or dark field (I_s). The effect of the thickness on intensity comes about primarily through absorption and scattering. The intensity of the columns passing through the cavity is given by:

$$I^B_{t,s} = I_{t,s}(t_1+t_2) \tag{2.16}$$

resulting in a contrast defined by:

$$C_{t,s} = (I^B_{t,s}/I^P_{t,s}) - 1 \tag{2.17}$$

Calculations by Rühle (28) yield the curves shown in Fig. 2, contrast versus foil thickness. The results will vary with the value chosen for the normal absorption coefficient (μ), but for the interests of simplicity, $\mu= 1/\xi_g$ was chosen. The anomalous absorption coefficient (κ) was fixed at .1. The important feature of this plot is the decaying oscillatory nature of the contrast. This shows that the appearance of the cavities will be highly sensitive to foil thickness, especially in

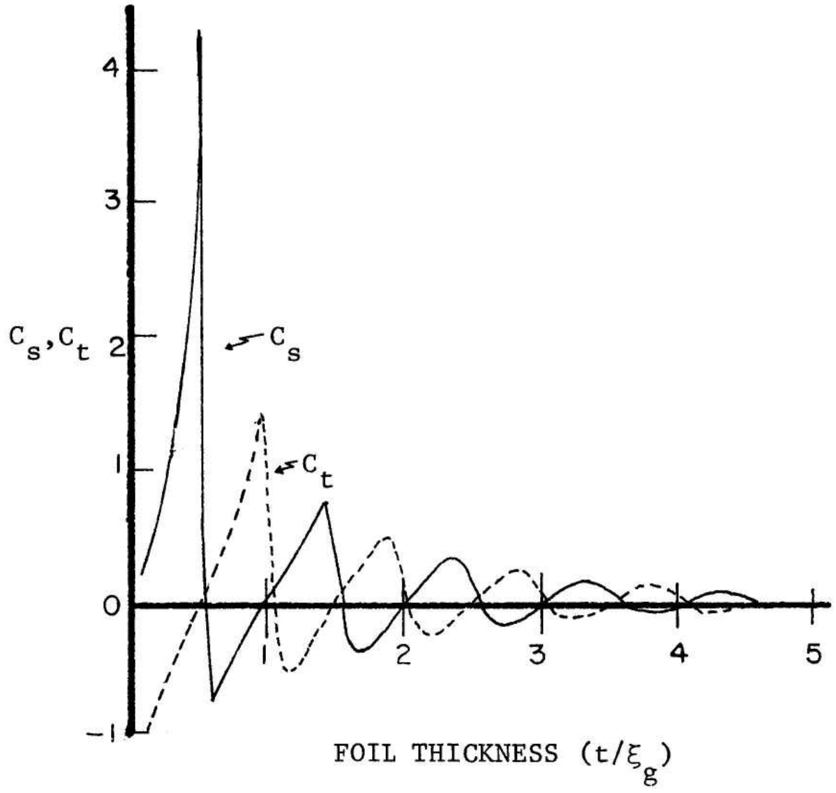

Figure 2 Dependance of void contrast on foil thickness

(thickness of void = $.1\xi_g$, $\mu = 1/\xi_g$, $w = 0$)

the thinner regions. As might be expected, the contrast is also sensitive to cavity thickness in an oscillatory manner--as shown in Fig. 3. Although these calculations apply to the void geometry mentioned above, results for any shape may be built up by choosing the appropriate portions of these curves.

The calculated contrast for a spherically shaped cavity is plotted in Fig. 4 against the reduced distance form the center ($\rho = r/R_b$) As can be seen, the contrast varies over the projection of the cavity, changing sign for some ratios between the diameter and foil thickness. In the case of a small void, there is a small negative contrast, decreasing with ρ. The large void will give a bright central region surrounded by a dark ring. Other diameters and foil thicknesses will yield different contrast curves--the one feature common to all being that the outer diameter of the projected image is equal to the true diameter of the void. In many cases, the contrast is so small that the voids are not visible, especially for small cavities or large values of the normalized extinction error (w).

2.4.2. Phase Contrast

If the sample is imaged at a point other than the lower surface (out-of-focus imagining), there may be interference between the waves emerging from the sample. If these waves have different phases, due to the differing inner potential between a void and the matrix, the interference will cause phase contrast. The mathematical description of this phenomenon is very complicated and will not be discussed here.

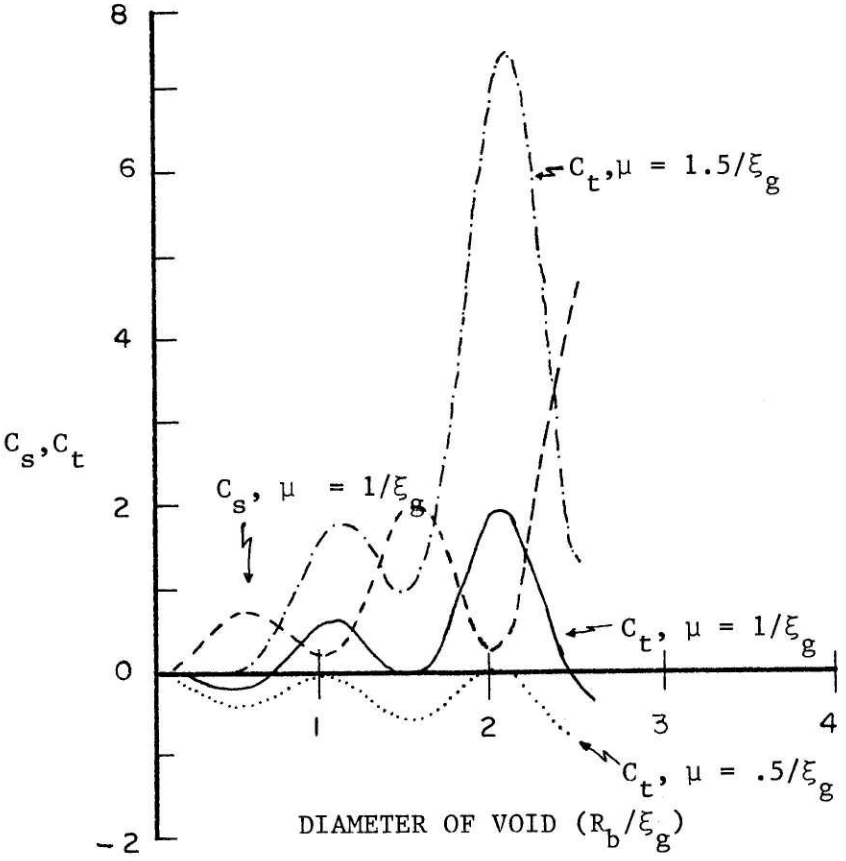

Figure 3 Dependance of void contrast on void thickness

(foil thickness = $4\xi_g$, $\mu = 1/\xi_g$, $w = 0$)

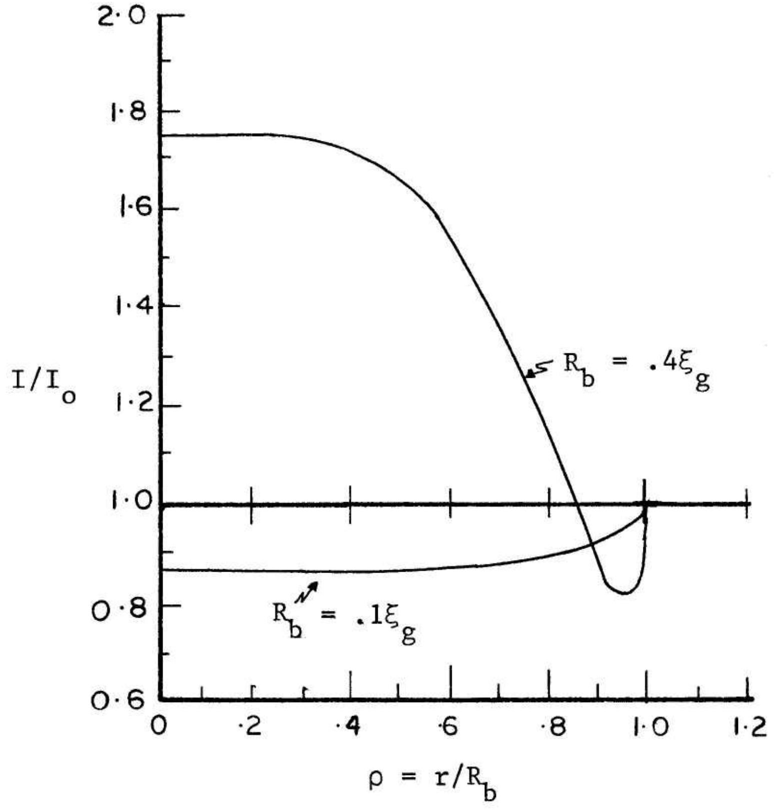

Figure 4 Contrast of spherical bubbles in mass thickness imaging conditions (foil thickness = $3.75\xi_g$, w = 0)

This difference in inner potential leads to the consideration of a refractive index to relate the wave vectors:

$$X_o = nk_o \tag{2.18}$$

where X_o = magnitude of the electron wave vector in the matrix, k_o = magnitude of the electron wave vector in vacuum (the gas may be ignored) and n = refractive index, where:

$$n = (1 + V_o/E)^{1/2} \tag{2.19}$$

V_o = mean inner potential of the metal and E = energy of the electrons. For 100 KV electrons and a mean inner potential relative to vacuum of 10 V, n is 1.00005. Assuming the interior of the void has the vacuum electron potential,

$$\lambda_{\text{void}} = 1.00005\lambda_{\text{matrix}} \tag{2.20}$$

It is clear that there may be phase differences between those beams passing through the void and those which don't, depending on the thickness of the void.

By considering the interactions of the electron wave functions on a plane other than the exit surface of the foil, Rühle has calculated the expected contrast from voids. It was found that the results varied for large and small voids (the cut-off point is at approximately .2 ξ_g). As mentioned earlier, the small voids are nearly invisible under out-of-focus conditions and large foil thicknesses. Fig. 5 shows that when imaged under out-of-focus conditions, much stronger contrast is revealed. The different curves are plotted for differing values of the focus parameter (β), where

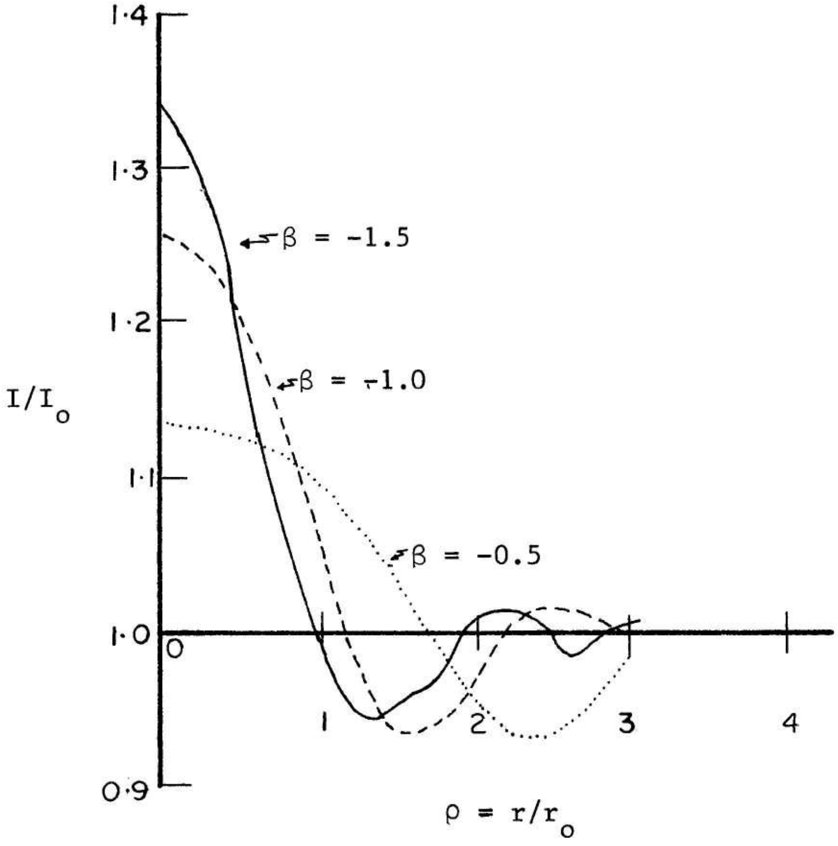

Figure 5 Contrast of small voids under phase contrast conditions ($\beta = \pi k_o R_b^2 / \zeta$)

$$\beta = \pi k_o R_B^2/\zeta \qquad (2.21)$$

R_B = void radius and ζ = defocusing distance.

As can be seen, for $\zeta < 0$, the image appears as a bright central region surrounded by a sequence of dark and bright fresnel fringes. Under most conditions, only the first fringe is visible. For the reverse focusing condition, $\zeta > 0$, the contrast will be reversed--a dark central region surrounded by a bright fringe. Fig. 5 also shows a problem in determining the actual size of the void--which feature of the image most closely represents the real diameter? Fig. 6, calculated ratios of the inner and outer diameters of the first fresnel fringe to the real diameter, shows that for cavities larger than approximately 20 Å, the inner diameter of the fringe deviates from the real diameter by less than 10%. This result also holds true for $\zeta > 0$. From this, it is clear that the size measurements should be made with the inner diameter of the first fresnel fringe.

For large voids, extinction contrast oscillations may occur, influencing the contrast produced in a way that is difficult to separate from the effects of focusing. It was found that if the sample was oriented away from strong diffracting conditions, the intensity oscillations would become invisible. Under in-focus conditions, the contrast would be formed by absorption only--producing a weak, bright region the size of the void. In out-of-focus conditions, the image formed would be largely similar to that for smaller voids. Once again, the inner diameter of the first fringe should be taken as the actual diameter.

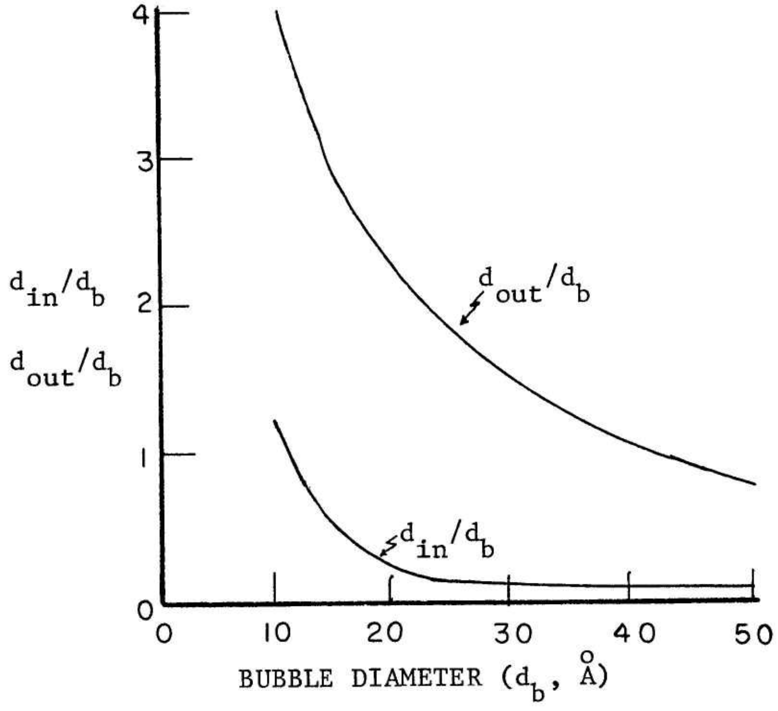

Figure 6 Ratios of inner and outer fringe diameter to true void diameter ($\zeta = -8000\text{Å}$)

2.4.3. Strain Contrast

The third type of image forming mechanism--strain contrast--will be only briefly mentioned, since it is not expected to be encountered. Features distorting the lattice of a sample would be expected to produce contrast by bending lattice planes either into or away from the diffracting conditions. This form of contrast is most visible under two beam dynamical conditions. Depending upon the amount of misfit strain and size of the void, the appearance will differ. For small defects with large misfits, black-white contrast with depth oscillation is expected. For large voids with smaller misfits, black-white contrast without oscillations is the result. Large voids would exhibit no black-white contrast under dynamical conditions, because the image is mainly due to mass-thickness contrast.

CHAPTER 3

EXPERIMENTAL TECHNIQUES

3.1. Experimental Aims and Materials

As mentioned previously, this experiment was to be a part of a round-robin ion correlation experiment. The bombarding ions-Cu^{++} and Se^{++}--were chosen because of their dissimilarity to the matrix material. Because this type of investigation was new, it was decided to adhere to the basic conditions outlined for the correlation experiment. These were as follows:

1. An irradiation temperature of 900°C.

2. A total dose of 20 dpa on half of the samples and 2 dpa on the remaining. The 2 dpa level should be at the same depth as the 20 dpa, the difference in damage level to be brought about by a reduced irradiation time.

3. The concentration of deposited ions at 20 dpa was to be less than .02% averagedover a 1000 Å section.

4. The dose rate was to be approximately 2×10^{-3} dpa/sec, within a factor of 2.

5. Displacement damage curves were to be calculated using the EDEP-1 computer code of Manning and Mueller (35) and the recommendations of HEDL-TME-73-76 (36) for dpa calculations--using a β of .8 and E_d=62 eV.

6. No preinjection of helium.

The specimens were supplied by Pacific Northwest Laboratory (PNL) precut and vacuum annealed. The foil was .007 inches thick. The vendors analysis of the original foil is given in Table 2, A vacuum anneal was given to all of the samples: 2 hours at 1600°C in a vacuum of 10^{-7} torr. An analysis of the interstitial elements after this anneal is given in Table 3.

The specimens were ground flat and mechanically polished with .3 micron alumina to produce a smooth surface for irradiation. This portion of the experiment was performed by another investigator. Surface profiles made with a Dektak stylus profilometer revealed some surface scratches as deep as 2000 Å. An attempt was made to improve the surface smoothness by electropolishing with a sulfuric acid-methanol solution. Varying conditions of voltage, current and temperature did not greatly improve the surface and in many cases made it rougher due to preferential attack at the grain boundaries. It was decided to use the foils in the as-mechanically polished state and to factor the surface roughness into the uncertainties in damage level at the region of examination.

3.2. Ion Bombardment

The irradiations had been performed at High Voltage Engineering Corporation in Burlington Mass. by another investigator. This facility is equipped with a 3MV (nominal) tandem Van der Graaf accelerator capable of providing accelerated beams of ions from hydrogen to uranium. For this experiment, 5 MeV beams of Cu^{++} and Se^{++} ions were used.

A beam of the appropriate ions is accelerated by the Van der Graaf accelerator and passes through an analyzing magnet. By careful choice of field strength and aperture size, only those ions with the correct energy (within .1%) and charge will be bent by the amount required to

TABLE 2

VENDORS CHEMICAL ANAYSIS OF Mo INGOT

ELEMENT	WEIGHT %
C	.005
O	.0005
N	.002
H	<.0001
Fe	.004
Ni	<.001
Si	.001

TABLE 3

INTERSTITIAL ANALYSIS OF MOLYBDENUM SAMPLES AFTER VACUUM ANNEAL

ELEMENT	WEIGHT %
C	<.001
O	.001
N	.001
H	.0003

pass freely down the beam tube without collisions with the walls. This monoenergetic ion beam then passes into the target chamber, bombarding the specimen.

The target was not floating above ground potential, so it was not possible to monitor beam current during irradiation. This could only be done by inserting a beam stop into the ion path and taking a current measurement from it. Temperature monitoring was performed with thermocouples embedded in the specimen holder. These thermocouples had been previously calibrated with an optical pyrometer.

3.3. Specimen Preparation

Since the aim of this procedure was to characterize the irradiation induced void structure by transmission electron microscopy, it was necessary to produce suitable samples. This required producing an electron transparent region--less than 1000 Å thick--at the desired depth with minimum deformation of the sample. Standard TEM procedures produce an electron transparent region somewhere near the center of the sample, which would not be suitable for this study, since the ion range is only on the order of 1 micron in a sample 75 microns thick.

The basic technique used to produce the samples is illustrated in Fig. 7. The front surface (ion bombarded surface) is removed to the depth of the desired damage level. This surface is then masked and the back is polished in a jet electropolisher. This results in a dished sample with a perforation in the center at the desired depth. The front surface removal is by far the most critical step. The methods considered to achieve this were: (1) real time x-ray attenuation monitoring during

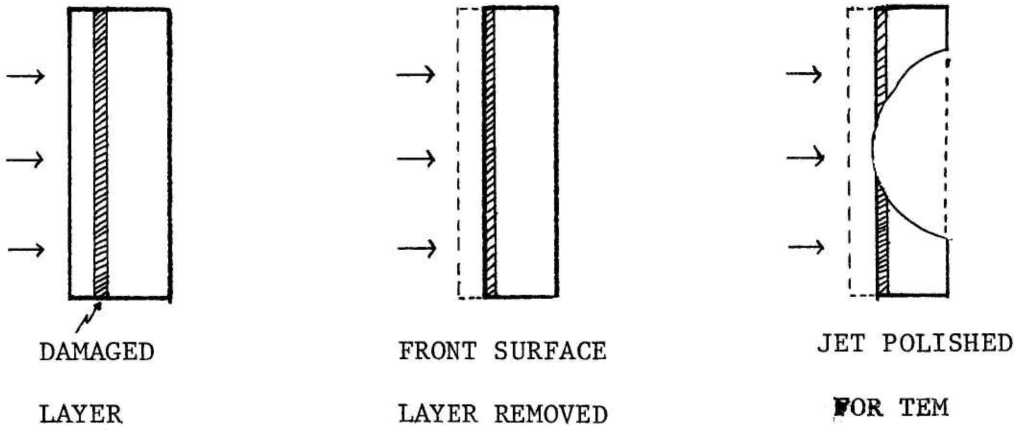

Figure 7 Basic specimen preparation technique

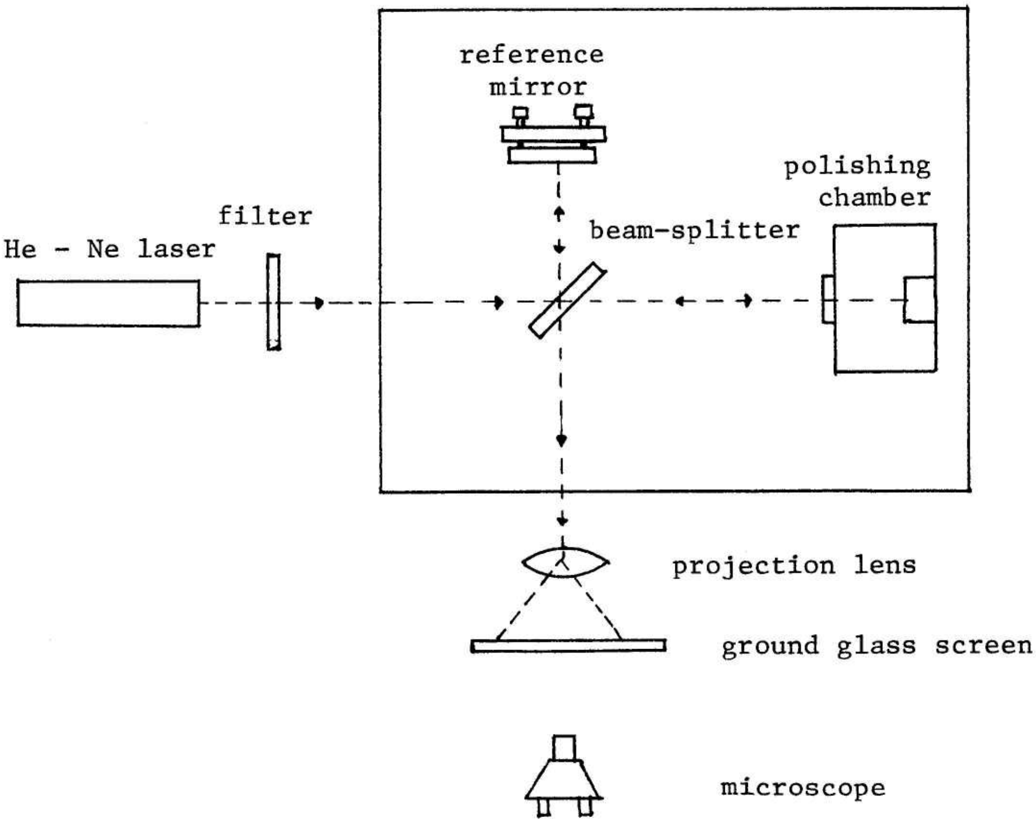

Figure 8 Laser interferometric polishing system

electropolishing, (2) vibratory mechanical polishing at a calibrated rate, (3) electropolishing at a calibrated rate, (4) real time laser interferometric monitoring during electropolishing and (5) mechanically measuring surface profile with a Dektak.

X-ray monitoring suffers from a low sensitivity with molybdenum as well as an understandable reluctance to allow electropolishing on an X-ray unit. Vibratory polishing would be very likely to introduce an artificial deformed microstructure in the sample. Electropolishing was originally through to be too variable to allow calibration with much hope of repeatability. Mechanical profilometry was not suitable due to the scratch left on the sample by the stylus and a resolution problem. If the sensitivity is set high enough to accurately measure a step height of .1 micron, a slight degree of bevel or misalignment of the sample ran the trace completely off scale. Laser interferometric monitoring overcomes many of these problems: it is a real time monitoring system capable of revealing information about the surface profile. Resolution better than 1000 Å in polishing depth should easily be achieved. An important factor in choosing this technique was its successful use by Sprague (29).

3.3.1. Interferometric Electropolisher

A diagram of the interferometer is shown in Fig.8, with the polishing chamber and sample holder shown in Figs. 9 and 10 respectively. A monochromatic beam from a He-Ne laser passes through an intensity controlling filter and is divided into two parts by the beam splitter. One beam passes through an optical flat into the polishing chamber and impinges upon the sample. When the two reflected beams recombine at the beam splitter, they interfere with each other. The difference in path

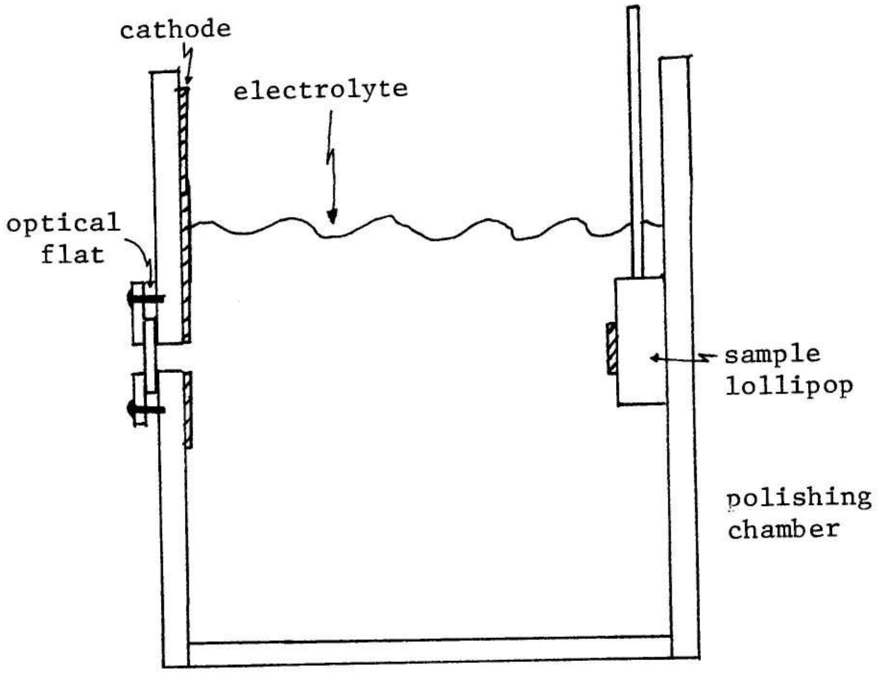

Figure 9 Polishing chamber

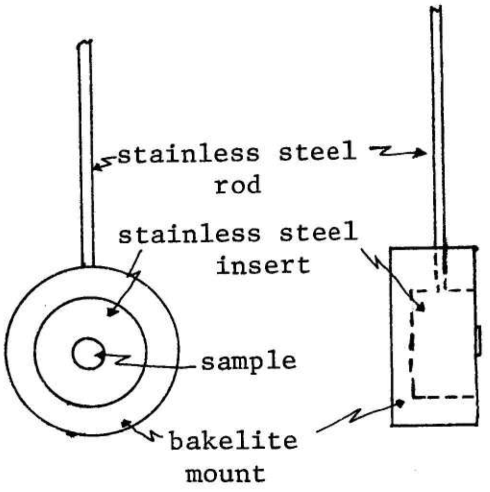

Figure 10 Sample holder

length of a particular portion of the beam determines whether the interference is constructive or destructive. This beam is expanded to an image on the ground glass screen by the projection lens. The fringe pattern is then observed through a microscope equipped with an eyepiece reticule. As the sample is polished, the front surface effectively moves away from the beam splitter--result in a longer path length, with an associated fringe shift.

This system is highly sensitive to small changes in position of the interferometer components relative to each other. Considering the vibration environment in most labs, this was an important factor in the design. A 1" thick slab of aluminum was used as a base, with the beam-splitter and reference mirror mounted to sizable aluminum posts. The polishing chamber was rigidly clamped to a V-block attached to the base. As a vibration isolator, a 1" thick piece of particle board was used as an optical table, with partially inflated inner tubes separating it from the lab bench.

Fluid motions in the electrolyte must be avoided for the same reason. This required that the polishing be done at room temperature to avoid thermal gradients. Strongly polarizable solutions should be avoided, due to a large fringe shift when voltage is applied. Bubbling of the electrolyte should also be avoided. In consideration of these factors, Sprague chose an electrolyte of 5% sulfuric in glacial acetic acid. This successfully avoided the polarization problem. If the voltage was applied in pulses of less than one second duration, it polished molybdenum well at room temperature, with no bubbling. The refractive index of the sulfuric-acetic mixture is 1.37, so by Snells law, the wavelength of

He-Ne laser light in this medium is approximately .46 microns. A shift of one fringe corresponds to a surface removal of one half-wavelength, or 2300 Å.

A pulsed power supply (schematic shown in Appendix 2) was developed to supply the short voltage pulses required--around .1 second. A monitor was also designed (also shown in Appendix 2) to count the number of fringes passing a given point. This was coupled to the system by the use of fiber optics and a photodiode. For reasons to be mentioned later, this system was adapted to be a pulse counter for the power supply.

Unfortunately, the interferometer was found to be inadequate. As the polishing depth passed about .25μ, a blue colloid (hydrate molybdenum pentoxide) formed on the surface. This effectively blocked the red laser beam from reaching the surface, causing the interference image to deteriorate. Alternate polishing solutions were tried--such as combinations of alcohols with sulfuric acid--but these suffered from either polarization or excessive bubbling.

3.3.2. Calibrated Pulsed Polishing

It was noticed that the polishing rates achieved by the above technique were fairly uniform, which led to the adoption of a calibrated pulsed polishing routine using the same sulfuric-acetic mixture at room temperature. By holding the polishing conditions as uniform as possible and adopting an appropriate iteration scheme, it was felt that accurate surface removal could be achieved. The power supply was used in the pulsed mode so that better time resolution would result. The total polishing time was around 5 seconds. By using a pulse duration of .1 second, the elapsed time was easier to monitor.

The polishing routine adopted was as follows:

1. Mask off a portion of the sample so that the resulting step height could be measured on an interferometric microscope.

2. Polish a preselected number of pulses known to fall short of the target depth. This was done with laser interferometer monitoring to get a feeling for polishing rate.

3. Remove the mask.

4. Measure the step height--polish depth--on an interferometer microscope.

5. Calculate a new number of pulses based on the maximum polishing rate and a distance short of the polish depth.

6. Iterate from step one as many times as necessary.

The best conditions for polishing were found to be: 10V, .1 second pulses with a duty cycle of 1%, 5% sulfuric-acetic mixture and ambient temperature. It typically took four iterations to polish the sample to the desired depth. The polishing system is shown schematically in Fig. 11.

Since the polishing procedure used was new and possibly unsure, a decision was made to aim for the depth of the peak of the damage curve. In the event of an error in measuring the polishing depth, the peak represents the most slowly changing portion of the damage curve--as well as the region which should show the largest effect of the irradiation. The only drawback of this choice is that the concentration of bombarding ions begins to climb strongly in this region. Since copper has a

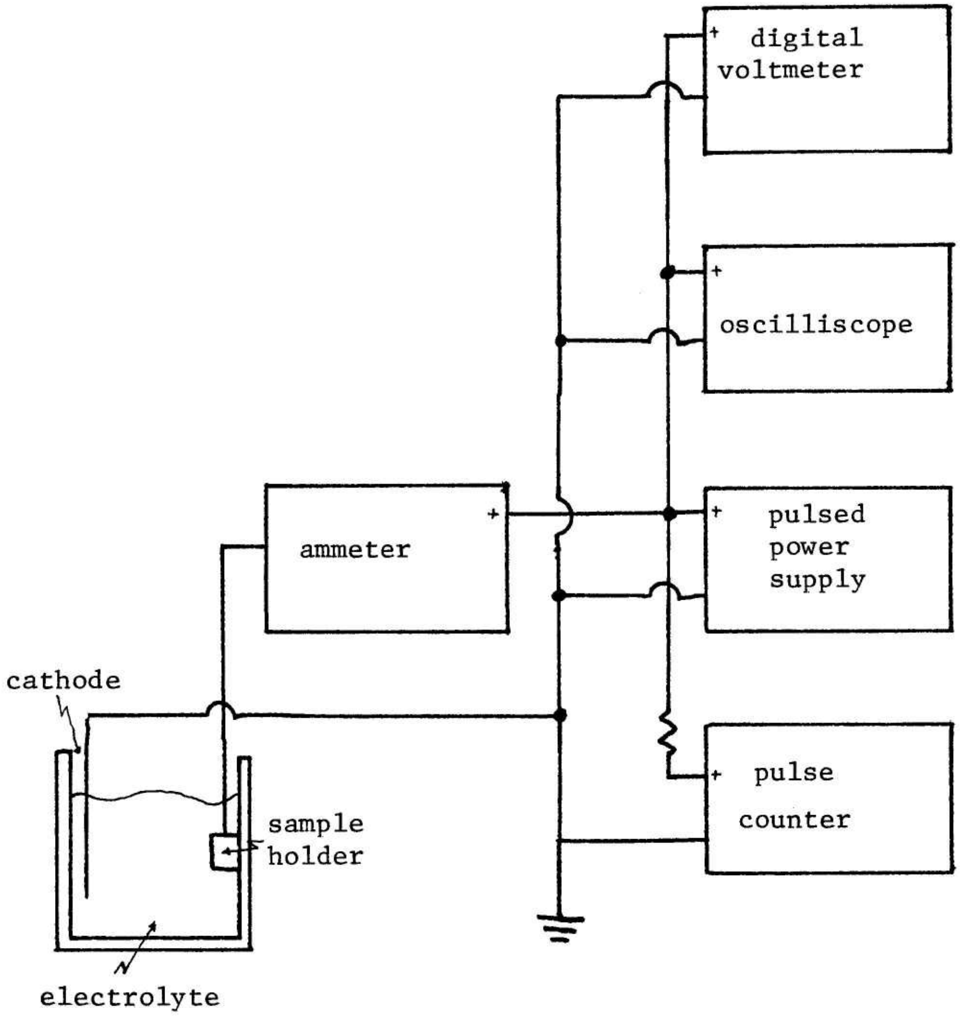

Figure 11 General schematic of polishing system

reasonable solubility in molybdenum at the irradiation temperature [solubility limit of Cu in Mo at 950°C = 1.5 weight % (33)], it was felt that precipitation would not be a major problem. The solubility limit of Se in Mo is not available, but no evidence of precipitation was seen.

3.3.3. Interference Microscopy

Since the step height measurements were the key step in the above procedure, it would be advantageous to briefly describe the principle of operation of the microscopes. The first microscope to be used was a Carl Zeiss interference microscope utilizing a Micro-Michelson interferometer. It is shown schematically in Fig. 12 (30). This is a dual beam interferometer--relying on the differences in path length of two beams of light to display an interference image of the sample. Knowing the wavelength of light used (in this case thallium--5300 Å), the step height can easily be computed from the fringe shift--as in Fig. 13.

As can be seen from the diagram, if the step is sharp and more than one half-wavelength high, confusion can exist in connecting the fringes across the step. This problem is removed on the Zeiss unit by having two light sources available--monochromatic thallium and white. If white light is used, the intereference pattern breaks up into colored fringes, with the central zeroth order fringe being black. This makes it an easy matter to determine not only the number of integral fringe shifts, but also the sense of the shift. The microscope had a polaroid back attached for easier measurement of the fringe shift.

Unfortunately, the Zeiss microscope broke down during the polishing procedure--necessitating the use of another microscope. A Tolansky interference microscope (31) was arranged, since the major components--

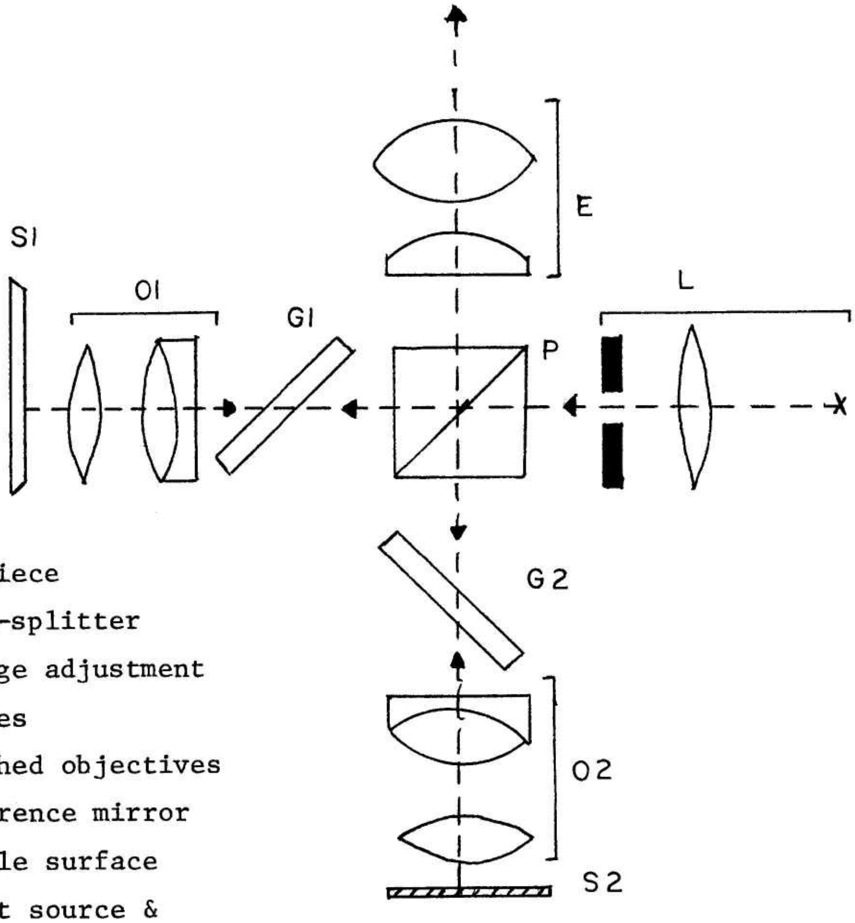

E - eyepiece
P - beam-splitter
G_1, G_2 - fringe adjustment plates
O_1, O_2 - matched objectives
S_1 - reference mirror
S_2 - sample surface
L - light source & collimator

Figure 12 Micro-Michelson interferometer

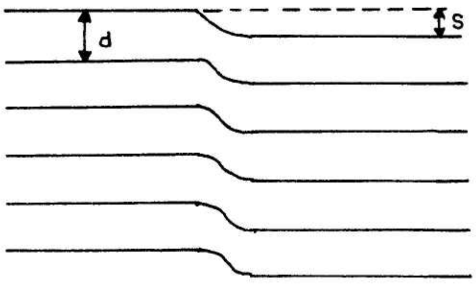

$$\text{HEIGHT} = (s/d) \times (\lambda/2)$$

s = fringe shift
d = fringe spacing
λ = wavelength of illuminating light

Figure 13 Typical fringe image at a step microscope, beam splitter and long working distance objective were readily available. This arrangement is shown schematically in Fig. 14. This microscope uses a multiple beam technique which is capable of much higher depth resolution than the two beam interferometer. The optical flat placed at a small angle to the sample is partially silvered to a reflectivity near .9. With the silvered side in contact with the sample, multiple reflection occurs, with a fraction of the beam escaping at each reflection to interefere with the original beam. This produces a much sharper fringe pattern--much in the same way that a diffraction grating yields a sharper pattern than a pair of slits. The orientation of the fringe pattern can easily be changed by movement of the flat.

Once again, the need existed for both monochromatic and white light sources. A Helium-Neon laser (λ=6328Å) was used for a monochromatic source, while an incandescent spotlight followed by a conderser--aperture system was found suitable for the white light source. The long working distance objective available did not provide sufficient magnification to accurately measure the fringe shift, so a photographic method was used. A 35 mm camera was mounted to the micrcscope and the developed negatives were projected with a slide projector. Glass slide mounts were used to avoid buckling and distortion problems. Measurements of fringe shifts could easily be made on the enlarged image and interpreted in the same way as previously.

From a practical viewpoint, the Micro-Michelson microscope was much easier to use, obviating the need for darkroom work or manipulating the cover glass. If one is not available, the Tolansky microscope is much

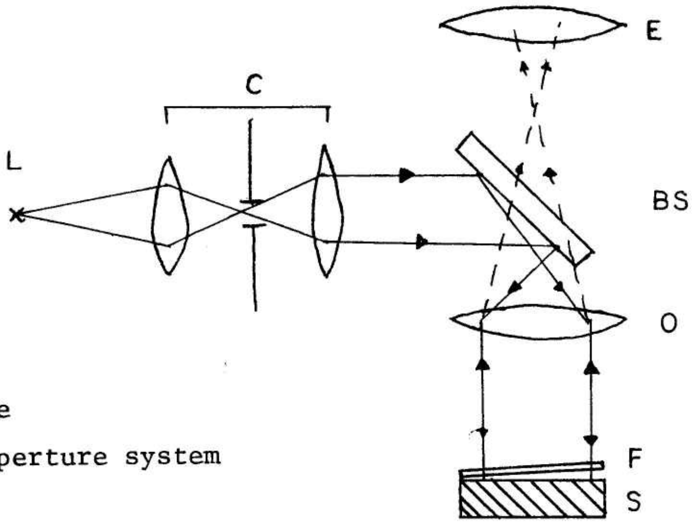

L - light source
C - condenser-aperture system
E - eyepiece
BS - beam-splitter
O - objective lens
F - partially silvered optical flat
S - sample

Figure 14 Tolansky interferometer

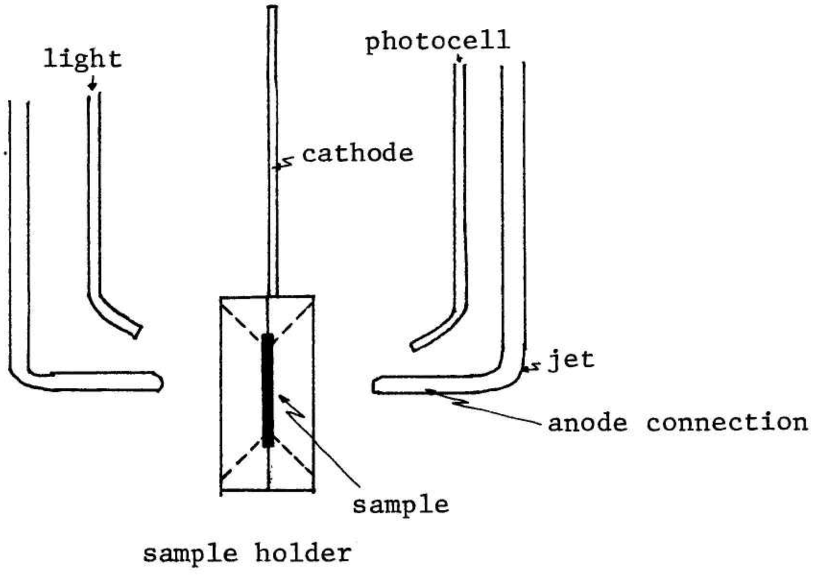

Figure 15 Jet electropolisher

easier to construct. Unless much care is taken in producing the partially silvered optical flats, the two techniques were found to produce equivalent results and can be considered interchangeable. Due to the malfunction partway through the procedure of the Micro-Michelson microscope, the Tolansky unit was used as well.

3.3.4. Jet Electropolishing

In order to produce an electron transparent region in the samples, it was necessary to jet electropolish them. This polishing apparatus is diagrammed in Fig. 15. This technique produces a dished surface. When it intersects the other surface, a curved wedge is formed. It was vitally important that the ion bombarded side not be etched in any way--so as to be confident that the region examined was at the preselected damage level. In order to insure this, a substance was found to mask off the front surface. Since the hole detection system is optical, the mask material must be transparent. Clear nail polish was found to be almost ideal--it resisted attack by the polishing solution and was easily soluble in acetone, leaving a clean surface when removed. In order to ensure that the mask was not erroded by the jet of electrolyte, the jet impinging on that side was disabled.

The polishing solution used was the standard one for molybdenum--25% sulfuric acid and 75% methanol. The best conditions were found to be: temperature=-25° to -35°C, voltage=10 to 15 volts and current=10 to 12 ma. There was evidence of preferential attack at the grain boundaries of some of the samples--in fact, two had penetration occur at grain boundaries.

Once penetration occurred, the samples were examined in the TEM.

Those that did not possess adequate thin area were thinned an additional amount in the ion mill. This machine bombards the sample with 6-10 KV argon ions and sputters some of the surface atoms. With a low incidence angle of the ion beam, fairly uniform thin areas can result. Since a hole existed in the samples already, the emergence of one could not be used to judge the extent of surface removal. Hence the samples were bombarded for a short time (30 minutes) and then examined in the TEM. The ion mill was not found to introduce any black spot damage. Much care had to be taken in mounting the samples in the holder, since it was very easy to introduce deformation during this step. Of course, the ion beam on the irradiated side was not used in order to retain the desired region of examination.

3.4. Electron Microscopy

Due to the expected small size of the voids, the microstructual investigation called for careful, high resolution TEM work. Two microscopes were used--a Phillips EM300 and a Siemens Elmskop 101, both equipped with goniometer stages. Although the Phillips EM300 is not considered a very high resolution TEM, the resolution was adequate for this study. Because the tilt stage was fairly well calibrated, as well as the ease of access, this microscope was used for the routine work. Specimen contamination in the Siemens is kept to a minimum by a column vacuum better than 10^{-6} torr. The only disadvantage of this microscope is that the tilting is somewhat inaccurate and unreproducible--introducing error into the thickness determination by stereo techniques.

Essential conditions for successful observation of voids are that the stability of the microscope and the cleanliness be optimized. This means that the apertures as well as the sample must remain as clean as possible. The use of a cold finger near the sample (to condense volatiles) as well as achieving the best vacuum possible in the microscope greatly aids this. In order to achieve a high degree of stability, the microscope must be allowed a reasonable warm-up period after obtaining a beam.

Voids, especially those on the order of 40Å diameter, may be difficult to observe. An important aid is the use of a through focal series. As mentioned previously, when the focus changes from under to over focus, the contrast of the voids changes. At underfocus, the voids appear as bright central regions surrounded by a dark ring. An overfocused condition yields reversed contrast. Since the contrast from small voids in an in-focus condition is very low (due to absorption only), they were very difficult to see--especially at higher magnifications. It was found that the best way to locate the voids was at lower magnifications (∿50 kX) by varying the focusing. One they were located, the magnification could be raised in small steps--with attention fixed on the voids. Once the desired magnification was reached (usually 100-150 KX), the focusing could be adjusted to yield the sharpest view of the voids.

Voids are most easily observed in thin regions under kinematical conditions (away from strong Bragg reflections). In many samples, this severely limited the available regions for observation. Although attempts were made to ensure that the regions examined were typical of the overall sample, there was a probable bias from not being able to observe any but the larger voids in the thick sections of the samples. Standard practices were taken to minimize beam contamination (polymerization of hydrocarbons by the electron beam). Once a suitable region was chosen, focusing and astigmatism correction were done in a neighboring location. Only after the conditions were optimized, was the selected region brought under the beam and photographed. Thin regions respond strongly to contamination of the beam by a strong loss of contrast and localized bending. By decreasing the time that the region is under the beam, the effects of this are minimized.

In order to obtain the most reliable results in stereo work, the "z axis" control on the Phillips was used. This shifts the sample relative to the axis of the barrel tilt, having two important results. First, it makes the taking of a stereo pair much simpler; as the sample is tilted, the same features remain in the field of view. This makes it possible to tilt in diffraction space without the need to search for the same area of the sample after tilting. More importantly, it makes thickness calculations from parallax measurements more accurate. When the control is set properly, the tilt axis and the optical axis of the microscope interesect--an essential condition for the use of the simple relation given in the next section.

The taking of useful stero pairs also requires that (1) the same region must be contained in each micrograph, (2) the tilt angle between the two views should be betweeb 6-20°, with 12° being optimal for the ease of visual accomodation of the stereo image and (3) the background should ramin at a similar contrast for the two micrographs. The first point can be easily achieved by plaing a unique feature--a dislocation, piece of dirt, strangely shaped void...--on a reference point on the screen. When this is repeated after tilting, one is assured of viewing the same region.

The last point, similar background contrast, is much more difficult to achieve. It requires that the diffraction conditions remain constant during tilting. If Kikuchi lines are visible in diffraction space, tilting along a band fulfills this requirement. Unfortunately, Kikuchi bands are visible primarily in thick regions of the sample and are not often observed in heavily radiation damaged materials. Tilting along an extinction contour (bend contour or thickness fringe) serves much the same function. This also has drawbacks, in that these represent strong diffracting conditions where voids are not highly visible. It was found that by the judicious use of both tilts, an orientation could be reached where the required tilt for stereo work produced background contrasts nearly equal by eye.

In a few cases, the micrographs used for the stereo work were suitable for the size distribution analysis. In the majority of the cases, a lower magnification was used for the stereo pairs than those intended for sizing. This meant that for a complete representation of a given area, five negatives must be exposed--two for the stereo pair, two diffraction patterns (one of each tilt) and at least one high magnification view for the size distribution. Since the high magnification views give a rather small sample size, more than one was usually taken.

It was found that the underfocus condition (light central region surrounded by a dark ring) was much easier to work with on the Phillips microscope, as well as in measuring the size distribution. In the case of the Siemens microscope, with a much higher current density in the electron beam, the overfocus condition (darker than the background) was easier to work with. Determination of the void shapes and orientation was found to also be easier in an overfocused condition.

3.5. Foil Thickness Determination

In determining the void volume fraction and number density, the foil thickness is an important parameter. In many applications of optical transmission microscopy, sample thickness can easily be determined by such techniques as: laser interferometry, mass, radiation absorption or even a micrometer. These techniques are usually not applicable to electron microscopy studies due to the small areas examined and non-uniformity of thickness. Because of this, it is desirable to determine the thickness from some feature of the observed region in the microscope. One technique which is often used is that of judging thickness by electron transparency (screen brightness). The basic problem with this is that it depends upon a judgement, the accuracy of which is based greatly on the experimenters experienced and the experimental conditions. In most cases, the errors involved are unacceptably large and a more reliable method must be used.

In cases where the sample exhibits slip traces, twin boundaries, helical dislocations or any other defect which intersects both surfaces and whose habit plane is known, the foil thickness may easily be determined. The projected width of the defect is related to the thickness by:

$$t = w \tan \theta \qquad (3.1)$$

where t = foil thickness, w = projected width and θ = angle between foil surface and plane of feature. If the electron beam is not perpendicualr to the foil surface, as is often the case with goniometer stages, a correction term must be applied. This is not usually possible, since many of the parameters needed are not accessible.

The most important point of the above method is that the habit plane or direction of the feature must be known. In most cases, this is not true of dislocation lines. Here it is necessary to induce some slip and use the resulting slip trace (obviously after the desired micrographs are taken). The easiest way to do this is to build up contamination with the beam at the nearest edge--inducing stress. Unfortunately, this does not work well in irradiated materials--voids and other damage structures are strong barriers to dislocation motion.

Another technique involves the use of thickness fringe contours. In principle, white fronges occur at:

$$t = (n,\ n+1,\ n+2,\ \ldots)\xi_g \qquad (3.2)$$

where ξ_g = extinction distance for the particular Bragg reflection, n=0 for bright field, n=1/2 for dark field. The extinction distance can be found from Eqn. 2.14. Equation 3.2 strictly applies only if the crystal is oriented at the exact Bragg angle to the beam (w=0). When this is not the case, the effective extinction distance is given by:

$$\xi_g^w = \xi_g/(1+w^2)^{1/2} \qquad (3.3)$$

Unfortunately, there is no easy way to measure w. If w=.5 (a small deviation from the Bragg angle), ξ_g is off by 10%, as is the thickness. If w is larger, the error increases rapidly.

It is possible in many cases to set w=0 by manipulation of the Kikuchi bands in diffraction space. When the appropriate Kikuchi line passes through a diffraction spot, w is nearly zero. Once again, things don't fare so well with irradiated specimens. In heavily cold worked or irradiated materials, Kikuchi bands tend to be very diffuse, if they can be detected at all. In this case, the only indicator available will be the intensity of the diffraction spot, very difficult to judge accurately.

Probably the most common technique used for irradiated materials involves the parallax shift between micrographs of a stereo pair. Any features intersecting both surfaces may be used--such as grain boundaries, dislocations or voids. If a pair of features can be identified as intersecting opposite surfaces of the foil, the thickness may be determined from:

$$t = p/2M\sin(\phi/2) \tag{3.4}$$

where p = measured parallax shift, M = magnification and ϕ = angle of tilt between micrographs. It is clear from this relation that the critical factor is the angle of tilt. The percentage error in the calculated thickness is roughly equal to the inaccuracy of the tilt stage, which is typically in the neighborhood of 10%.

The stereo technique is the most convenient and accurate method to determine the foil thickness. In practice, it was difficult to decide which voids were intersecting the surface. Because of this, a number of voids were chosen (as well as their stereo pairs) and their center-to-center spacing was measured in each micrograph. The difference between these spacings was the parallax. The differences in height between the voids was then calculated from Eqn. 3.4. The largest value was chosen as the foil thickness after insuring that it wasn't due to either an incorrect measurement or an artifact.

3.6. Void Size Distribution Analysis

Determining size distribution parameters from TEM analysis is appreciably different than from metallographic sections. In the first place, one is treating a two-dimensional projection of a three-dimensional structure--additionally, corrections must be made for features whose centers lie outside of the foil thickness, as well as overlap. In the case of voids, the foil thickness is appreciably greater than the void diameters, so the correction will be small. The overlap problem is also lessened, as nearly all overlapped voids can be separately identified. First the technique used to measure void sizes will be described, then the conventions and relations adopted to make the raw data useable.

A Zeiss particle size analyzer was used to measure the diameters of the voids in the micrographs. This is an apparatus that projects a variable diameter circle of light through a photograph. By matching the diameter of the circle with an appropriate dimension of the feature considered and pressing a foot pedal, the appropriate mechanical counter is incremented. There are 48 counters (48 size classes). Simultaneously, a movable arm puts a pinhole in the center of the void counted to avoid its being recounted.

There are four different size class scales available--linear normal, linear reduced, exponential normal and exponential reduced. The reduced mode simply covers a smaller range than the normal mode (.4 - 9.2 mm vs.

1.2 - 27.7 mm). In the linear mode, each size class has equal width, while in the exponential mode, as the interval center increases, the class width does so also. The operating manual suggests the use of the exponential mode for wide size distributions. This recommendation was followed here. In order to get reliable results, some conventions must be adopted for the measuring process. These will be described below.

Since the relationship between the true void size and the image on the micrograph varies with the focusing conditions under which it was taken, the appropriate dimension must be decided upon. Nearly all of the micrographs taken on the Phillips were in the underfocused condition with the diffracting conditions tending towards kinematical. In this case, the true diameter of the void will be represented by the inner diameter of the first dark ring surrounding the bright central region. The images from the Siemens were taken in an overfocused condition--here the true diameter was taken as the inside of the first bright ring surrounding a dark center.

The high resolution views showed that the voids were not spherical. It was decided to measure the size of these by adjusting the circle of light so that it was totally enclosed by the projection of the void. This diameter was used as the size parameter (with appropriate geometrical corrections--as shown in Appendix 3). This way, there would be consistency between the high resolution views (where the faceting was clear) and the lower resolution views from the Phillips (where the voids appeared circular).

Another decision had to be made about voids that were either partially within the foil thickness or field of counting (arbitrarily determined). Counting only those voids whose centers lay within the field of counting was felt to be the appropriate measure. Approximately half of the partially enclosed voids will have their centers within the field. By adopting this convention, the results would be statistically correct.

Determining which voids were partially within the thickness of the sample is a more difficult problem. It could be done by stereo techniques, which would not be practical with the particle size analyzer. Wolff (32) reported that surface voids have a somewhat "fuzzy" appearance, a feature that wasn't thought to be reliable enough for use here. This problem was resolved by counting all of the visible voids and applying the following correction factor:

$$N_i^c = N_i^o/(1+IC_i/t) \tag{3.5}$$

where: N_i^c = corrected number of voids for each size class,
N_i^o = observed number of voids for each size class,
IC_i = interval center for the size class and
t = foil thickness

The problem of accurately knowing the enlargement from the negative to the print was sidestepped by a simple trick. A reference scale--such as a clear plastic ruler--was placed in contact with the negative in the enlarger, in such a way that it was projected onto an edge of the print. Measurement of the enlarged scale gave the enlargement used. In one step, this takes into account all of the minor changes--such as paper shrinkage in drying and shifts due to focusing.

CHAPTER 4

RESULTS

4.1. Ion Bombardment

The samples were all irradiated at a temperature of 900°C, with no significant temperature fluctuations. The chamber vacuum was maintained at less than 10^{-6} torr at all times during irradiation. Samples E, F, I and J were bombarded with 5 MeV Cu^{++} ions and samples A_1, C_1, A_2 and C_2 with 5 MeV Se^{++} ions. It was not possible to monitor the beam current on target during irradiation. This required one minute interruptions at twenty minute intervals to measure the beam current. The low dosage samples had the beam current measured immediately before and after irradiation. The irradiation conditions are summarized in Table 4.

4.1.1. Damage Calculations

Before the irradiation schedule was decided upon, a run was made of EDEP-1 at NRL (see Appendix 1) for 5 MeV Se^{++} ion bombardment. The output of this was used to calculate the beam current--time conditions to meet the specifications listed previously. The assumption was made that the results for copper would be within 10% of those for selenium. The irradiation conditions were then based upon this assumption. After the irradiation, the code was run for copper ions specifically and it was found that the assumption was erroneous. The peak displacement level calculated from the EDEP-1 data was 16 dpa while the estimate yielded 20.1 dpa. Since the specified conditions couldn't be met--20 dpa in a region where the concentration of copper was less than .02%, it was

TABLE 4

IRRADIATION CONDITIONS

(900°C, 10^{-6} torr, 5 MeV ions)

SAMPLE	ION	TOTAL BEAM TIME (min.)	MINIMUM CURRENT (nA)	MAXIMUM CURRENT (nA)	MEAN CURRENT (nA)
E	Cu^{++}	84	50	50	50
F	Cu^{++}	85	50	43	48.5
I	Cu^{++}	8.4	50	50	50
J	Cu^{++}	8.4	50	50	50
A_1	Se^{++}	167	21	10	17
A_2	Se^{++}	162	25	16	18.4
C_1	Se^{++}	18.4	16	15	15.5
C_2	Se^{++}	17.7	18	15	17

decided to examine the region of maximum damage--the peak of the curve.

Details of the damage calculations using EDEP-1 are given in Appendix 1. The results will be summarized here. Figures 16 and 17 show the displacement and bombarding ion concentration vs. depth for copper and selenium respectively. The conditions at the peak are listed in Table 5. The peak damage occurred at a depth of .74 microns for copper ions and .805 microns for selenium ions.

As insurance, in case the calibrated polishing was not successful, the damage level and ion concentration were calculated at depths .1 micron removed from the peak. It was felt that .1 micron was greater than the probable margin of error for the procedure. The results of this calculation are summarized in Table 6. As can be seen, the difference in displacement level is less than 7 1/2 % in all cases (although the concentration of the bombarding ion can be as much as 150% larger, in the case of copper). The differences in damage level are insignificant, while the effects of these changes in concentration are unknown.

4.2. Sample Preparation

Calibrated electropolishing was found to be a viable technique. The samples were all polished to within an acceptable limit of the target depth. Tests on molybdenum foil stock had shown the conditions specified in the technique section to produce an adequate surface, although there was evidence of preferential attack of some grains. This etching was small, so it could be ignored. The blue colloidal substance that had made the laser system useless may have been advantageous to this

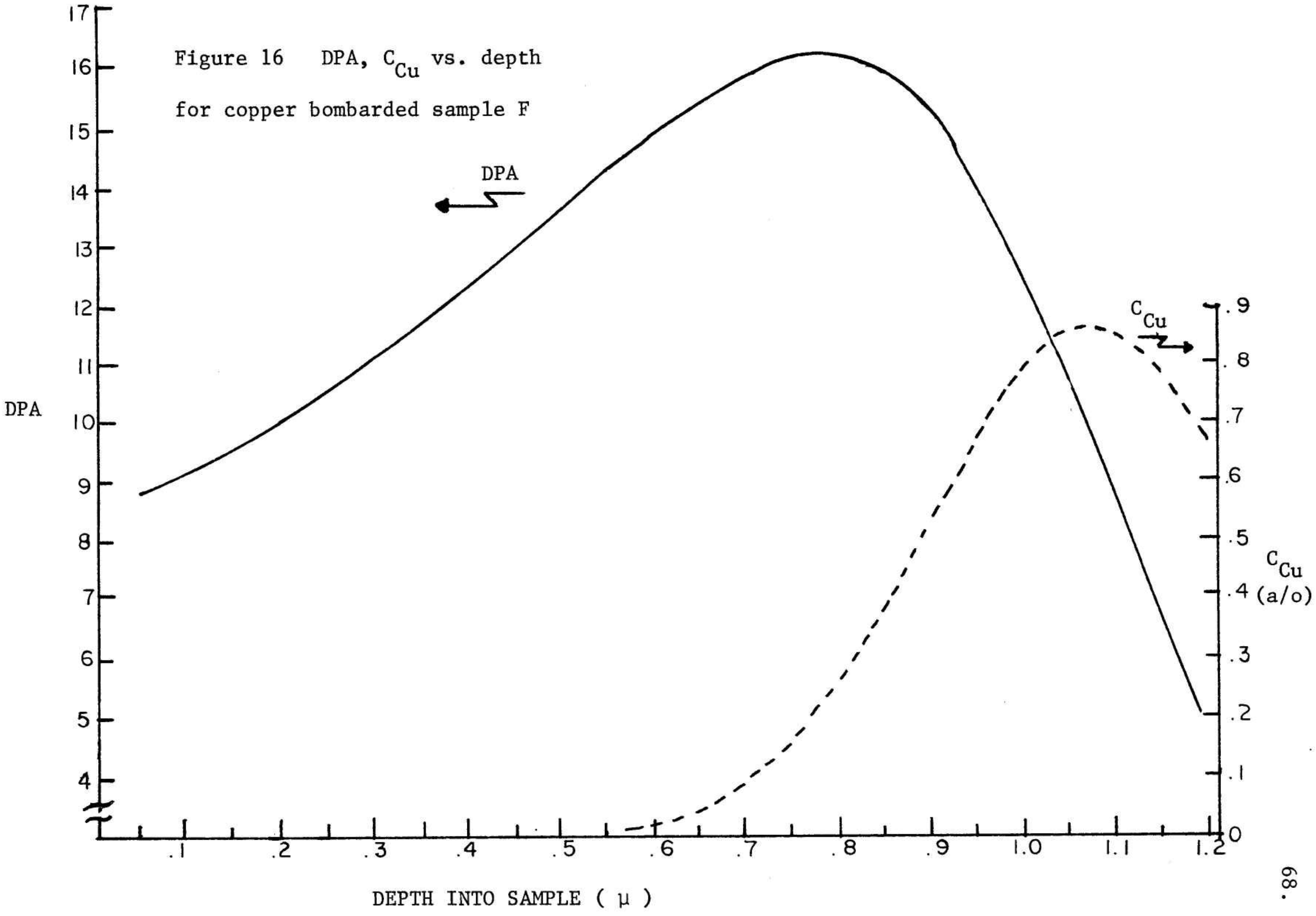

Figure 16 DPA, C_{Cu} vs. depth for copper bombarded sample F

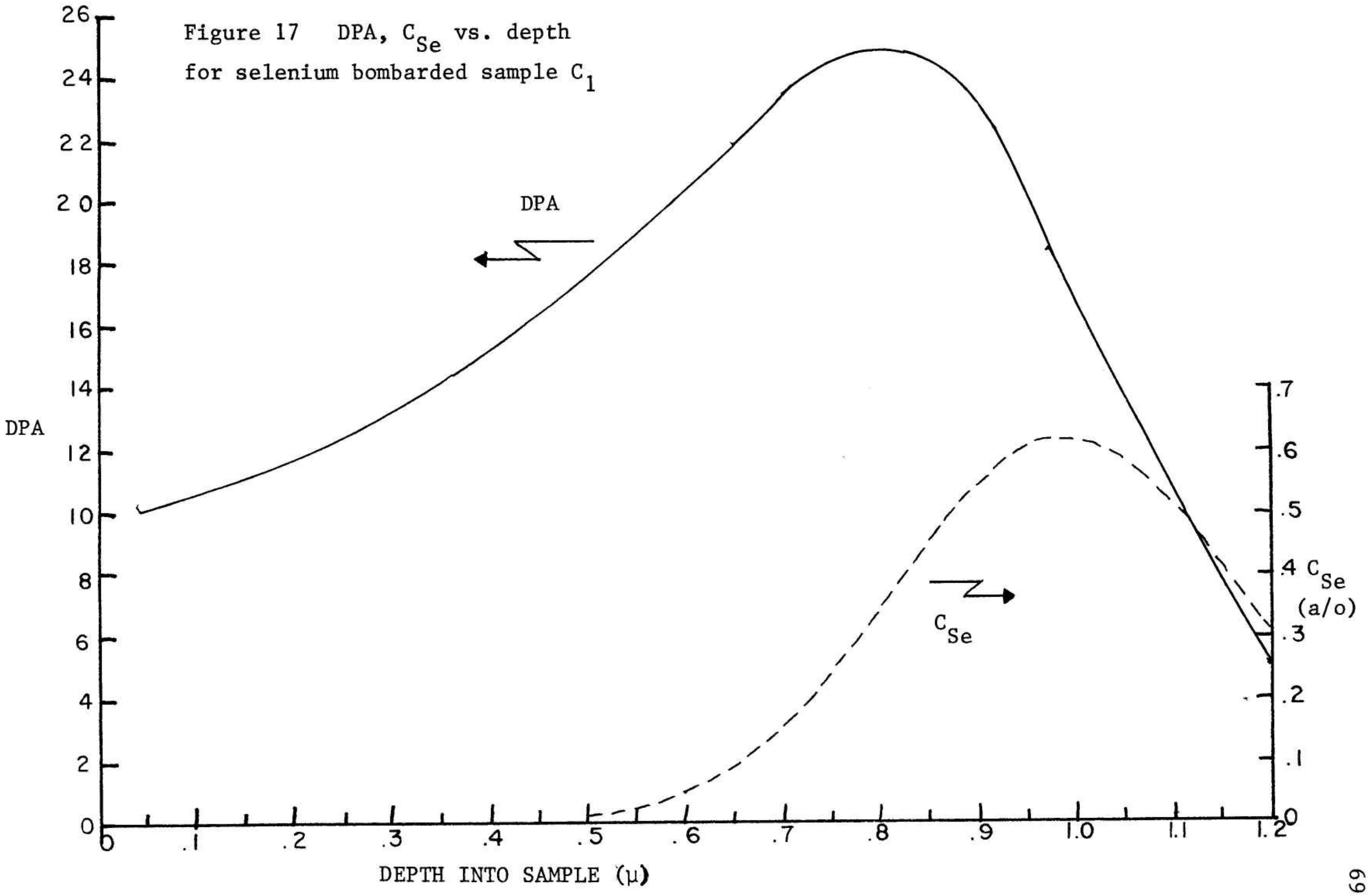

Figure 17 DPA, C_{Se} vs. depth for selenium bombarded sample C_1

TABLE 5

RESULTS OF EDEP-1

SAMPLE	ION	PEAK DAMAGE DEPTH (μ)	DPA @ PEAK	DPA/SEC @ PEAK	C_{ion} @ PEAK (a/o)
E	Cu^{++}	.74	16.59	3.29×10^{-3}	.148
F	Cu^{++}	.74	16.28	3.19×10^{-3}	.145
I	Cu^{++}	.74	1.66	3.29×10^{-3}	.0148
J	Cu^{++}	.74	1.66	3.29×10^{-3}	.0148
A_1	Se^{++}	.805	23.97	2.39×10^{-3}	.342
A_2	Se^{++}	.805	25.17	2.59×10^{-3}	.360
C_1	Se^{++}	.805	2.41	2.18×10^{-3}	.0344
C_2	Se^{++}	.805	2.54	2.39×10^{-3}	.0363

TABLE 6

DAMAGE LEVELS NEAR PEAK

SAMPLE	PEAK DPA	+.1μ DPA	-.1μ DPA	PEAK C_{ion} (a/o)	+.1μ C_{ion} (a/o)	-.1μ C_{ion} (a/o)
E	16.59	15.80	16.10	.148	.368	.0430
F	16.28	15.51	15.80	.145	.362	.0422
I	1.66	1.58	1.61	.0148	.0368	.0043
J	1.66	1.58	1.61	.0148	.0368	.0043
A_1	23.97	22.21	22.55	.342	.525	.163
C_1	25.17	23.31	23.67	.360	.551	.171
A_2	2.41	2.23	2.26	.0344	.0527	.0164
C_2	2.54	2.35	2.39	.0363	.0556	.0173

technique. Some people believe that the existence of a viscous surface layer results in a smoother polish, which this substance may have provided. The Zeiss interferometric microscope was used to measure the surface removal for the copper bombarded samples (E, F, I and J). Samples of the interferograms are shown in Figs. 18 and 19. Fig. 18 was taken with monochromatic green light (λ=.54μ) after the first polishing step with sample E. It can be seen that the polish surface remains fairly smooth with evidence of some scratches. These were probably introduced during the pre-irradiation preparation and either enlarged or uncovered (as with a bridged-over scratch) during the electropolishing. A measurement of step height from this photograph yielded a surface removal of .347μ.

Figure 19 shows an interferogram of sample J after two polish steps. This was taken with white light. The zeroth order fringe (marked) can be seen as the darkest, with the higher order fringes increasingly losing contrast. It is clear from this picture that the while light is necessary to be sure not only of the direction of the fringe shift, but also of the order of the shift. Evidence of surface pitting and preferential etching of grains can be seen here. The upper step was found to have a height of .101μ and the lower .36μ.

The results of the front surface polishing are shown in Table 7 for the copper samples. It can be seen that although only one was very close to the target (J - 3%), the other three were within a band of -11% to +16%. This was felt to be close enough that it would not be worth correcting the ones that fell short.

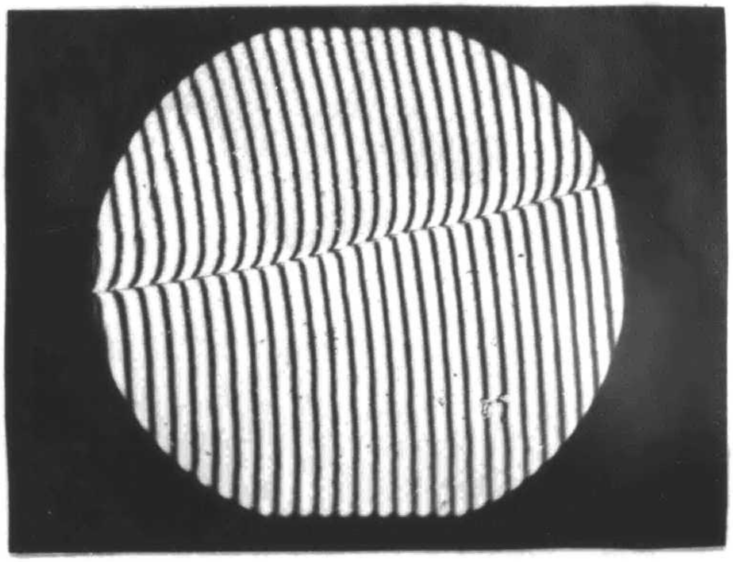

Figure 18 Typical Micro-Michelson interferogram (green light)

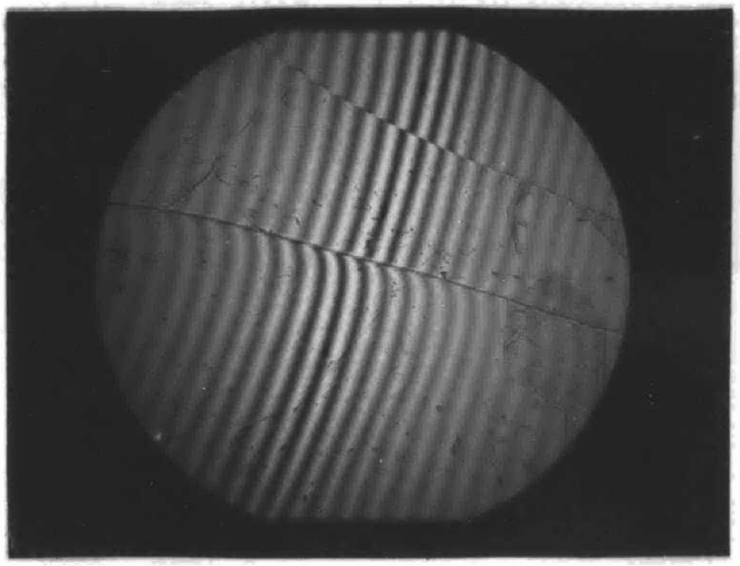

Figure 19 Typical Micro-Michelson interferogram (white light)

TABLE 7

RESULTS OF SURFACE REMOVAL FOR COPPER SAMPLES

SAMPLE	NUMBER OF PULSES	POLISH TIME (s)	DEPTH REMOVED (μ)	ERROR (%)
E	53	5.3	.66	-11
F	50	5.0	.86	+16
I	51	5.1	.82	+11
J	48	4.8	.72	- 3

The selenium irradiated samples (A_1, C_1, A_2, and C_2) were measured with the Tolansky microscope. The Zeiss unit had been shipped out for repair. Due to the relative success with the copper samples as well as the increased possibility of surface damage (the reference flat is placed directly on the surface of the sample in this technique), the amount of surface removal was measured only after the first two iterations. Since the number of pulses calculated for the final polish were based on the maximum polish rate as well as a distance slightly short of the target depth, it is most probable that the final depth is at least within the limits obtained above.

The results from the jet polisher were barely satisfactory. Half of the samples yielded adequate thin area for the TEM examination. In some cases, there was severe grain boundary attack--the hole that registered on the optical system was on a grain boundary or triple point, with negligible thin area. One sample was found to have a large amount of pitting around the outside of the polishing area--due to incomplete contact with the platinum electrode. This problem was solved by the use of a new electrode, with care taken to ensure complete contact.

The samples that weren't suitable were made so by the use of the ion mill (all but one). It typically took three half-hour polishing sessions to produce areas for TEM examination. No artifacts from the ion milling were seen--especially black spot damage. Although lattice defects were most probably formed by the low energy argon ion bombardment, these were primarily very near the surface. The sample remains at temperatures less than 200°C, where the defects have very low mobility. It would not be expected that these made much of a contribution to the void structure.

4.3. Microscopy Results

Five samples were found to be suitable for analysis the TEM. Attention was focused primarily on the features of the void distribution--size, shape and spatial distribution. The other features of the irradiation damage structure--dislocation loops, network dislocations and precipitates were noted, but for reasons mentioned below, these were not carefully analyzed.

The void distribution, while not perfectly uniform, was rather homogeneous. Many of the foils had been somewhat damaged (bent or contaminated) in the handling steps. The results of this would tend to obscure the voids, making any strong conclusion about the homogeneity of the void distribution doubtful. The voids observed ranged in size from about 10-100 Å in diameter. There were probably smaller voids, but these would be below the resolution limits of the microscopes. As will be discussed below, the voids were faceted--having probably a cubo-octahedral shape.

There were a small number of dislocation loops observed. There was also evidence of a small number of precipitates. Since the starting material was reported to have a small precipitate density, they are probably from the annealing treatment. Again, due to the deformation in handling of the samples (evidenced by the bend contours), not much can be said about the influence of the irradiation on the dislocation structure.

4.3.1. Void Shape

The high resolution views of a copper bombarded sample (F) and a selenium sample (C_1) show that the voids are non-spherical in shape. Fig. 20 shows some typical voids observed in sample F. The two-dimensional projection of the void is a square with the corners cut off. The most probable crystallographic shape that would result in the observed projection perpendicular to a (100) face is the cubo-octahedron. This is illustrated in Fig. 21. All of the voids observed with sufficient resolution yielded evidence of possessing the same shape--independent of the size of the voids. The ratio of the length of the side to that of the corner diagonal was approximately 3/2.

Both the round robin micrograph and sample (Mo ion irradiated Mo) show evidence of faceting on the voids. These, however, more nearly approach a circular cross section. On the voids where the segmented nature of the boundary is clear, the projection appears to be a nearly perfect octagon--as illustrated in Fig. 22. This difference in void shape has some implications about the effect of impurities on surface energies. In many cases, impurities have been observed to segregate at void surfaces. If this were the case with copper or selenium, even the low concentration of impurities present at the depth of observation ($\sim$.3 atomic %), could have large effects on void shape. This could come about through either thermodynamic reasons--altering the surface energies of different planes or from kinematical reasons--such as slowing the growth rate in certain directions.

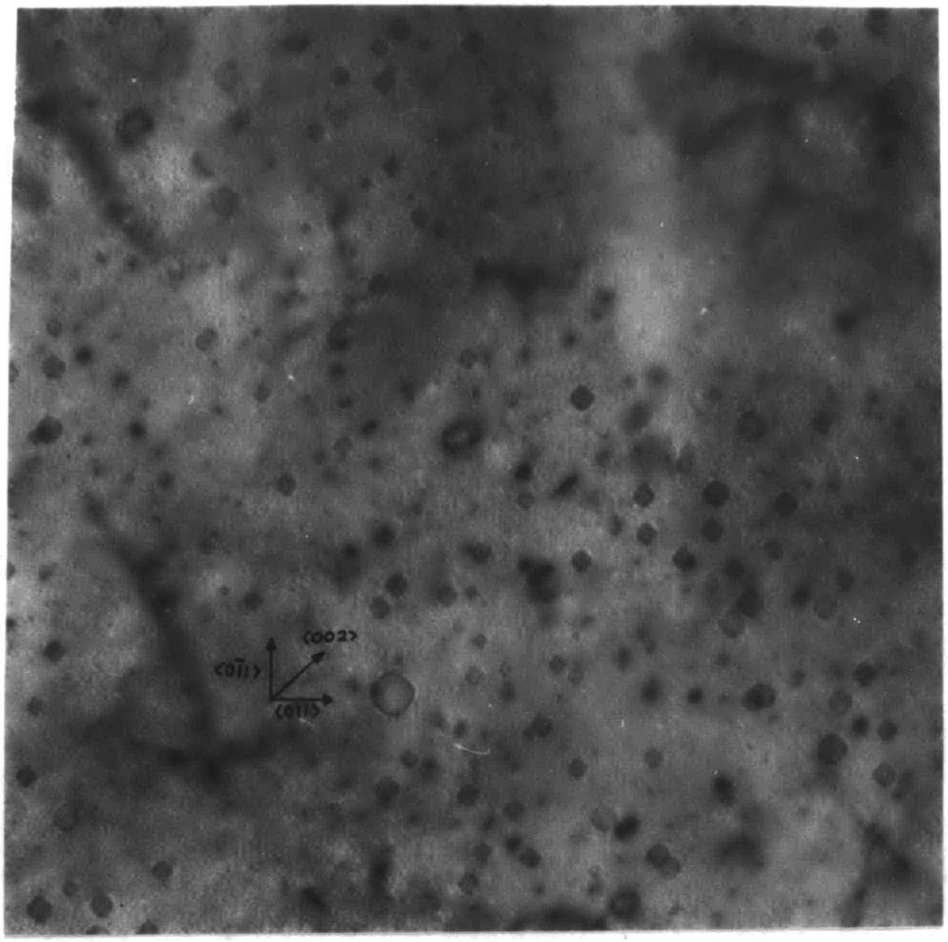

Figure 20 Void faceting in copper bombarded sample (magnification = 493kX)

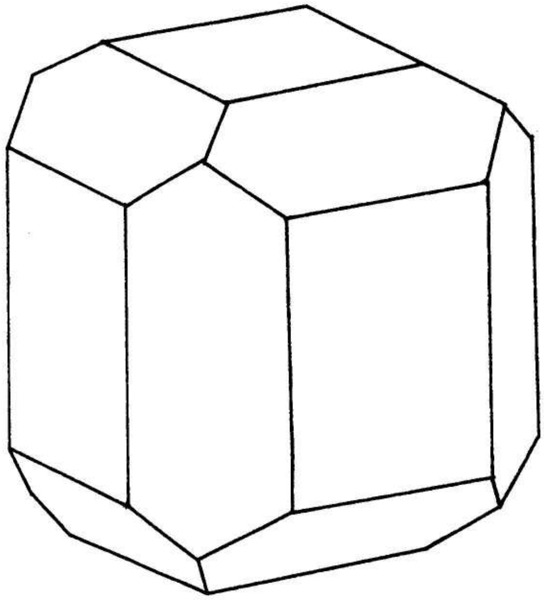

Figure 21 Most probable void shape

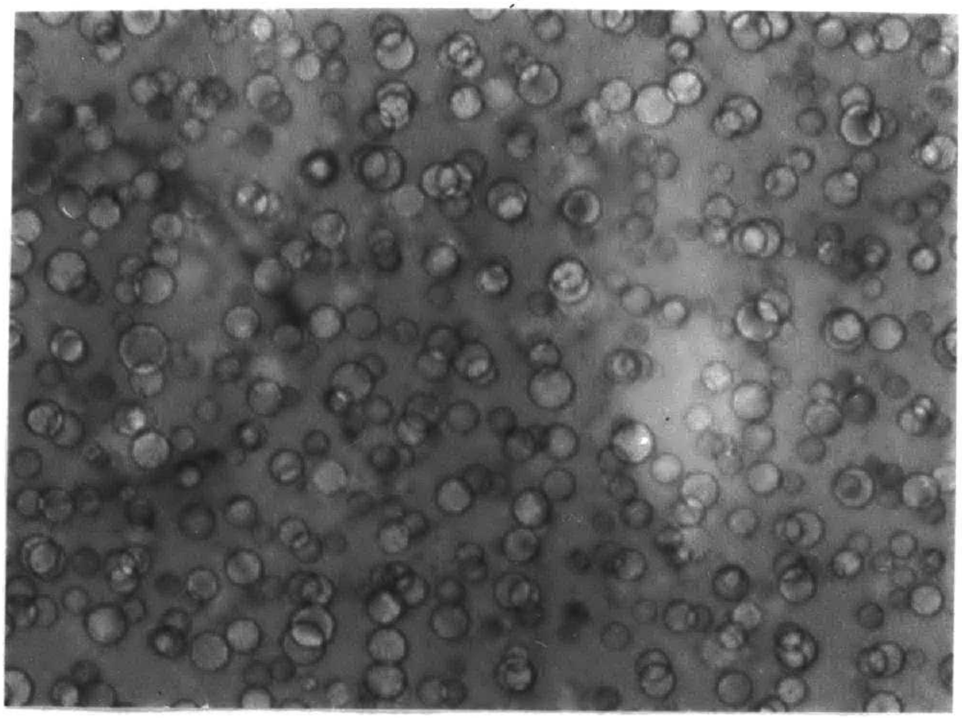

Figure 22 Void faceting in molybdenum ion bombarded sample (magnification = 400kX)

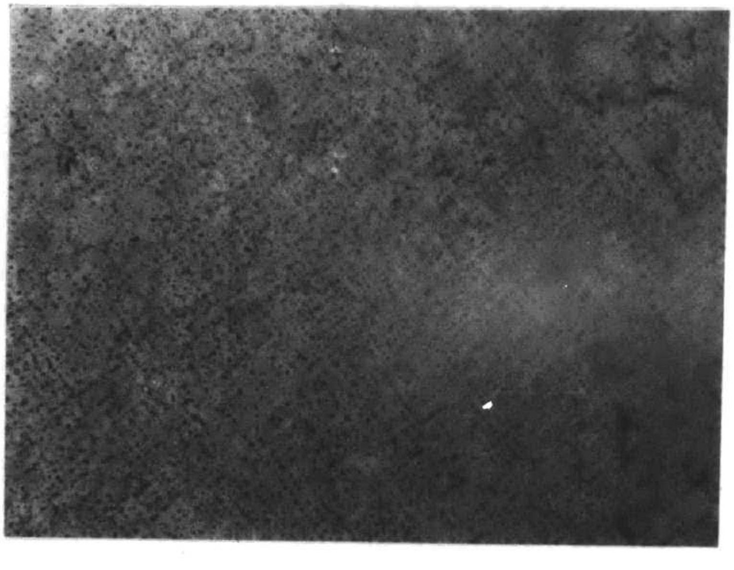

Figure 23 Void lattice (magnification = 54kX)

4.3.2. Void Lattice

Evidence was seen of the formation of a void lattice (a spatially regular array of voids) in one sample--see Fig. 23 for example. This sample (the round robbin sample, 2.7 MeV Mo ion irradiated) was the only one studied that showed a lattice. Unless there is a high void density, the observation of a lattice is highly dependent on the orientation of the sample. It may have been possible that a void lattice existed in the other samples, but was not observed.

Evans (34) has noted some of the features of the void lattice in molybdenum and has shown that it is a body-centered cubic array oriented parallel to the underlying molybdenum atomic lattice. The results from the present study did not allow the determination of the lattice type or spacing. In their study on the same sample, Oak Ridge National Laboratory (26) also found the lattice and measured a lattice parameter of approximately 375 Å.

4.4. Thickness Determination

A problem existed in determining the foil thickness. As shown in Fig. 24, there was a distribution in the measured apparent thickness. The spread in the distribution is due to two causes: (1) difficulty in identifying surface voids and (2) the dependence of the apparent height difference on the orientation of the void pair. It is obvious that if the projection of a line connecting the void pair approached parallel to the tilt axis, the parallax is greatly reduced. This problem could be removed by measuring the parallax shift only on void pairs oriented perpendicular to the tilt axis. Since the solution to the first problem

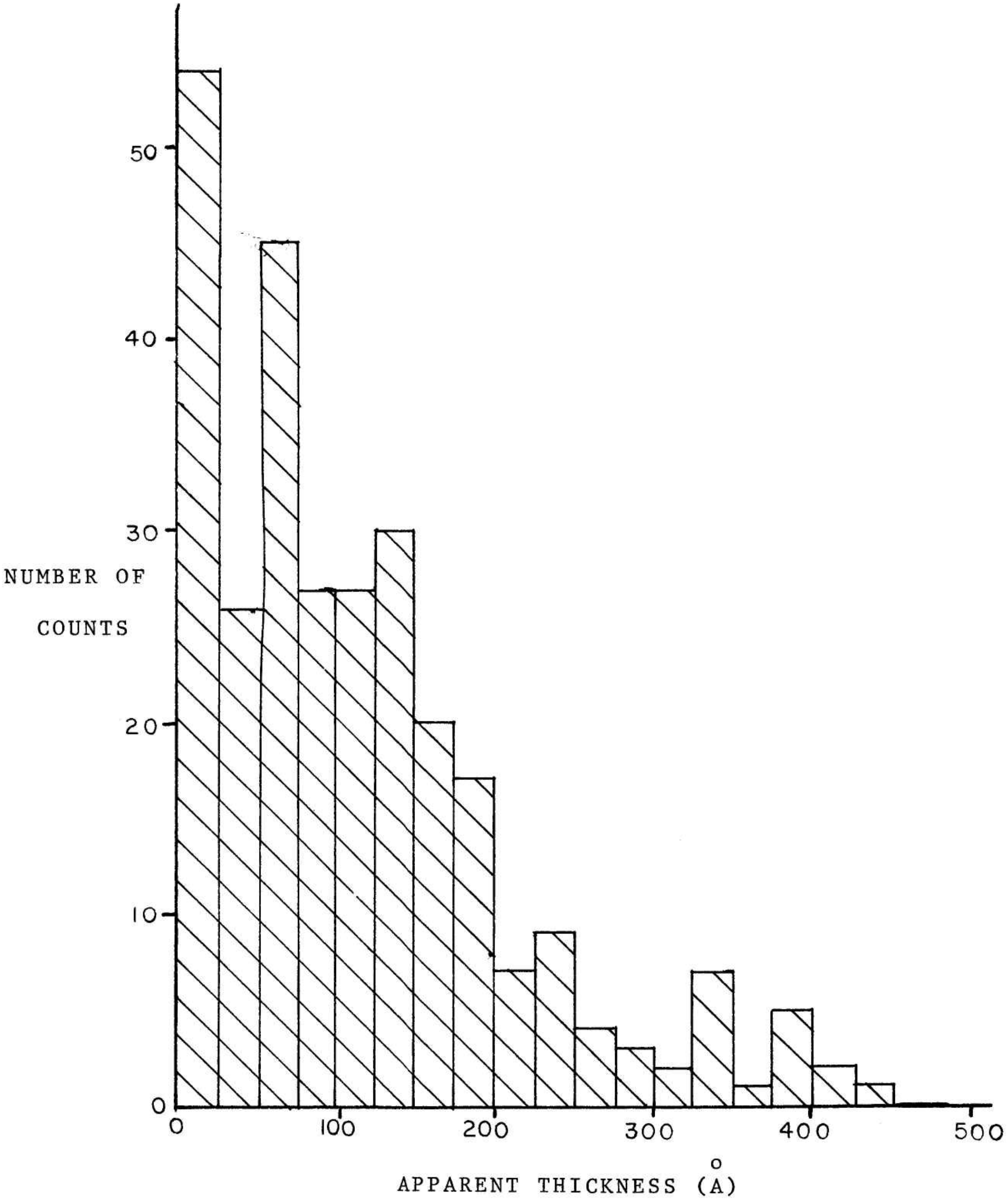

Figure 24 Thickness distribution from parallax technique

requires the measurement of many void pairs in order to be sure of including those that intersect opposite surfaces, it was felt that this measure would also take care of the orientation problem.

In practice, a large number of pairs were measured (combinations from at least 20 voids in each view). The true thickness was taken as the tail of the distribution. An error estimate was made by making duplicate measurements on one stereo pair from the round robbin sample. This, coupled with an estimated inaccuracy in the tilt stage of ± .5° leads to an estimate of the error in the thickness of ± 15%. This will also be the probable error in the calculated void volume fraction.

4.5. Void Size Distribution

The results of the size distribution are summarized in Table 8. The methods used to reduce the raw data and arrive at the statistics are outlined in Appendix 4. The individual results are given in Tables 9-13, with typical curves and micrographs shown in Figs. 25-33. Here, the continuous curve is the normal distribution possessing the same mean and standard deviation as the data (histogram). It can be seen that in all cases, the size distributions approximated normal distributions (skewness between .16 and 1.10, kurtosis between 2.45 and 4.88). A normal distribution possesses a skewness of 0. and a kurtosis of 3.0 (see Appendix 4).

It must be noted that some of the parameters for sample F are estimates. At the time it was first examined, a stereo pair was not taken. Before a more thorough analysis could be made, the sample was lost. Based on the screen intensity and contrast in the negatives, an

TABLE 8

CONDENSED RESULTS OF VOID DISTRIBUTION

SAMPLE	ION/ ENERGY	DPA	C_{ion} (a/o)	MEAN DIAMETER (Å)	STANDARD DEVIATION (Å)	NUMBER DENSITY (v/m^3)	VOLUME FRACTION (%)
E	Cu^{++}/5MeV	15.8	.148	36.7	8.9	4.65×10^{22}	.232
F	Cu^{++}/5MeV	15.5	.145	37.3	12.7	$6.4 \times 10^{22*}$	.414*
I	Cu^{++}/5MeV	1.58	.0148	49.7	14.8	1.83×10^{22}	.239
C_1	Se^{++}/5MeV	23.3	.360	40.4	13.3	1.62×10^{23}	1.22
C_2	Se^{++}/5MeV	2.35	.0363	44.9	16.3	1.35×10^{23}	1.38

* Due to not knowing the sample thickness, these are estimates. For the thickness range mentioned in the text, these values become:

$t = 500$Å, $V_f = .839\%$, #density = 12.8×10^{22} v/m^3

$t = 1000$Å, $V_f = .279\%$, #density = 4.3×10^{22} v/m^3

TABLE 9

VOID SIZE DISTRIBUTION IN SAMPLE E

MICROGRAPH	12358	12567
FOIL THICKNESS (Å)	475	600
MAGNIFICATION (kX)	630	592
NUMBER OF VOIDS COUNTED	243	207
MEAN DIAMETER (Å)	37.9	35.6
MEDIAN DIAMETER (Å)	33.8	31.6
MEAN AREA $x10^3$ ($Å^2$)	1.3	1.2
MEAN VOLUME $x10^5$ ($Å^3$)	.53	.48
VARIANCE ($Å^2$)	65.5	96.5
STANDARD DEVIATION (Å)	8.1	9.8
SKEWNESS	.76	.62
KURTOSIS	4.18	3.35
VOLUME FRACTION (%)	.236	.227
# DENSITY $x10^{22}$ (v/m^3)	4.5	4.8

TABLE 10

VOID SIZE DISTRIBUTION IN SAMPLE F

MICROGRAPH	8203	8204	8206	8207	8208
FOIL THICKNESS (Å)	750	750	750	750	750
MAGNIFICATION (kX)	521	779	353	665	665
NUMBER OF VOIDS COUNTED	626	278	2006	542	522
MEAN DIAMETER (Å)	30.6	32.6	40.2	41.3	41.6
MEDIAN DIAMETER (Å)	27.7	29.3	35.9	38.9	38.9
MEAN AREA x10^{3} (Å^{2})	.96	1.1	1.5	1.7	1.7
MEAN VOLUME x10^{5} (Å^{3})	.38	.48	.66	.8	.82
VARIANCE (Å^{2})	151.1	192.7	98.5	185.0	190.8
STANDARD DEVIATION (Å)	12.3	13.9	9.92	13.6	13.8
SKEWNESS	.91	.90	.76	.16	.22
KURTOSIS	4.07	4.35	3.88	2.45	2.47
VOLUME FRACTION (%)*	.188	.248	.504	.575	.582
# DENSITY x10^{22} (v/m^{3}) *	5.0	5.2	7.6	7.2	7.1

* Estimated - see text

TABLE 11

VOID SIZE DISTRIBUTION IN SAMPLE I

MICROGRAPH	12269	12271	12274	12494	12497	12500
FOIL THICKNESS (Å)	700	700	550	575	575	575
MAGNIFICATION (kX)	348	348	447	447	496	360
NUMBER OF VOIDS COUNTED	420	379	165	264	157	164
MEAN DIAMETER (Å)	47.65	50.57	54.83	50.72	35.73	58.52
MEDIAN DIAMETER (Å)	41.38	44.25	54.83	44.76	33.03	51.94
MEAN AREA x10^3 (Å^2)	2.2	2.4	2.9	2.5	1.3	3.3
MEAN VOLUME x10^5 (Å^3)	1.2	1.4	1.8	1.4	.55	2.2
VARIANCE (Å^2)	207.4	191.1	241.6	226.1	160.4	310.6
STANDARD DEVIATION (Å)	14.4	13.8	15.5	15.0	12.7	17.6
SKEWNESS	1.06	1.07	.75	.75	.81	.75
KURTOSIS	4.04	4.13	3.39	3.71	3.13	2.77
VOID VOLUME FRACTION (%)	.224	.232	.315	.299	.130	.239
VOID NUMBER DENSITY x10^{22} (v/m^3)	1.9	1.7	1.8	2.1	2.4	1.1

TABLE 12

VOID SIZE DISTRIBUTION IN SAMPLE C_1

MICROGRAPH	9340	9343	9346	9347	9348
FOIL THICKNESS (Å)	300	300	300	300	300
MAGNIFICATION (kX)	469	469	623	623	911
NUMBER OF VOIDS COUNTED	1234	880	500	587	214
MEAN DIAMETER (Å)	38.8	41.7	41.6	35.2	44.6
MEDIAN DIAMETER (Å)	34.9	37.3	36.6	30.0	42.0
MEAN AREA $\times 10^3$ ($Å^2$)	1.4	1.7	1.7	1.3	1.9
MEAN VOLUME $\times 10^5$ ($Å^3$)	.62	.78	.88	.58	.95
VARIANCE ($Å^2$)	124.6	142.8	231.7	213.0	184.6
STANDARD DEVIATION (Å)	11.2	11.9	15.2	14.6	13.6
SKEWNESS	1.10	.75	.67	.74	.41
KURTOSIS	4.88	3.73	2.89	3.18	2.65
VOID VOLUME FRACTION (%)	1.242	1.344	1.248	.940	1.331
VOID # DENSITY $\times 10^{23}$ (v/m^3)	2.0	1.7	1.4	1.6	1.4

TABLE 13

VOID SIZE DISTRIBUTION IN SAMPLE C_2

MICROGRAPH	12513	12516
FOIL THICKNESS (Å)	275	275
MAGNIFICATION (kX)	490	563
NUMBER OF VOIDS COUNTED	467	357
MEAN DIAMETER (Å)	45.5	44.3
MEDIAN DIAMETER (Å)	40.8	37.8
MEAN AREA $\times 10^3$ ($\mathring{A}^2$)	2.0	1.9
MEAN VOLUME $\times 10^5$ ($\mathring{A}^3$)	1.1	1.0
VARIANCE ($\mathring{A}^2$)	223.3	207.4
STANDARD DEVIATION (Å)	14.9	14.4
SKEWNESS	.76	.81
KURTOSIS	3.35	3.36
VOID VOLUME FRACTION (%)	1.37	1.38
VOID # DENSITY $\times 10^{23}$ (v/m^3)	1.3	1.4

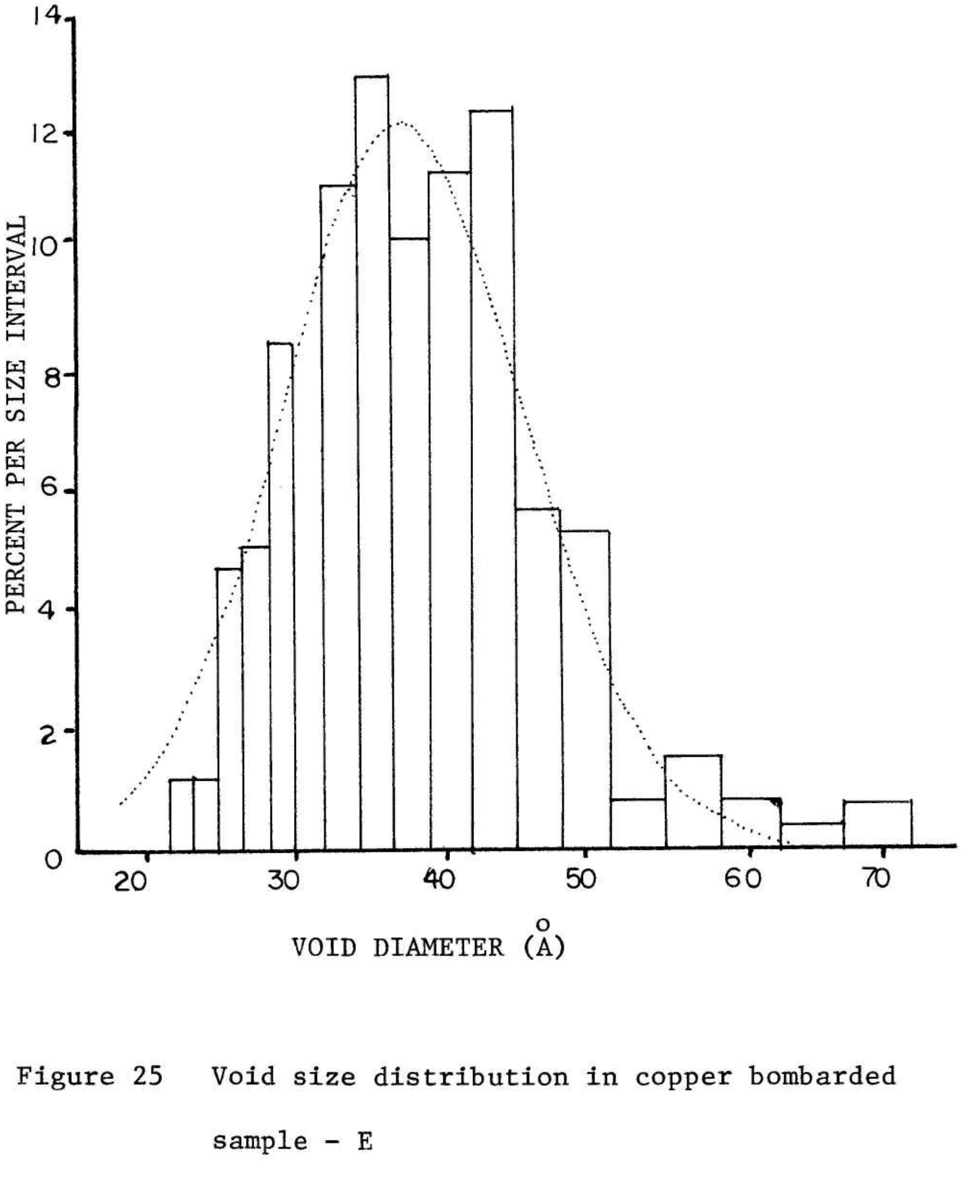

Figure 25 Void size distribution in copper bombarded sample - E

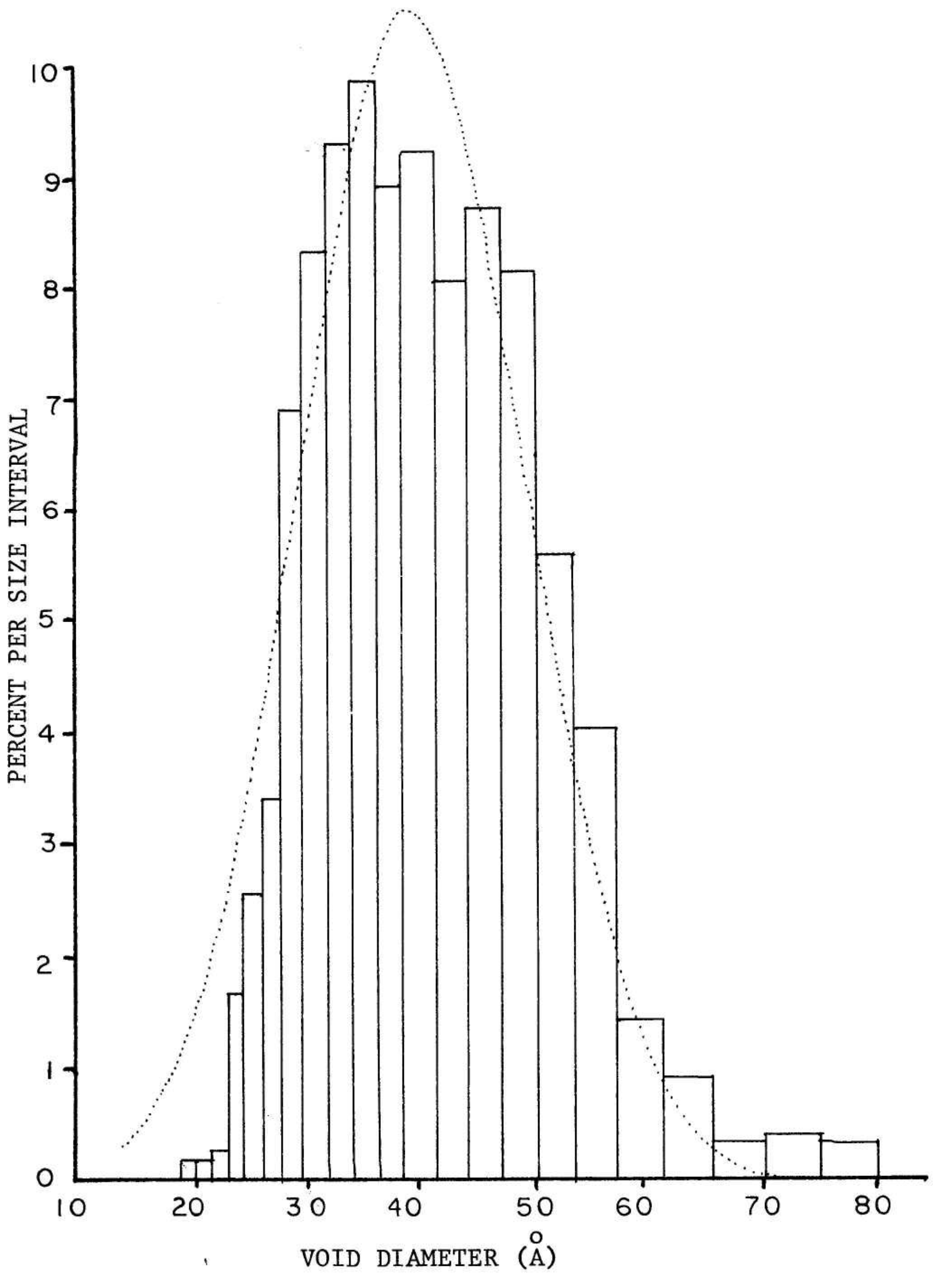

Figure 26 Void size distribution in copper bombarded sample - F

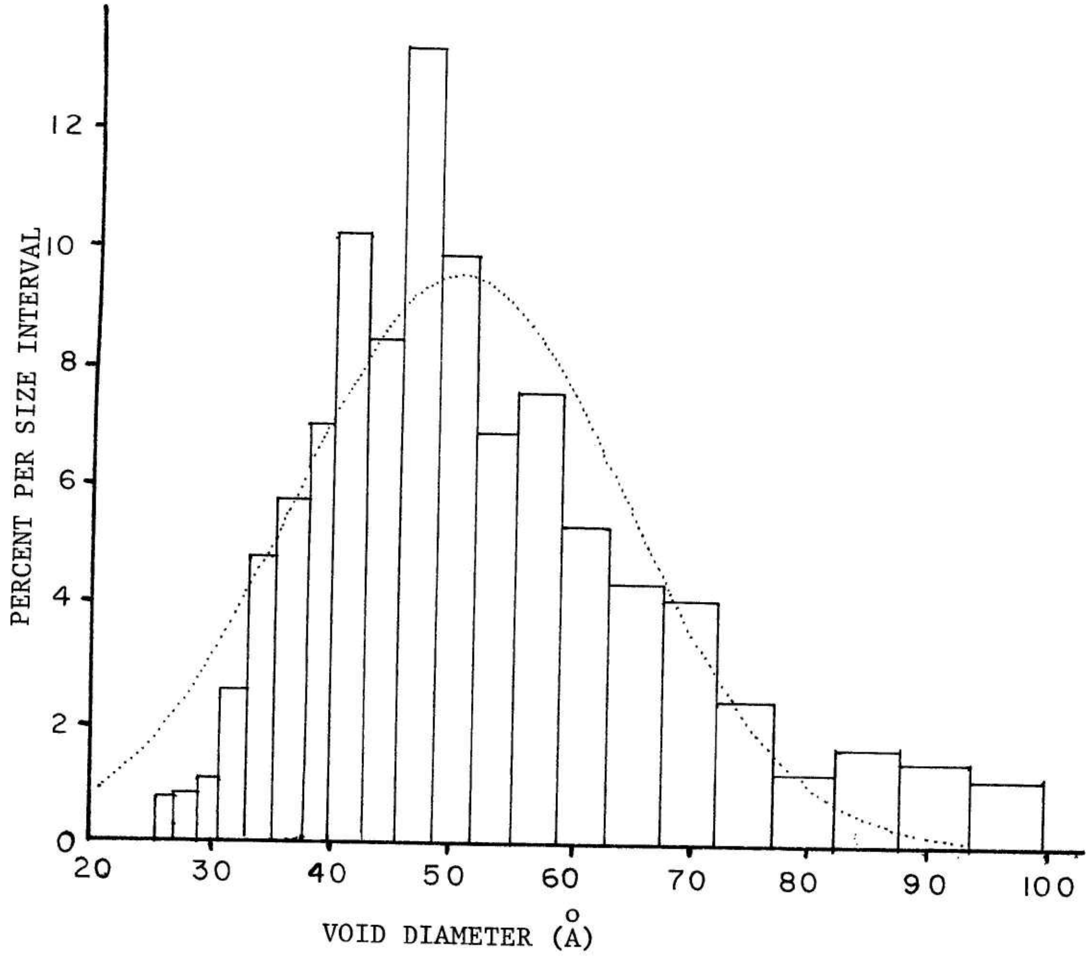

Figure 27 Void size distribution in copper bombarded sample - I

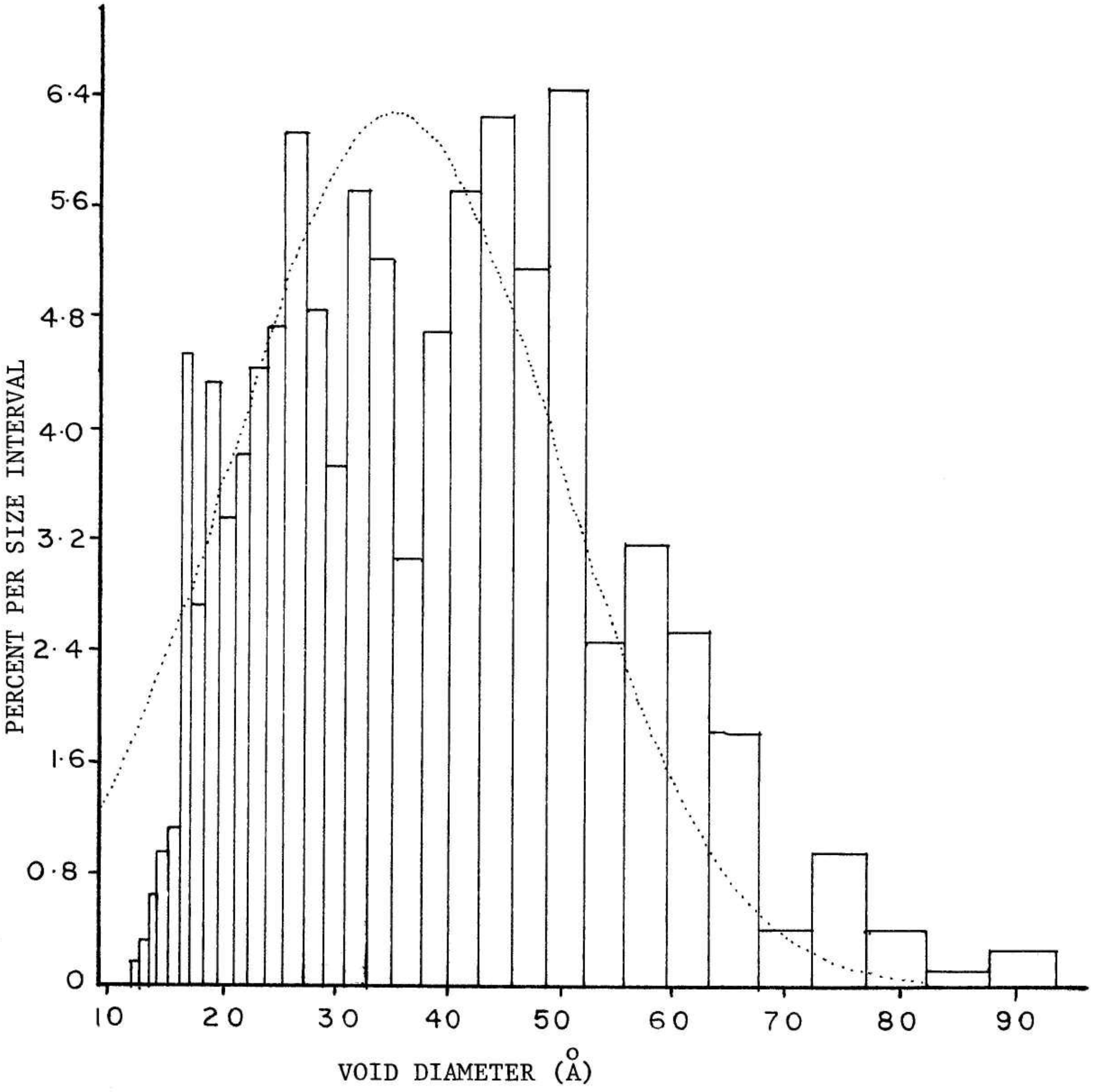

Figure 28 Void size distribution in selenium bombarded sample - C_1

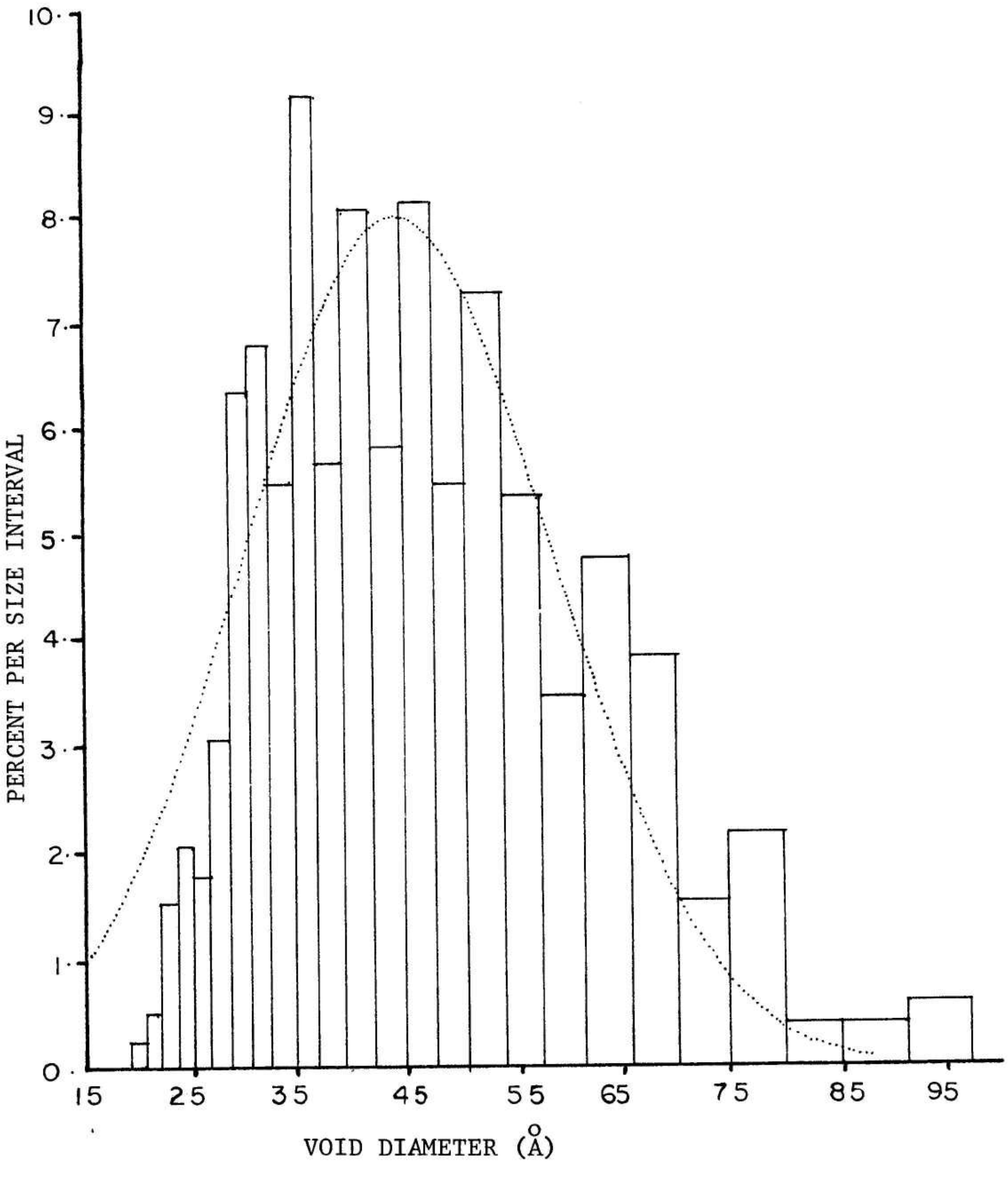

Figure 29 Void size distribution in selenium bombarded sample - C_2

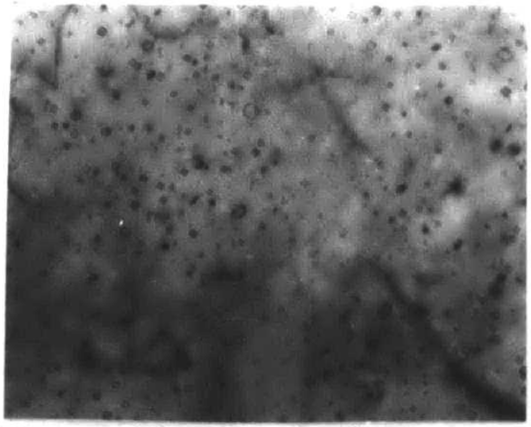

Figure 30 Typical microstructure in copper ion bombarded sample F (magnification = 205kX)

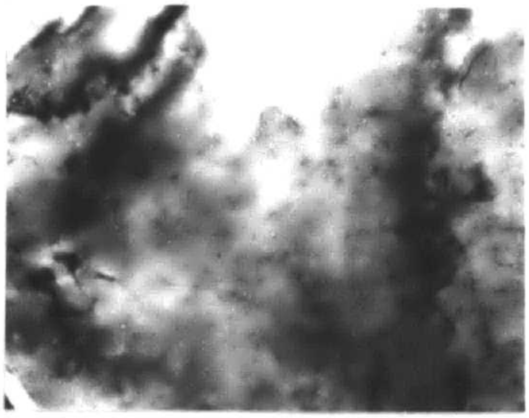

Figure 31 Typical microstructure in copper ion bombarded sample I (magnification = 150kX)

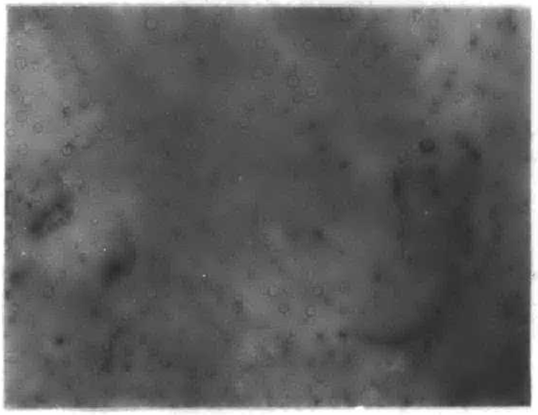

Figure 32 Typical microstructure in selenium ion bombarded sample C_1

(magnification = 186kX)

Figure 33 Typical microstructure in selenium ion bombarded sample C_2

(magnification = 175kX)

estimate of the thickness of 750 Å was made. This affects the number density and volume fraction directly. With a high degree of probability, the sample thickness is between 500 and 1000 Å. The modified parameters are shown in a footnote in Table 8.

The results obtained by the other participants in the study are given in Appendix 5. The other labs which had reported and the ions used are as follows:

(1) PNL 5 MeV Ni^{++}

(2) NRL 3.2 MeV Mo^{+}

(3) U. Wisc. 17 MeV Cu^{4+} and

(4) AI .5 MeV H^{+}

4.6. Errors in Size Distributions

The possible errors in the size distribution will be listed and briefly discussed below.

(1) The samples were not always thinned to the exact peak of the damage curve. The actual magnitude of this error is unknown, but the effect is believed to be small. For example, in the case of copper ions, if the depth thinned is off by as much as .1μ, the damage level will vary by less than 4.7%. The concentration of deposited ions, however, will vary by -71% to +149%, depending upon which side of the peak is reached.

(2) Specimen damage in handling. There were many occasions for specimen damage during the handling steps. In many samples, surface contamination and localized bending greatly reduced the areas available for examination. This leads to the possibility of doubt as to whether

these areas were truly characteristic of the entire sample.

(3) Microscope calibration errors: magnification and rotation. These errors are probable very small. Although the characteristics of microscopes change with age, the calibrations used were recent enough that the errors would be minor.

(4) Thickness determination. Tilt stages on TEM's are typically inaccurate. The thickness calculated depends strongly on the tilt angle between elements of a stereo pair. A ± 10% error in tilt (about a tilt angle of 12°) yields an error in thickness of approximately the same amount.

(5) Errors in measuring void sizes. This type of error has several sources: (a) miscounting--such as counting a void twice (believed to be minimal); (b) missing the exact size (also believed to be minimal); (c) noise in micrograph (contrast fluctuations or precipitates that have the appearance of voids) and (d) fuzziness and contrast problems. On micrographs that were not in sharp focus or flat in contrast, some voids (notably the smaller ones) were lost in the background. There is no way to estimate the magnitude of the last two problems, but careful use of the particle size analyzer would tend to remove most of them. It was found that after spending time measuring the void sizes, the operator becomes very proficient in discriminating between the voids and features with a similar appearance.

CHAPTER 5

DISCUSSION

The specimen preparation technique adopted in this study, controlled front surface removal followed by penetration from the back surface, was found to be satisfactory for the examination of ion induced damage by transmission electron microscopy. The key step to this process is the accurate removal of a predetermined amount of the front surface. Although the technique used gave good results, it is felt that further work to develop the laser interferometric system for use with molybdenum samples would be worthwhile. Aside from the additional time required, the extra handling steps involved in the iterative technique (with either the Micro-Michelson or Tolansky interference microscopes) have a large potential for producing damage in the samples. The laser interferometer system, with real time measurements of polishing depth, avoids this and would lead to more accurate results. For the case of molybdenum, the discovery of an electrolyte that minimizes the formation of MoO_5 would make this technique useable.

Another procedure that was found useful for specimen preparation was the use of the ion mill for samples that did not have adequate thin area. Jet electropolishing commonly has a significant failure rate. With a very limited quantity of samples available, it is important that the majority be useable. The use of the ion mill was found to be an excellent technique to redeem inadequate samples, as it was found to produce the required thin area with a minimum of specimen damage.

The considerations mentioned previously for high resolution microscopy were found to be very important, especially in those samples exhibiting minimal thin area. By taking care to ensure that minimum specimen contamination occurs, the maximum useable area will be encountered. On several of the samples, appreciable areas were lost before the proper procedures were developed.

Since the voids were small, their identification as voids was rather difficult. The use of a through focal series at a relatively low magnification (∿50 KX) was found to be very helpful. As the objective lens passes through the in-focus condition, the void contrast reverses. This is relatively easy to see on the screen. Once the voids were located, the magnification could be slowly increased without their loss. With the range of enlargement available in the printing process, a magnification of at least 75 kX must be used in order to achieve sufficient spatial resolution for the particle size analyzer. The accuracy of the diameter measurement increases greatly with increasing void size. Unfortunately, as the magnification increases, the statistical population decreases. This was offset by measuring a sufficient number of voids for an acceptable confidence limit.

The foil thickness measurements by the stereo parallax technique were successful, but led to a high degree of operator fatigue. Due to the nonoptimal nature of many of the stereo pairs, there was difficulty in matching voids from the two views, without the inclusion of non-void features or incorrect pairing. It is probable that a significant number of the initial parallax measurements were in error, since the measurements were not made under the stereo viewer. These were only detected later, after the apparent height differences were calculated. The largest values were checked for the above errors. These problems could have been sidestepped with the use of a device designed for this type of measurement--a Hilger-Watt floating spot mirror stereoscope. Here, the measurement of parallax is performed directly in the stereo viewer by varying the apparent height of a marker to match the void. The results obtained with this method tend to be more reliable.

The microscopy revealed that the irradiations with both Cu^{++} and Se^{++} ions at 900°C produced a large number of small voids (10-100 Å in diameter), fairly homogeneously distributed. The void size distributions were nearly normal in shape. One interesting feature was noted: the high dose samples yielded a smaller average void diameter than the lower dosage ones, contrary to what would be expected. The magnitude of this difference (37 Å vs. 44.7 Å for copper, 40.4 Å vs. 44.9 Å for selenium) is not highly significant--primarily since the majority of the data for the high dose samples was obtained from the high resolution TEM. This allowed the clear identification of very small voids (for the other samples, there was a background noise problem), biasing the apparent average diameter to lower values.

Selenium ion irradiation was found to produce a much higher void number density and volume fraction than copper ions, even allowing for the possible inaccuracies in sizing techniques mentioned earlier. As shown in Appendix 5 (especially in Fig. A-5.1), copper ion irradiation was found by other participants to produce a significantly lower void volume fraction than Ni, Mo or proton irradiation. A possible explanation for this would be the affinity of copper for a face-centered cubic lattice. When implanted in a BCC lattice, the copper atoms would act as trapping sites for vacancies, decreasing their probability of arriving at a void and increasing the likelihood of recombination with an interstitial. Copper has been shown to have the same effect in BCC Iron.

These results have also shown that the presence of He (or other gas) is not a prerequisite for void nucleation. A high void density was produced without the preinjection of gas. As has been shown in many investigations, the presence of gas may greatly aid the nucleation process by balancing the surface tension of a void embryo, but is not absolutely necessary.

Theoretical calculations were made for both the steady state void nucleation rate and terminal void number density by the use of Russell's theory outlined on Section 2.2. This theory is interesting, as it contains no adjustable parameters, as do the others. All of the terms are measurable properties of the material, with the possible exception of the surface energy. The surface energy of a material is sensitive to impurities--especially those that have undergone surface adsorption. For this reason, the calculations were repeated for a surface energy reduced by 20% of that for the pure metal. Reasons for this approach will be given below. The dislocation density (not measured in this experiment) was taken as the average of the results reported from other sites. The other materials parameters were taken as the accepted values listed in the literature.

The results of these calculations are listed in Table 14. As can be seen, the calculated terminal void number densities using an

TABLE 14

THEORETICAL VOID NUCLEATION RATES AND TERMINAL NUMBER DENSITIES

	K (dpa/s)	γ^*	J_s^o (v/cm^3s)	ρ_c (v/cm^3)	ρ_{exp} (v/cm^3)
COPPER SAMPLES	$3.2x10^{-3}$	γ_1	$1.77x10^4$	$5.6x10^{19}$	$4.3x10^{22}$
"	$3.2x10^{-3}$	γ_2	$1.23x10^{12}$	$4.0x10^{22}$	$4.3x10^{22}$
SELENIUM SAMPLES	$2.5x10^{-3}$	γ_1	$5.0\ x10^3$	$3.4x10^{19}$	$1.5x10^{23}$
"	$2.5x10^{-3}$	γ_2	$5.7\ x10^{11}$	$2.8x10^{22}$	$1.5x10^{23}$

* γ_1 = Surface energy of pure molybdenum
$\gamma_2 = .8\gamma_1$ to account for surface effects

	PARAMETER	VALUE		SOURCE
T	TEMPERATURE	900^oC		
Ω	ATOMIC VOLUME	$1.55\ x10^{-23}$	$cm^3/atom$	
γ_1	SURFACE ENERGY	1491	$ergs/cm^2$	(40)
γ_2	REDUCED SURFACE ENERGY	1193	$ergs/cm^2$	
D_v	VACANCY DIFFUSION COEFFICIENT	$4.34\ x10^{-10}$	cm^2/sec	(42)
D_i	INTERSTITIAL DIFFUSION COEFFICIENT	.1	cm^2/sec	(41)
C_v^e	EQUILIBRIUM VACANCY CONCENTRATION	$8.7x10^{-10}$	v/cm^3	(42)
ρ_d	DISLOCATION DENSITY	$4.\ x10^9$	d/cm^3	(26)
α	RECOMBINATION PROBABILITY	$10^{17}D_i$		(41)
Z_v	DISLOCATION BIAS FOR VACANCIES	1		(41)
Z_i	DISLOCATION BIAS FOR INTERSTITIALS	1.05		(41)

uncorrected surface energy are about three orders of magnitude lower than measured. Considering the range of values obtainable in nucleation calculations (at the high temperature limit of void swelling, the calculated nucleation rate may be on the order of 10^{-88} voids/cm^3 sec), this is not a large discrepancy. The set using a reduced surface energy yield results that are in excellent agreement with the measured data.

The value of surface energy used for the original calculations was for pure molybdenum. Even small amounts of impurities have been known to significantly lower the surface energy of a material, especially if they exert some influence of the surfaces. The faceting mentioned earlier provides evidence for this. The voids produced when using Mo ion irradiation (no impurities implanted) exhibit facets of nearly equal size. In the case of Cu^{++} or Se^{++} irradiation, this was not true. The (200) facets were substantially larger than the $(1\bar{1}0)$. It seems very likely that this was produced by a change in surface energy caused by the impurity atoms that are either implanted near or migrate to the surface of the voids (39), although it may be due to another effect, possibly kinetic. The value chosen for the reduction in surface energy (20%) seemed to be a reasonable estimate, in lieu of any value available in the literature.

From the small changes in the void number density between the high and low dosage samples (less than a factor of a 3), it seems very likely that void nucleation has ceased within the damage levels encountered in this experiment. This conclusion agrees with the calculation mentioned above, of the terminal void number density. This implies that any swelling past the 2 dpa damage level was due to growth and coalescence of existing voids. In light of this, it is felt that the observed slight decrease in average void size with increased damage is most probably an artifact of the measuring procedure.

CHAPTER 6

CONCLUSIONS

1. Controlled front surface removal followed by penetration from the back surface was found to be a satisfactory preparation technique for the examination of ion-induced damage in the TEM.

2. Pulsed electropolishing followed by interferometric microscopy to measure the step height was sufficiently accurate to allow examination of the desired depth in the sample ($\sim .75\mu$).

3. A large void number density ($.18\text{-}1.6 \times 10^{23}$ v/m^3) was induced in the molybdenum samples by Copper or Selenium ion irradiation without the presence of inert gas.

4. The void size distribution was nearly normal in shape.

5. The voids were found to have a faceted nature--most probably cubo-octahedral in shape.

6. Selenium ion irradiation was found to produce a much higher void density than copper ions ($\sim 1.5 \times 10^{23}$ vs. $\sim 4. \times 10^{22}$ v/m^3).

7. Void nucleation had probably ceased during the time scale of the irradiations.

8. Theoretical calculations of the terminal void number density agreed well with the experimental data--especially those with a surface energy reduced by 20% from the literature value for molybdenum.

APPENDIX 1

DAMAGE CALCULATIONS

In order to ensure consistency amongst the participants of the round robin study, the damage calculations were to be calculated by the EDEP-1 computer code of Manning and Mueller (35). The displacement calculations were to be in accordance with the report of Doran et al. (36). The correction factor for the Kinchen-Pease model (β) was to be equal to .8 and the effective displacement energy (E_d) to be 62 eV.

EDEP-1 considers an energetic heavy ion beam striking a target. The target is assumed to be amorphous and may be composed of up to six components. The routine calculates various ion range parameters and the depth profile of energy deposition into the target. Both the total energy deposited as well as that responsible for displacements are considered. The total energy loss may be split up into two components: elastic and inelastic. The inelastic collisions affect primarily the electrons of a struck atom. This excitation is eventually dissipated as heat without causing radiation damage--although it may enhance localized annealing. The elastic collisions involve momentum transfer to the struck atoms, resulting in the production of PKA's--as long as the energy transferred is greater than E_d.

The ion range parameters play an important role in the calculations. The appropriate parameters are defined in Fig. A-1.1. A Gaussian distribution in projected range is assumed:

$$f(x) = \frac{1}{\sqrt{2\pi}\,\alpha_x} \exp\left(-\frac{(x-x_m)^2}{2\alpha_x^2}\right) \qquad \text{A-1.1}$$

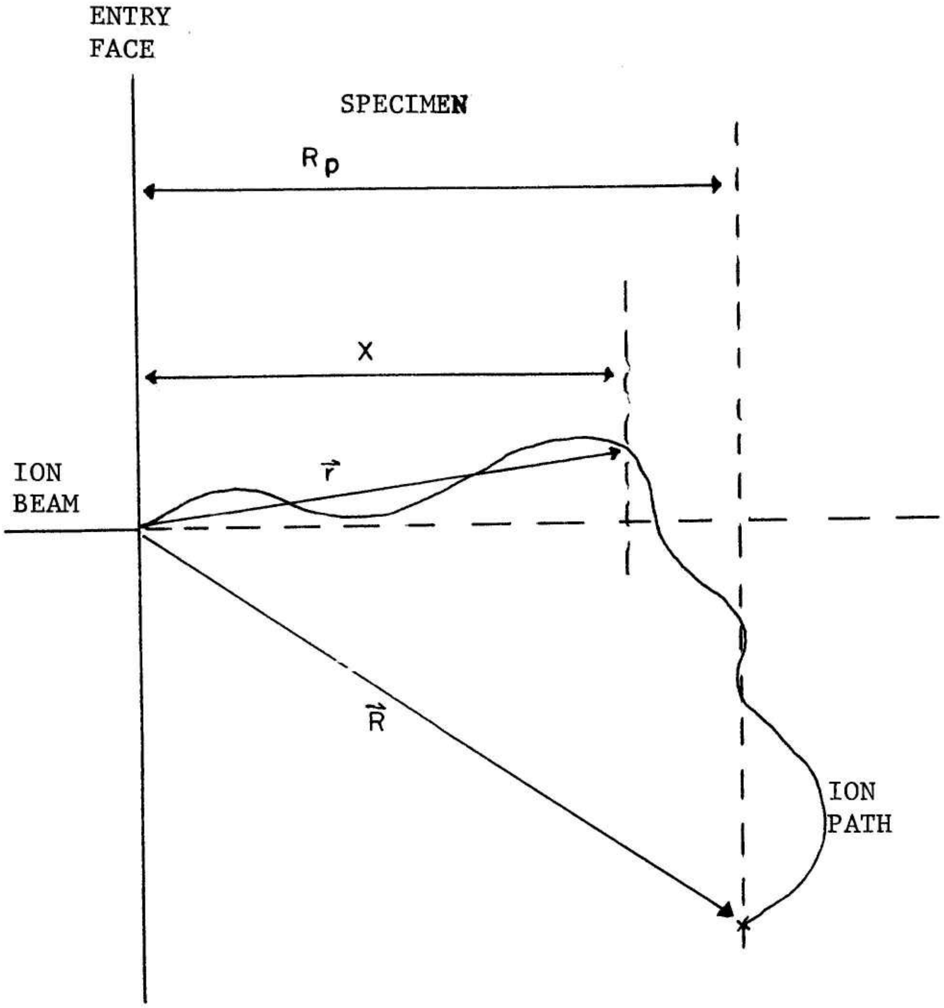

R = Range

R_p = projected range

Figure A-1.1 Range parameters

where f(x) = fraction of beam ions with projected range in the neighborhood dx of x, x_m = mean projected range and α_x = standard deviation in projected range. x_m and α_x are computed by the routine of Johnson and Gibbons, which takes into account range straggling by the LSS theory. This straggling is due to the different paths taken by individual ions, causing a spread of the energy of the ions at any given depth. All of the energy deposition relations will be dependent upon this function.

Two energy distributions are calculated by the remainder of the code. $S_B(x)$, the profile of energy deposited into the creation of PKA's by beam ions, takes into account inelastic energy losses of the ions, but ignores the fact that the PKA's and the displacement cascades that they create also undergo inelastic collisions. This introduces an overestimation of the energy available for displacements, although it is a good measure of the total energy loss of the beam. $S_D(x)$ takes into account all of the inelastic collisions and is therefore the appropriate factor for displacement calculations.

Manning and Mueller took the assumption that $S_B(x)$ is related to the known range distribution f(x) by:

$$S_B(x) = \int_x^\infty f(x')S_n(E_1(x'-x) \frac{\partial R(x')}{\partial x'} \partial x' \qquad \text{A-1.2}$$

where $S_B(x)dx$ = average energy deposited into the creation of PKA's as the ion traverses the projected distance dx.

$E_1(x)$ = average energy of an ion whose projected range is x.

$S_n(E)dR$= average energy loss into elastic collisions by an ion of energy E as it travels a total path length of dR.

$R(x)$ = total range of an ion--considered as a function of projected range (x).

E_1, S_n and dR/x are obtained from the Johnson and Gibbons routine.

$S_D(x)$ is calculated in much the same fashion, but utilizes the Linhard partition theory to take into account the inelastic collisions of the primary and secondary knock-on atoms.

$$S_D(x) = \int_x^{\infty} f(x')S_L(E_1(x'-x)) \frac{\partial R(x')}{\partial x'} \partial x' \qquad \text{A-1.3}$$

where

$$S_L(x) = \int_{T=T_1}^{T=T_m} T\eta(T)\partial\sigma(T) \qquad \text{A-1.4}$$

T = energy transferred to a PKA in an elastic collision by an ion of energy E, T_1 represents the displacement energy (this is sufficiently small 25-50 eV, that it can be taken as $T_1=0$), T_m=maximum energy transfer allowed by kinematics. The factor $\eta(T)$ is given by the Linhard theory and represents the fraction of PKA energy T dissipated into elastic processes. $\sigma(T)$ is the Linhard scattering cross section. Fig. A-1.2 shows $S_D(x)$ vs x for 5 MeV Se^{++} ions bombarding Mo.

To calculate the total number of displacements, Doran et al. (36) recommend the use of the modified Kinchen-Pease formula:

$$\begin{array}{ll} N_d = 0 & T<E_d \\ N_d = 1 & E_d \leq T < 2E_d \\ N_d = T_{dam}/2\ E_d & T \geq 2E_d \end{array} \qquad \text{A-1.5}$$

where N_d = average number of displacements produced in a collision

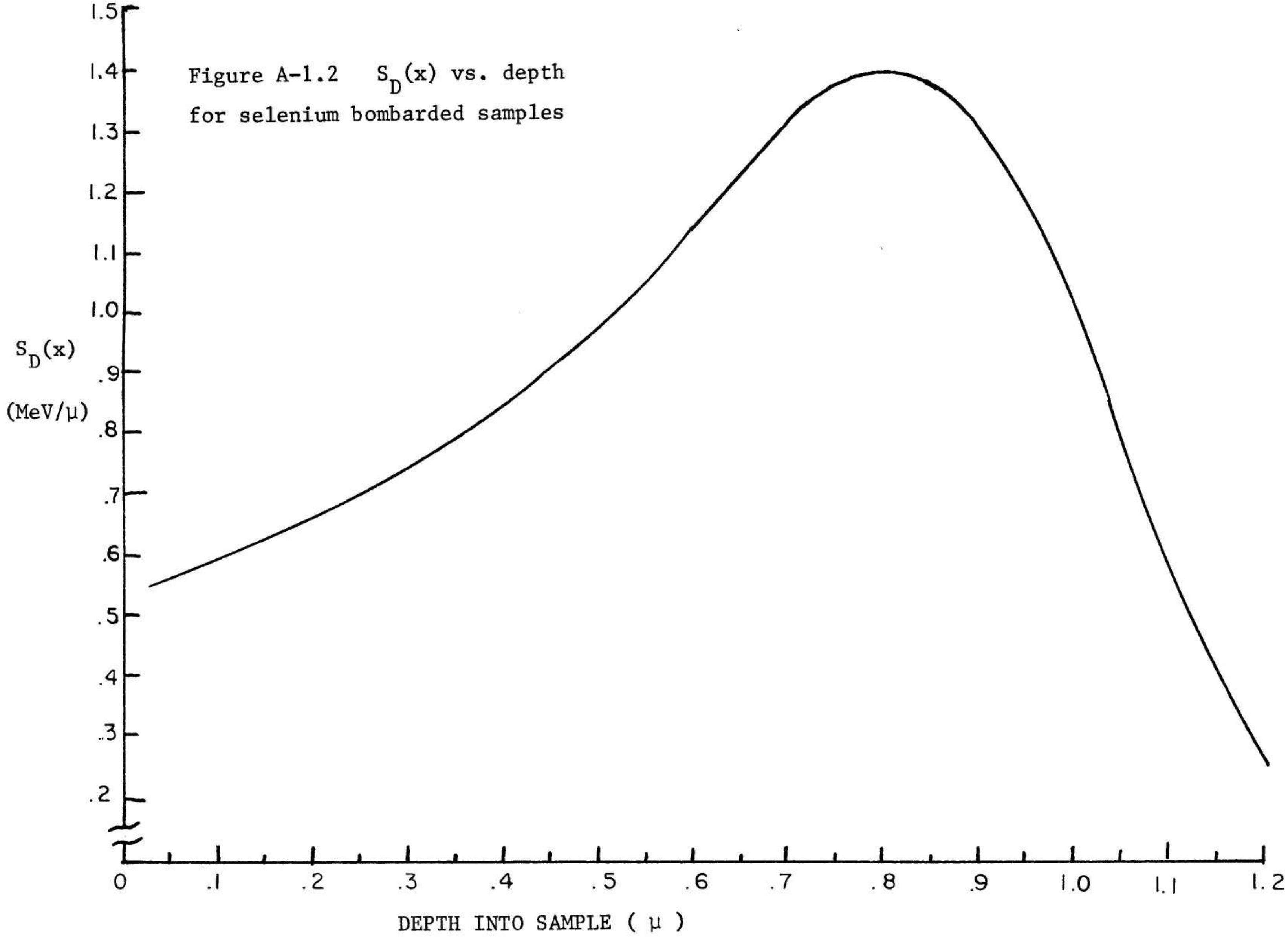

Figure A-1.2 $S_D(x)$ vs. depth for selenium bombarded samples cascade. T_{dam} may easily be obtained from $S_D(x)$.

Doran estimates the errors involved in the above procedure as follows:

1. The uncertainties in the LSS theory gives rise to an inaccuracy in the energy deposition function of ± 20%. This is compounded by the large change of dE/dx through a TEM sample in addition to uncertainties of sample location and thickness. This adds another ±15% in uncertainty.

2. Swelling is not taken into account in the models. The effects of this are unknown.

3. The secondary displacement model adds another 30%.

4. Energy transport away from the collision location is not considered. This is estimated to introduce another 15%.

The total estimated uncertainty in calculated displacements is ∿45% in the region of slowest varying dE/dx. In regions where dE/dx changes more rapidly, such as near the end-of-range, this is expected to rise to ±50%.

The following is a sample calculation of the damage level and Selenium concentration in sample A_1 at a depth of $.8\mu$.

f(x) from Eqn. A-1.1 is the fraction of beam ions with projected range in the neighborhood dx of x. The total number of ions hitting the sample is:

$$\#\text{ of ions} = \bar{I}\ t\ F/2 \qquad \text{A-1.6}$$

where $\bar{I}$ = average current, t = irradiation time and F/2 is the Faraday constant divided by the charge on the ions. The total number of ions deposited at depth x will be:

$$\# \text{ of ions @ } x = f(x) \ \Delta x \ \bar{I} \ t \ F/2 \qquad \text{A-1.7}$$

This must be corrected to atom percent. The number of Mo atoms in the volume to be considered is:

$$\# \text{ of Mo atoms} = \Delta x \ \pi r_a^2 \ \rho \qquad \text{A-1.8}$$

where r_a = aperture radius and ρ = atom density of Mo.

The final form will be:

$$C_{Se} = 100 \ f(x) \ \Delta x \ \bar{I} \ t \ (F/2)/ \ \Delta x \ \ r_a^2 \rho \qquad \text{A-1.9}$$

Using the following values (appropriate for sample A_1 at a depth of .8):

$\bar{I} = 17 \times 10^{-9}$ Amps

$t = 10020$ seconds

$F = 6.24 \times 10^{18}$ charges/coulomb

$r_a = .1$ cm

$\rho = 6.4 \times 10^{22}$ atoms/cm^3

$x_m = .9909$ (from EDEP-1)

$\alpha_m = .1784$ (from EDEP-1)

results in: $C_{Se} = .332$ a/o

Eqn. A-1.5 yields the total number of displacements per atom--with a little manipulation:

$$N_d = \beta T_{dam}/E_d \qquad \text{A-1.5}$$

now, $T_{dam} = S_D(x) \ \Delta x$, so

$$N_d = \beta S_D(x) \ \Delta x/E_d \qquad \text{A-1.10}$$

As written above, N_d represents the average number of displaced atoms per beam ion in a region Δx wide about a depth x. Again, the number of beam ions is given by Eqn. A-1.6 and the number of Mo atoms in the appropriate volume by Eqn. A-1.8. The final relation for displacements per atom is:

$$\mathrm{dpa} = \frac{\beta S_D(x)\Delta x}{E_d} (ItF/2)/\Delta x \pi r_a^2 \zeta \qquad \text{A-1.11}$$

for sample A_1 at a depth of .8μ, the appropriate values are:

$S_D(x) = 1.410$ MeV/μ (from EDEP-1)
$\beta = .8$
$E_d = 62$ eV

with the other terms remaining as above. This results in a value of 23.57 dpa at this depth.

The results of the calculations are illustrated in Fig. A-1.3 and A-1.4 for selected samples.

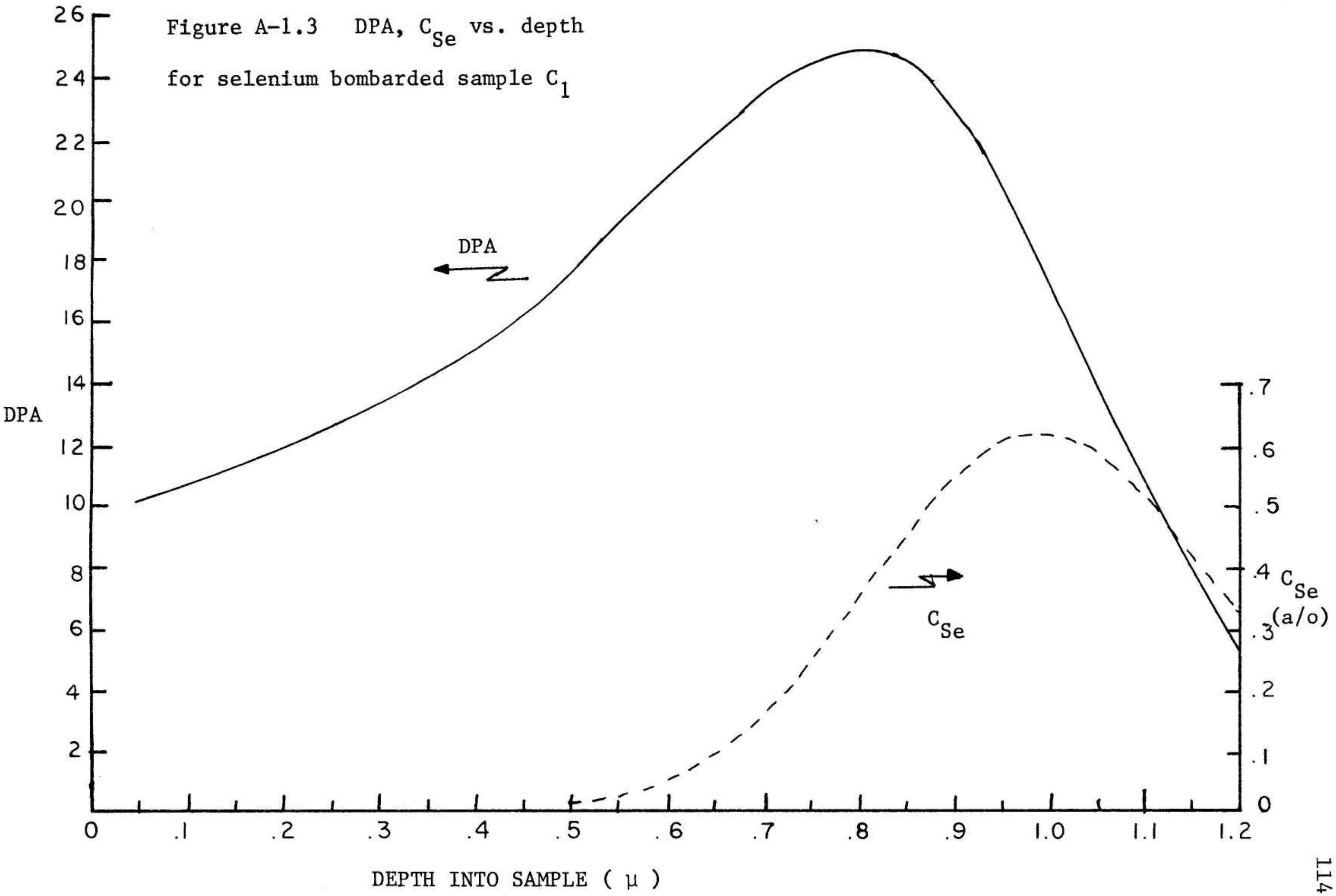

Figure A-1.3 DPA, C_{Se} vs. depth for selenium bombarded sample C_1

Figure A-1.4 DPA, C_{Cu} vs. depth for copper bombarded sample F

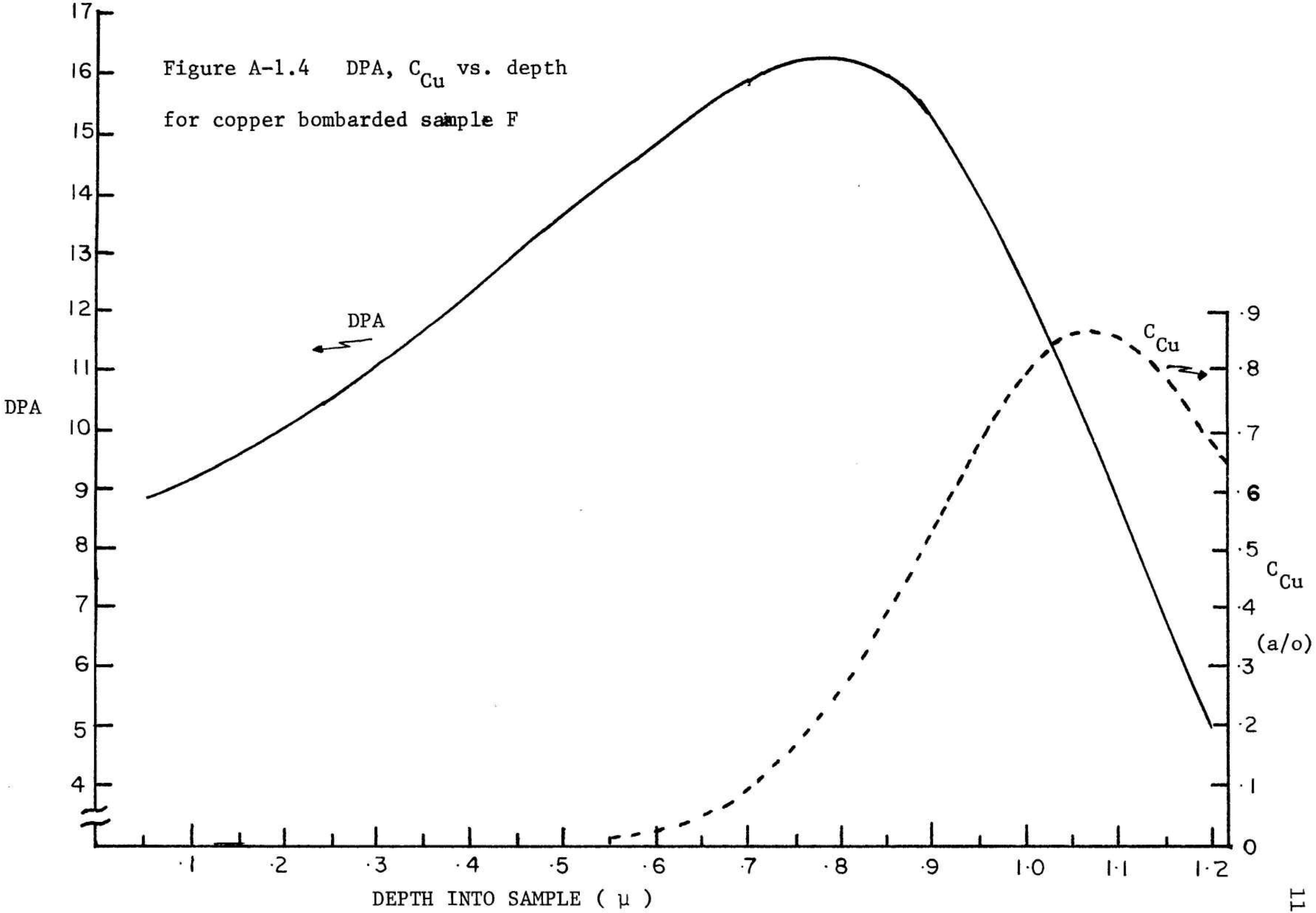

APPENDIX 2

INSTRUMENTATION

In order to control the electropolishing conditions as closely as possible, as well regulated power supply was designed and constructed. This unit has the advantages over the supplies commonly used for polishing of having a constant (selectable) output voltage and the capability of supplying current either steadily or in pulses as short as .05 seconds. With a small amount of modification, it could be converted to a constant current supply.

The schematic is shown in Fig. A-2.1. The power supply is a standard bridge rectifier--capacitor filter circuit, with an output voltage of 35V. A fixed reference voltage of 6.6 V is provided by D_1. Op amp A_1 is used to pass a constant current through D_1 to increase the stability of the circuit. A_2 is used as a voltage multiplier with an output voltage of $V_{out} = V_{in} (R_5+R_6)/R_5$. V_{in} is varied by a voltage divider across the Zener diode. The output current is boosted by Q_1 and Q_2, arranged in a Darlington configuration, with R_7 acting as a sensor for current limiting (2A max). This regulator provides a very stable output voltage.

The pulsing capability is provided by an LM555 integrated circuit (A_4) in an astable multivibrator configuration. Both the period and duty cycle are semi-independently variable, affording a large degree of flexibility in controlling the polishing conditions. Since A_4 has a maximum supply voltage of 30V, a 5V regulator (A_3) was used to reduce this. A reed relay was used to switch the output voltage, as the maximum

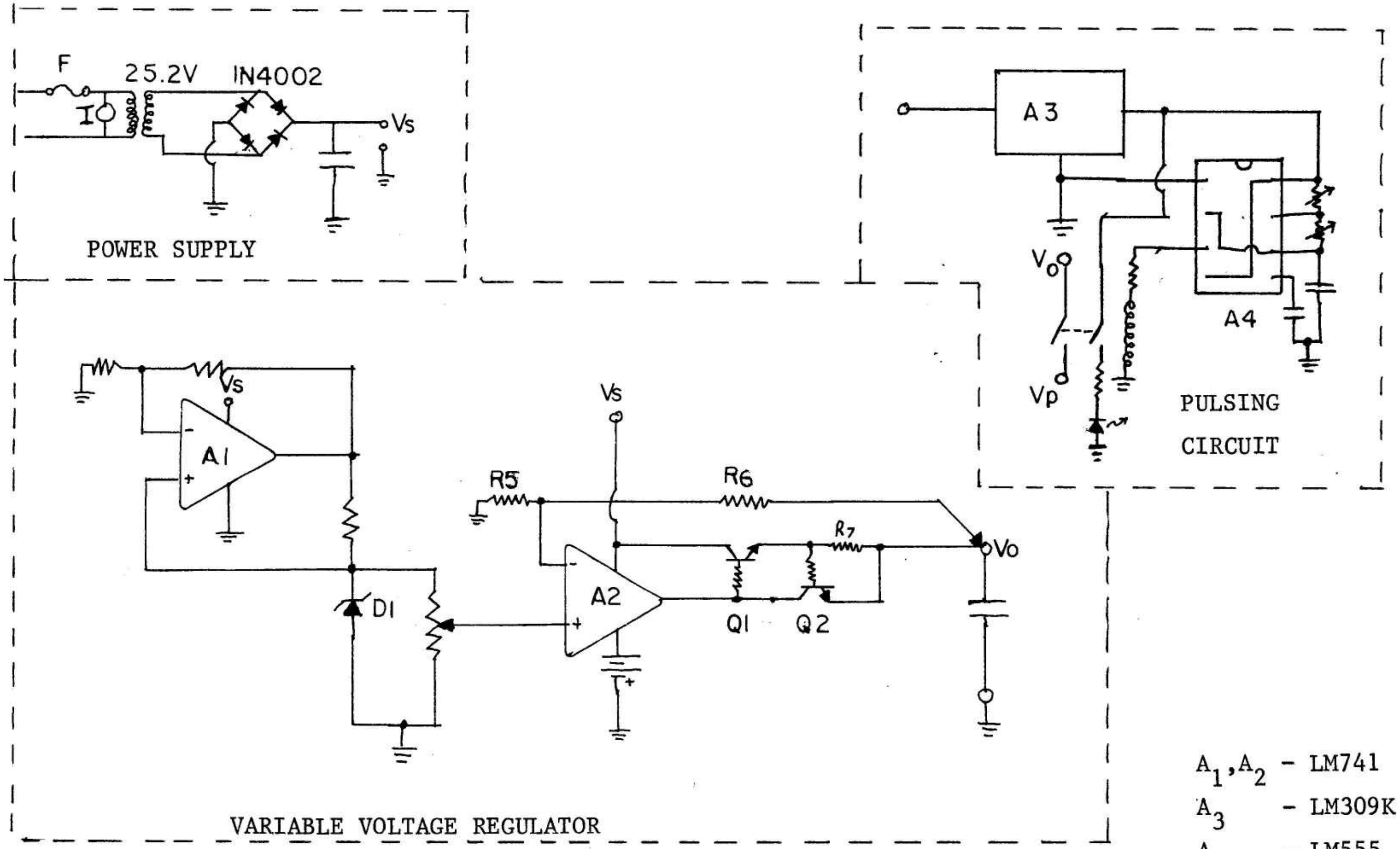

A_1,A_2 - LM741
A_3 - LM309K
A_4 - LM555
Q_1 - 2N3055
Q_2 - 2N3904
D_1 - 6.6V Zener

Figure A-2.1 Schematic of Pulsed Power Supply output current of A_4 is only 300 mA.

During polishing, monitoring instruments were used for the most consistent results. The output voltage was measured with a Weston digital voltmeter. The current was monitored and the pulse conditons were monitored on a Tektronix oscilliscope. It was found that the pulse width could be reduced as low as .05 seconds before evidence of contact bounce was seen.

Initially, when the laser system was to have been used, a fringe shift monitor was constructed. When it became apparent that the interferometer would not function correctly, this circuit was converted to a pulse counter. This freed the operator to pay closer attention to the polishing conditions without having to keep track of the number of pulses. The schematic for this circuit is shown in Fig. A-2.2 & 3.

In the original design--fringe counter--the input was a current passed through a phototransistor. The modification involved substituting a 100K resistor for this, in order to monitor the voltage of the pulsed supply. The input stage consists of three basic circuits: a current to voltage converter (A_1), an inverter (A_2) and a comparator (A_3) to convert the varying analog levels to TTL logic levels with a fast rise time. The pulse output from this section goes to a retrigerable monostable circuit (A_4, A_5 and Q_1) with a selectable on time of 1 or 10ms. This removes the possibility of contact bounce from the pulsing relay to cause errorneous counts.

The pulses from this section go to two stages of conventional decade counters, followed by an overflow indicator (R/S flip-flop). These drive

Figure A-2.2 Schematic of Pulse (Fringe) Counter

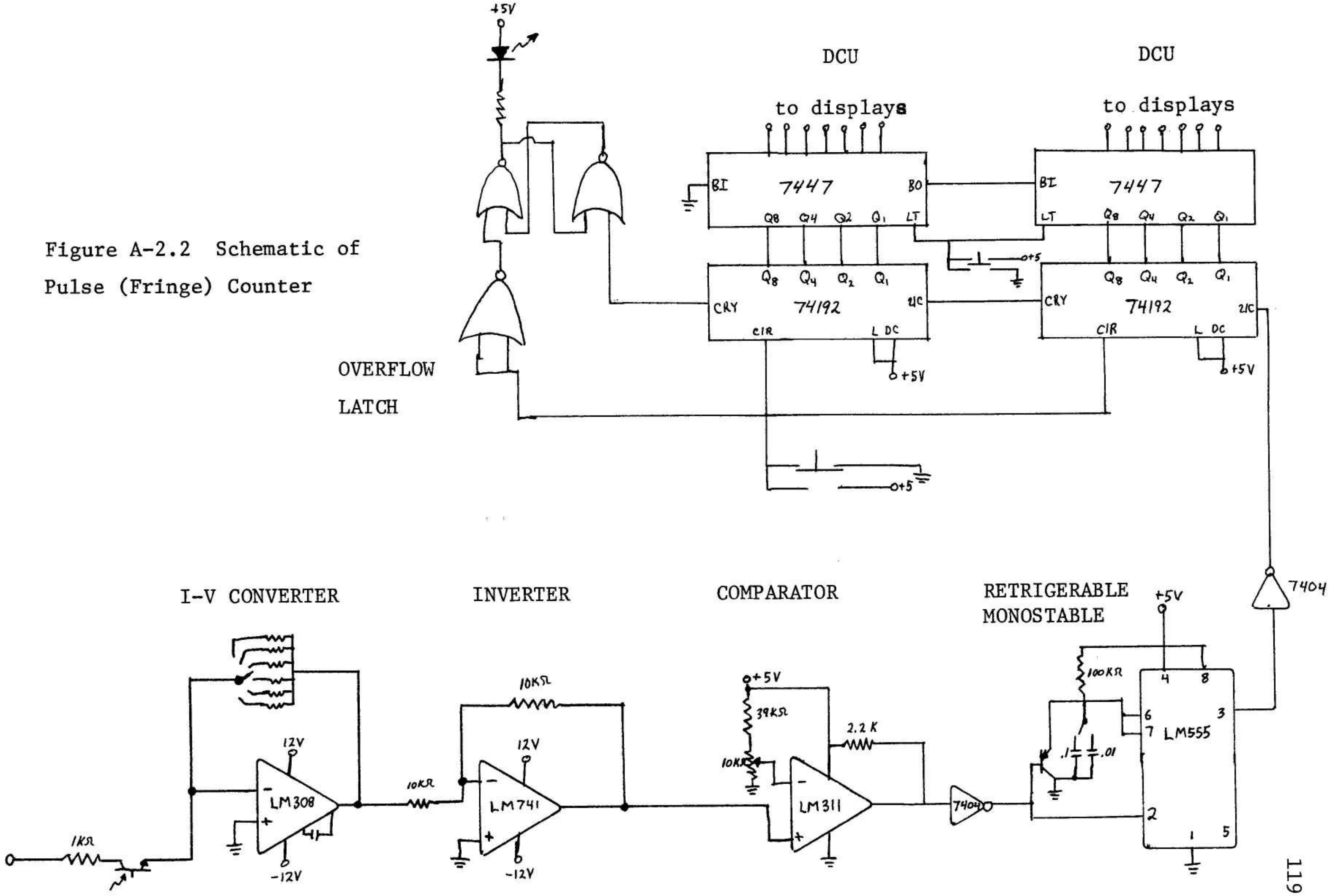

the outout displays. The power supplies (± 12V, 5V) are shown in Fig. A-2.3. These are of conventional design, with three terminal voltage regulators to fix the output voltage.

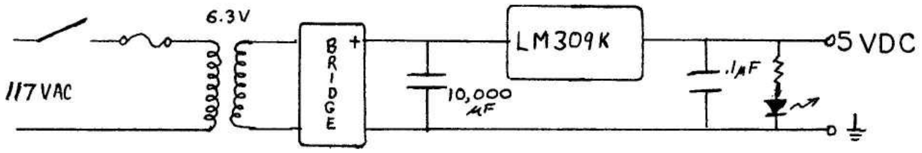

a) LOGIC SUPPLY

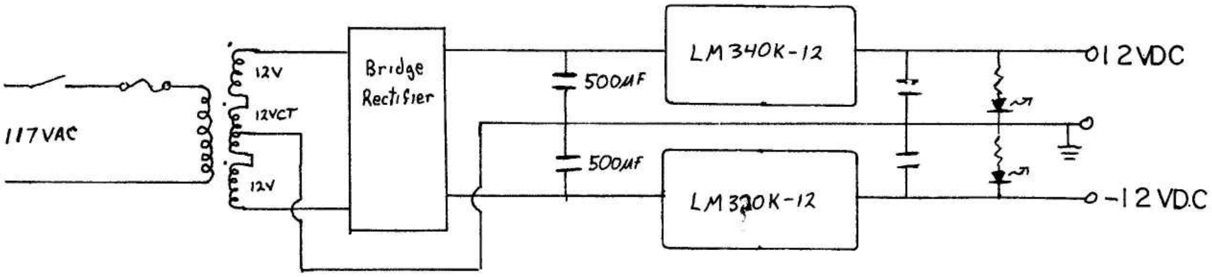

b) BIPOLAR OP-AMP SUPPLY

Figure A-2.3 Schematic of Power Supplies for Pulse Counter Circuit

APPENDIX 3

SHAPE FACTOR CALCULATIONS

The computer routine for analyzing the void size distribution was originally based on spherical voids. For the void shapes encountered in this study (Fig. A-3.1), this assumption would lead to sizeable errors. The easiest way to rectify this was to introduce a shape factor to account for the actual void volume. The convention adopted for determining the void diameter was to measure the diameter of the largest circle capable of being contained within the void projection.

The shape factor for the area will be considered first. Fig. A-3.2 shows the appropriate dimensions. The area of this figure will be given by:

$$A = D^2-4(a^2/4) \qquad \text{A-3.1}$$

now,

$$D = b + (2)^{1/2} a \qquad \text{A-3.2}$$

and

$$b \simeq 3/2\ a \text{ (by measurement)} \qquad \text{A-3.3}$$

so:

$$A = .882\ D^2 \qquad \text{A-3.4}$$

This results in: $\text{STRFA} = .882\ D^2/(\pi D^2/4) = 1.123$ A-3.5

where STRFA = area shape factor (area of real shape/area of circle with equivalent diameter).

The volume shape factor is much more difficult to calculate. It was felt that the following approximation would suffice:

1. take the original cube volume (sides of length D),
2. subtract the volumes of edge prisms of length b,
3. subtract the volumes of the remaining corner tetrahedra, and
4. add the volumes of smaller tetrahedra at the corners.

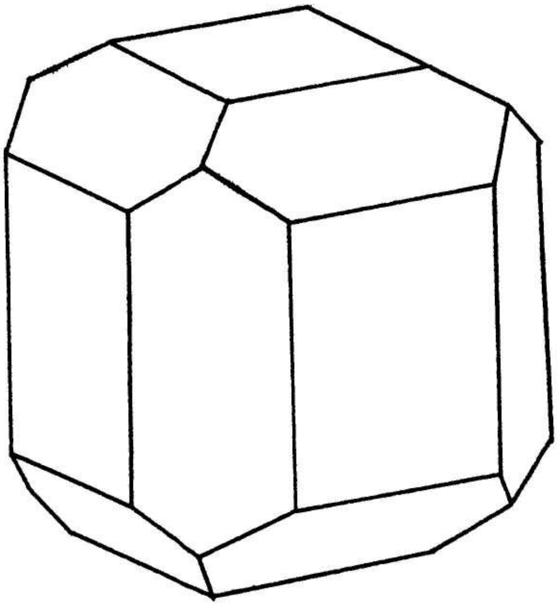

Figure A-3.1 Observed void shape

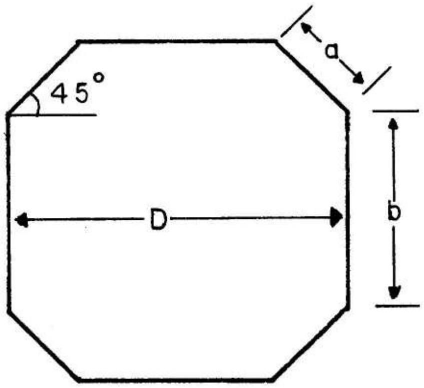

Figure A-3.2 Dimensions for calculations

Again referring to Fig. A-3.2, these steps result in the following expressions:

1. $V_{cube} = D^3$ A-3.6

2. $V_{prism} = b\ a^2/4 = .00943\ D^3$ A-3.7

3. $V_{large\ tetrahedra} = 1/3(a^2/4)((7/18)^{1/2}a) = .0178D^3$ A-3.8

4. The volume of the small tetrahedra is unknown, so the assumption was made that these have half the volume of the large tetrahedra.

The final volume of the void is then:

$$V \approx .816\ D^3$$

resulting in a volume shape factor of:

$$STRFV \cong 1.558$$

These values were used to obtain the correct area and volume for the actual voids.

APPENDIX 4

STATISTICAL CALCULATIONS

The raw data for the void size distribution analysis consisted of 48 size class counts along with the associated dimensions for each. In order to aid the calculations, a computer program was written to reduce the data from micrograph space to sample space and perform the statistical manipulations. The appropriate statistical relations were obtained from statistical analysis textbooks (37, 38).

The first step in the calculation was to reduce the appropriate table of interval centers and limits (depending on the scale chosen) to the sample space by scaling with the magnification. The number of counts in each class was then corrected for surface intersections (as mentioned previously) by the use of the following equation:

$$CN_i = N_i/(1 + IC_i/t) \qquad \text{A-4.1}$$

where the terms are defined in Table A-4.1. The diameters of all voids contained within a given size class were taken as the interval center (IC_i). The cross-sectional area and volume of the voids were calculated in the following way, correcting for the true void shape:

$$A_i = \pi IC_i^2 \text{ (STRFA)} \qquad \text{A-4.2}$$

$$V_i = (4/3) IC_i A_i \text{ (STRFV/STRFA)}$$

The means of the diameter, area and volume were calculated in the standard way:

$$D = \Sigma N_i IC_i / \Sigma N_i \qquad \text{A-4.3}$$

The parameters to describe the shape of the distribution were obtained from the second, third and fourth moments of the curves as follows:

$$\text{Variance} = \Sigma N_i\ (IC_i - \bar{D})^2/\Sigma N_i \qquad \text{A-4.4}$$

$$\text{Standard Deviation} = (\text{Variance})^{1/2} \qquad \text{A-4.5}$$

$$\text{Skewness} = \Sigma N_i (IC_i - \bar{D})^3/\sigma^3 \Sigma N_i \qquad \text{A-4.6}$$

and

$$\text{Kurtosis} = \Sigma N_i (IC_i - \bar{D})^4/\sigma^4 \Sigma N_i \qquad \text{A-4.7}$$

The varance and standard deviation describe the width of the distribution. The skewness refers to the symmetry of the curve. A perfectly symmetrical curve will have a skewness of zero. A positive skewness means that the curve is skewed to the higher values--that is, the tail on the side of the higher values is larger. The kurtosis refers to the size of the tails on the curve. An interesting diagram demonstrating the concept of kurtosis is shown in Fig. A-4.1. A normal distribution possesses a kurtosis of 3.0. These parameters for different distributions yield a measure of the similarity between them. The computer routine outputs a plot showing a corrected histogram and cumulative distribution, along with a normal curve having the same mean and a standard deviation for comparison. The normal curve is given by the following relation:

$$f = (\sigma\sqrt{2\pi})^{-1} \exp(-\tfrac{1}{2}\ (x-\bar{D})^2/\sigma^2) \qquad \text{A-4.8}$$

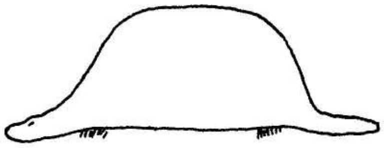

PLATYKURTIC

K<3

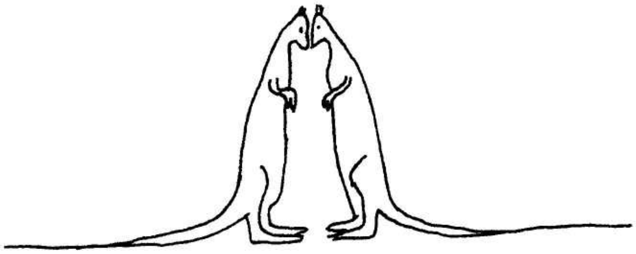

LEPTOKURTIC

K>3

Figure A-4.1 Illustration of kurtosis

(from <u>Principles of Statistics</u>

M.G.Bulmer)

TABLE A-4.1

IDENTIFICATION OF VARIABLES USED IN APPENDIX 4

IC_i	Interval Center
IL_i	Interval Limit
N_i	Number of Counts in i^{th} Class
CN_i	Corrected Number of Counts in i^{th} Class
t	Sample Thickness
A_i	Void Cross-sectional Area
V_i	Void Volume
STRFA	Shape Factor for Area
STRFV	Shape Factor for Volume
r_i	Equivalent Radius - radius of circle contained within the projected area of the void
$\overline{D}$	Mean Void Diameter
σ	Standard Deviation

APPENDIX 5

RESULTS FROM BCC ION EXPERIMENT

A compilation of the results reported by participants in the correlation experiment is given in Table A-5.1. For reasons mentioned previously, only irradiations at 900°C were performed at this site, but other investigators covered the temperature range of 700-1000°C. Although many experimental conditions--dose rate, ion energy, chamber vacuum...--were not constant between the participants, this experiment represents the first attempt to standardize the procedures. Most of the differences in experimental conditions are probably not significant.

As the void volume fraction (swelling) is the parameter of practical interest for reactor design, the swelling vs. ion dose is plotted in Fig. A-5.1. Since most of the lines are based on only two data points, they should not be taken as conclusive, but to indicate trends. The temperature dependence of the void swelling is shown in Fig. A-5.2.

In Fig. A-5.1, the results for 3.2 MeV Mo^{+} and 5MeV Ni^{++} are very close--with .5MeV H^{+} yielding a much higher amount of swelling and 17 MeV Cu^{4+} and 5 MeV Cu^{++} both being appreciably lower. A possible explanation for the lower swelling from copper ion bombardment is given in the discussion section. The swelling vs. temperature curves show a fairly close grouping among the high and low dosage samples (although the high dose 5 MeV Cu^{++} swelling falls near the low dosage curves). From the shapes of the curves, it appears that the peak swelling temperature has not yet been reached.

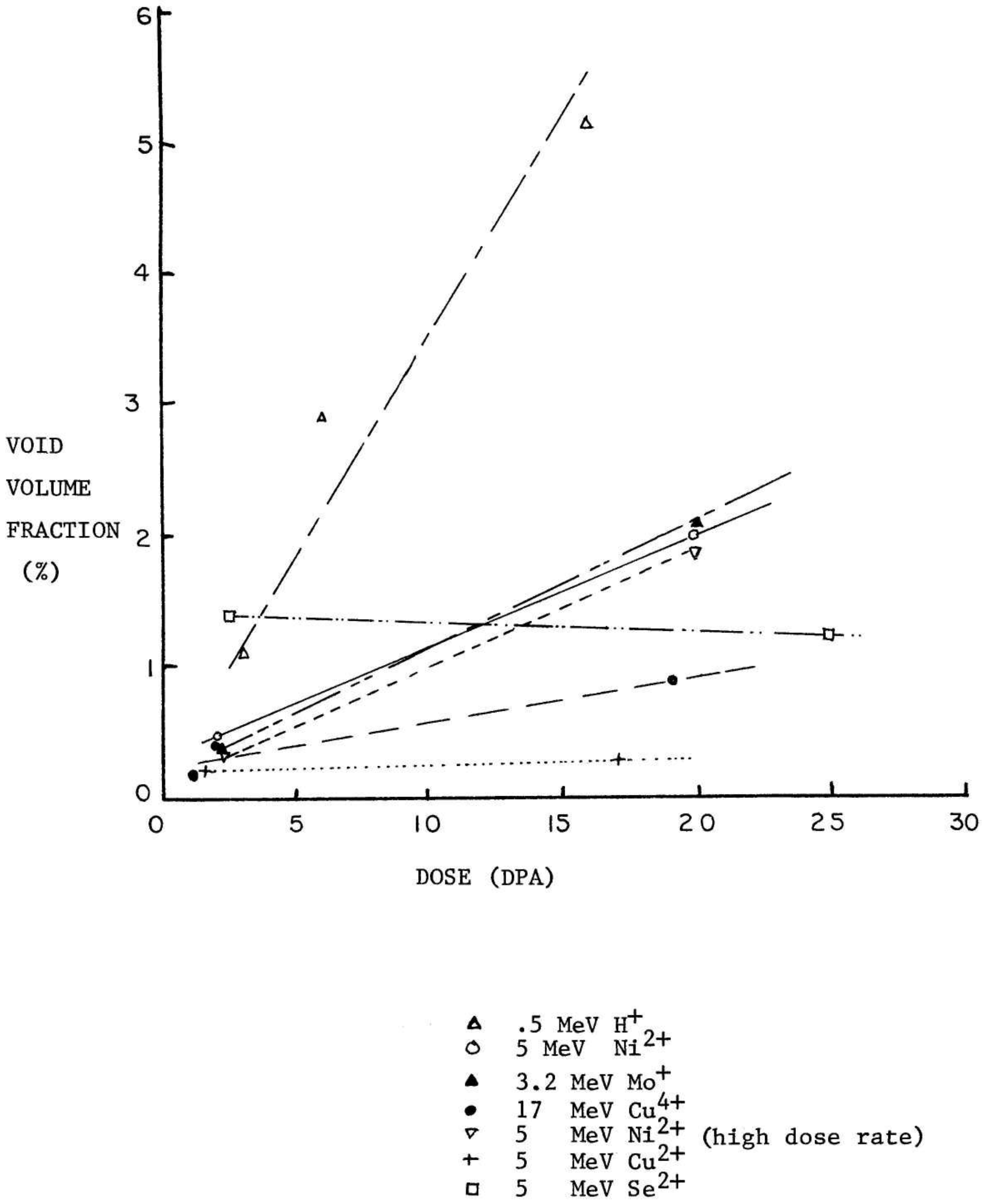

Figure A-5.1 Swelling in Molybdenum at 900°C

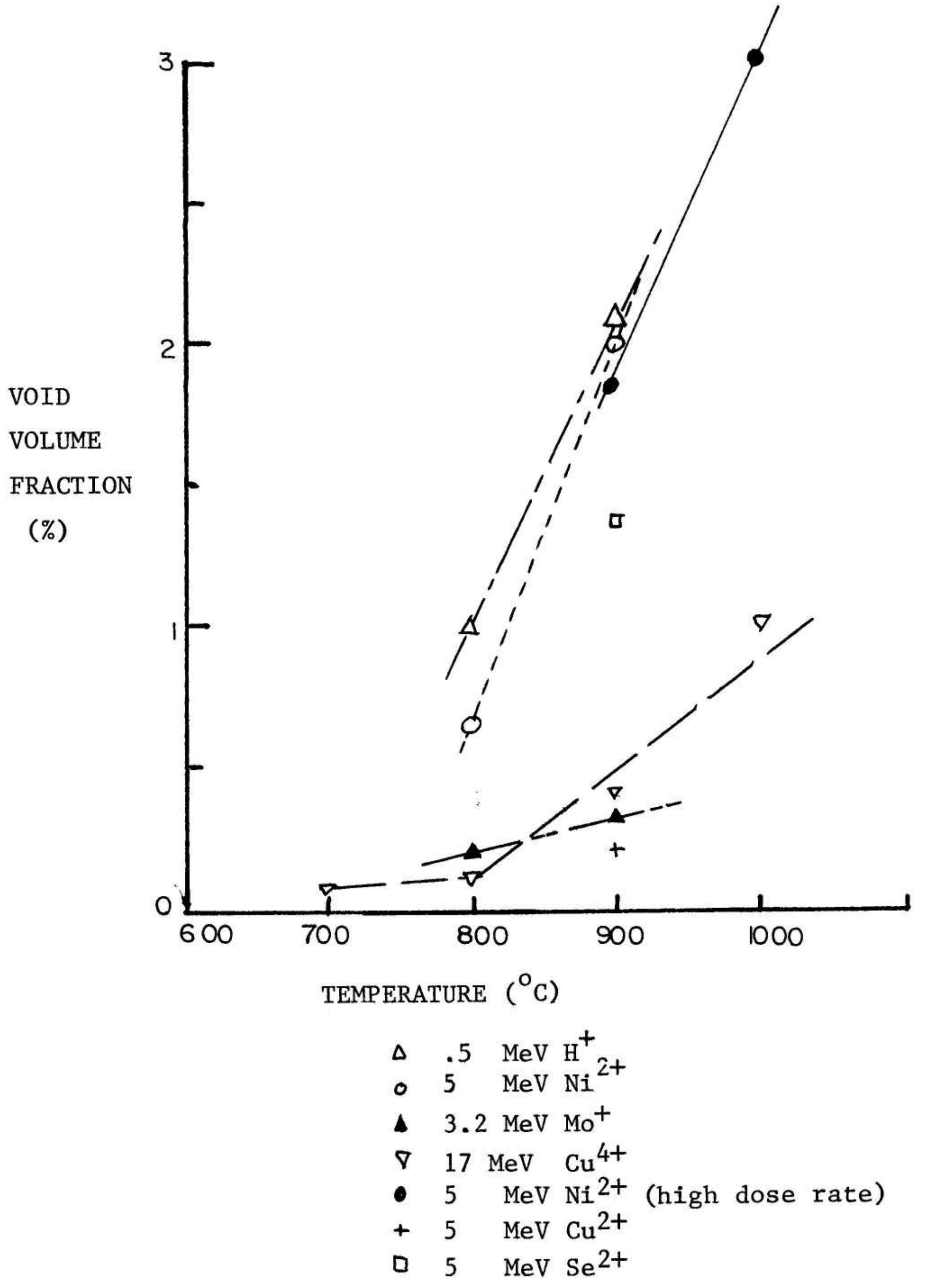

Figure A-5.2 Temperature dependance of swelling in molybdenum

TABLE A-5.1

MICROSTRUCTURAL DATA FROM PARTICIPANTS

IN THE BCC ION CORRELATION STUDY

SITE	T (^{o}C)	ION	ENERGY (MeV)	DOSE (DPA)	DOSE RATE (10^{-3}dpa/s)	$\overline{D}$ (Å)	#DENSITY (10^{22}v/m^3)	V_f (%)	VOID LATTICE PARAMETER (Å)
UWi	700	Cu^{4+}	18.	1.	.4	48	1.	.08	*
PNL	800	Ni^{2+}	5.	20.	3.	44	5.	.65	*
PNL	800	Ni^{2+}	5.	2.	10.	20	low		*
PNL	800	Ni^{2+}	5.	20.	10.	20	low		*
NRL	800	Mo^{+}	2.7	2.	2.5	36	6.1	.2	*
NRL	800	Mo^{+}	2.7	20.	2.5	56	8.1	1.01	310
UWi	800	Cu^{4+}	17.	2.2	.4-.8	44	1.7	.11	340
AI	800	H^{+}	.5	8.	.2	36	48.	1.4	*
AI	800	H^{+}	.5	12.	.2	35	59.	1.4	*
PNL	900	Ni^{2+}	5.	2.	3.	34	9.3	.47	*
PNL	900	Ni^{2+}	5.	20.	3.	54	8.	2.	350
PNL	900	Ni^{2+}	5.	2.	10.	37	4.	.3	*
PNL	900	Ni^{2+}	5.	20.	10.	64	5.	1.85	340
NRL	900	Mo^{+}	3.2	2.	2.5	40	8.2	.34	*
NRL	900	Mo^{+}	3.2	20.	2.5	80	5.8	2.07	350
UWi	900	Cu^{4+}	18.7	1.	.5	78	.6	.17	*
UWi	900	Cu^{4+}	17.	1.9	.4	98	.66	.39	*
UWi	900	Cu^{4+}	17.	19.	.5	75	3.	.87	340
AI	900	H^{+}	.5	3.	.2	140	.6	1.1	*
AI	900	H^{+}	.5	6.	.2	140	1.2	2.9	*
AI	900	H^{+}	.5	16.	.2	170	1.14	5.15	*
MIT	900	Cu^{2+}	5.	1.7	3.3	50	1.8	.24	*
MIT	900	Cu^{2+}	5.	17.	3.3	37	4.5	.26	*
MIT	900	Se^{2+}	5.	2.5	2.4	45	13.	1.38	*
MIT	900	Se^{2+}	5.	25.	2.6	41	16.	1.22	*
PNL	1000	Ni^{2+}	5.	21.	3.	53	2.1	.45	380
PNL	1000	Ni^{2+}	5.	2.	10.	38	9.	.48-.96	400
PNL	1000	Ni^{2+}	5.	20.	10.	64	7.5	3.	400
UWi	1000	Ni^{2+}	18.7	1.3	.5	252	.058	.76	*

* NOT OBSERVED

UWi - University of Wisconsin
PNL - Pacific Northwest Laboratories
NRL - Naval Research Laboratories
AI - Atomics International
MIT - Massachussets Institute of Technology

APPENDIX 6

INITIAL STAGES OF CORRELATION EXPERIMENT

Due to the large amount of judgement by the individual investigator in both the microscopy and void sizing steps of this study, tests were devised to determine the spread in results likely from different sites. As a first step, a common micrograph was circulated to each lab, with the request that the void size distribution parameters be measured. This micrograph is shown in Fig. A-6.1. A compilation of the results is given in Table A-6.1. As can be seen, the reported mean diameter was rather consistent, with a standard deviation of 2.7 Å (mean diameter = 80.8 Å). This was expected, as the only source of difference would be either gross measurement errors or differences in opinion in defining the exact diameter of the voids--both small.

The spread in number density seems to be a bit surprising. At first glance, this parameter would depend solely on the number of voids in the field of view. The differences here are probably due to different identifications of voids (vs. random non-void features) and treatment of voids that intersect either the surfaces or boundaries. The largest variation is in the volume fraction--standard deviation = .18%, mean=2.08%. It seems probable that the a causes of the spread in mean diameter and number density would combine in obtaining this parameter. Considering the spread between the maximum and minimum values, 36%, it is possible that two investigators, when faced with identical distributions, could report different values.

As a further test, a common sample was sent to all participants. This would point out not only the differences in measuring techniques, but

TABLE A-6.1

RESULTS FROM COMMON MICROGRAPH

SITE	VOID DIAMETER (Å)	VOID NUMBER DENSITY $\times 10^{22}$ v/m^3	VOID VOLUME FRACTION (%)	NUMBER OF VOIDS MEASURED
AI	79	5.96	1.96	1840
ANL	82	6.4	2.2	1703
MIT	85	5.6	2.29	1405
NRL	80	5.85	2.07	1664
ORNL	78	6.04	2.04	700
PNL	82	5.91	2.2	600
U.CINN.	77	5.57	1.68	1850
U.WISC.	84	5.86	2.2	
AVERAGE	80.8	5.90	2.08	
STANDARD DEVIATION	2.7	.24	.18	

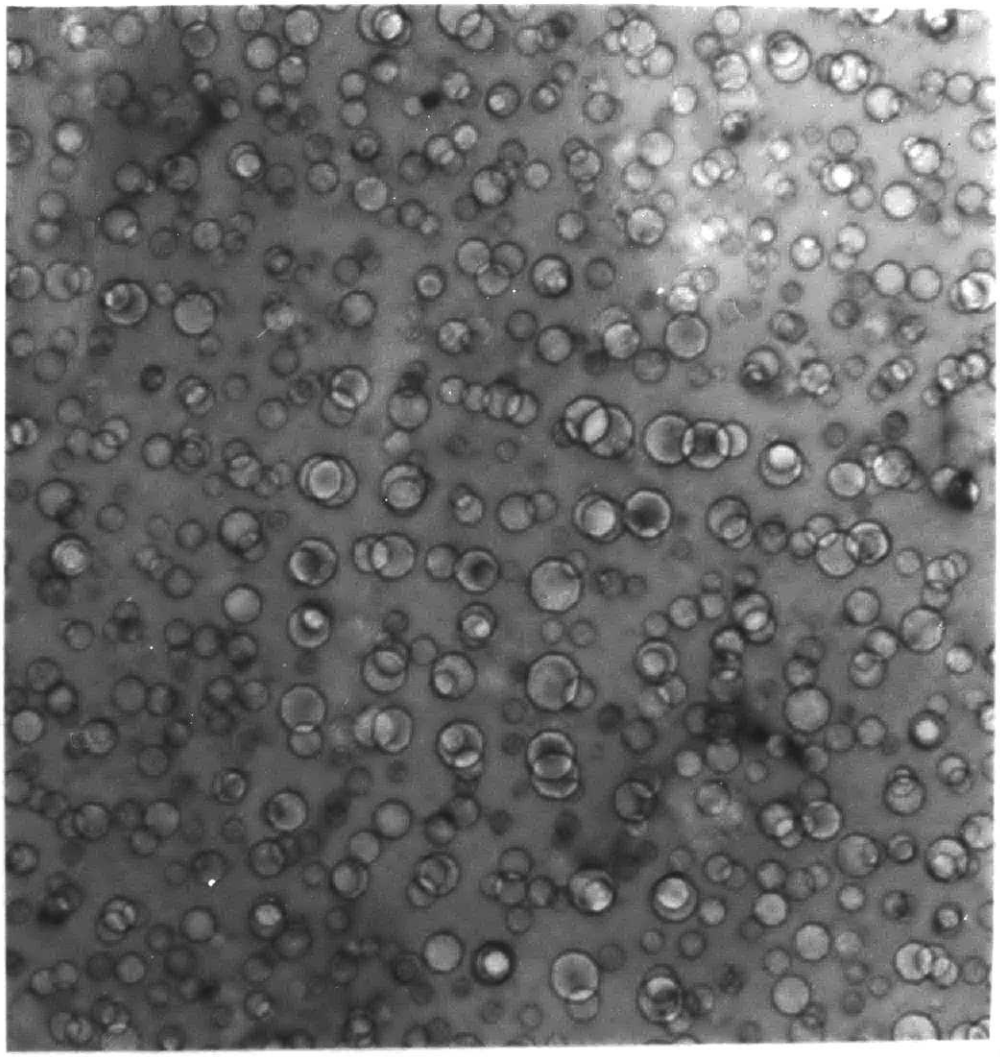

Figure A-6.1 Round robin common micrograph
(Mo ion irradiated molybdenum, magnification = 400kX)

also in microscopy. Surprisingly, the sample deteriorated very little in being shipped to and examined at all of the sites. The results of this stage are summarized in Table A-6.2. As might be expected, the agreement here was worse than previously. The mean diameter had a standard deviation of 6.9 Å, while the standard deviation of the number density is 2.2×10^{22}--corresponding to 33% of the mean value. These parameters reflect not only the previously mentioned errors, but also those due to magnification and inappropriate choice of the areas to be examined. The number density would also show variations due to the different techniques (and inaccuracies) of measuring the foil thickness. The volume fraction, although the standard deviation has doubled from the previous stage, is no longer the parameter in worst agreement.

These results may be looked at as representing the best agreement possible between the different investigators, as they were all examining the same specimen. Based on the spread found in the volume fraction, it is likely that differences in values of 35% or less between two sites are not meaningful.

TABLE A-6.2

RESULTS FROM COMMON SAMPLE

SITE	VOID DIAMETER (Å)	VOID NUMBER DENSITY $\times 10^{22}$ v/m^3	VOID VOLUME FRACTION (%)	VOID LATTICE PARAMETER (Å)
AI	82	4.55	1.74	---
ANL	64	12.0	2.1	---
MIT	83	7.4	2.91	---
NRL	80	5.8	2.06	350
ORNL	87.4	6.04	2.85	375
PNL	84	6.35	2.62	365
U.CINN.	86	4.4	1.75	---
U.WISC.	85	6.4	2.6	355
AVERAGE	81.4	6.61	2.33	3.61
STANDARD DEVIATION	6.9	2.2	.44	6.8

REFERENCES

1. C. Cawthorne & E.J. Fulton,"Voids in Irradiated Stainless Steels," Nature, 216 (1967), 515.
2. D.R. Harris, "The Void Swelling Problem in Sodium Cooled Fast Reactors", AERE-R 7934, p.1
3. P.R. Huebotter and T.R. Bump, "Implications of Metal Swelling in Fast Reactor Design," in Ref. 4.
4. Radiation-Induced Voids in Metals, Ed. J.W. Corbett & L.C. Ianiello, AEC Symposium Series 26, 1972.
5. C.M. Logan, J.D. Anderson and A.K. Mukherjee, "Proton Simulation of Displacement Effects Induced in Metals by 14 MeV Neutrons", J.N.M., 48 (1973), 223.
6. R.S. Nelson, D.J. Mazey and J.A. Hudson, "The Use of Ion Accelerators to Simulate Fast Neutron-Induced Void Swelling in Metals", J.N.M., 37 (1970).
7. D.I.R. Norris, "The Use of the High Voltage Electron Microscope to Simulate Fast Neutron-Induced Void Swelling in Metals," J.N.M., 40 (1971), 66.
8. S.D. Harkness, E.L. Yagee and F.N. Nolfi, "Simulation of In-Reactor Creep of Type 304 Stainless Steel", ANL-7883, January 1972.
9. J.B. Mitchell, C.M. Logan and C.J. Echer, "Comparison of 16 MeV Proton, 14 MeV Neutron and Fission Neutron Damage in Copper," J.N.M., 48 (1973), 139.
10. D.W. Kafer, A.G. Pard, C.G. Rhodes and D. Kramer, "Proton Irradiation Effects in Type 321 Stainless Steel," J.N.M., 39 (1971), 229.

11. C.M. Logan and J.D. Anderson, "Proton Simulation of Displacement Effects Induced in Metals by 14 MeV Neutrons", J.N.M., 48 (1973), 223

12. R.B. Adamson, W.L. Bell and D. Lee, "Use of Ion Bombardment to Study Irradiation Damage in Zirconium Alloys", GE Report #74CRD003, January, 1974.

13. L.T. Chadderton, Radiation Damage in Crystals, Methuen & Co. Ltd., London, 1965.

14. B. T. Kelley, Irradiation Damage to Solids, Pergamon Press, Oxford, 1966.

15. J.A. Brinkman, "On the Nature of Radiation Damage in Metals," Journal of Applied Physics, 25 (1954), 961.

16. J.R. Beeler, "Displacement Spikes in Cubic Metals, I, α-Iron, Copper and Tungsten," Physical Review, 150 (1966), 470.

17. D.I.R. Norris, "Voids in Irradiated Metals," Rad. Eff., 14 (1972), 1.

18. A.D. Brailsford and R. Bullough, "Void Growth and its Relation to Intrinsic Point Defect Properties," in Proc. of the Argonne Conference on "Properties of Atomic Defects in Metals," Oct. 1976.

19. K.C. Russell, "The Theory of Void Nucleation in Metals," Acta. Met. (in print).

20. J.O. Steigler, "Void formation in Neutron-Irradiated Metals," in Ref. 4.

21. S.D. Harkness and Che-Yu Li, in Radiation Damage in Reactor Materials, Vol. 2, IAEA Vienna, 1969, p. 189.

22. H. Wiedersich and J.J. Burton, "Effect of Mobile Helium on Void Nucleation in Materials during Irradiation," J.N.M., 51 (1974), 287.

23. R.S. Nelson and J.A. Hudson, "The Influence of Different Inert Gases on Void Nucleation in Stainless Steel Bombarded by 45.5 MeV Ni 6+ Ions", J.N.M., 58 (1975), 11.

24. A.D. Brailsford and R. Bullough, "The Rate Theory of Swelling Due to Void Growth in Irradiated Metals," J.N.M., 44 (1972), 121.

25. J.L. Straalsund, "The Effect of Cluster Formation on the 'Temperature Shift' for Accelerator Simulation of Neutron Irradiation," J.N.M., 51 (1974), 302.

26. J.L. Brimhall, "Body-Centered Cubic Ion Irradiation Experwment," BNWL-2293/UC-25, 1977.

27. P.B. Hirsch, A. Howie, R.B. Nicholson, D.W. Pashley and M.J. Whelan, Electron Microscopy of Thin Crystals, Plenum Press, New York, 1965.

28. M.R. Rühle, "Transmission Electron Microscopy of Radiation Induced Defects", in Ref. 4.

29. J.A. Sprague, "Interferometric Electropolisher for Controlled Surface Removal", Rev. Sci. Instrum., 46 (1975), 1171.

30. A.E. Feuersanger, "Interference Microscopy of Thin Films and Semiconductor Structures", Solid/State/Design, October 1963.

31. V.A. Phillips, Modern Metallographic Techniques and their Applications, pp. 96-100, Wiley-Interscience, 1971.

32. U.E. Wolff, "Determination of Foil Thickness and Void Size from Electron Micrographs of Irradiated Austenitic Alloys", Metallography, 2 (1969), 89.

33. R.P. Elliott, Constitution of Binary Alloys, 1st supplement.

34. J.H. Evans, R. Bullough and A.M. Stoneham, "The Observation and Theory of the Void Lattice in Molybdenum", in Ref. 4.

35. I. Manning and G.P. Mueller, "Depth Distribution of Energy Deposition by Ion Bombardment," Computer Physics Communications, 7 (1974), 85.

36. D.G. Doran, J.R. Beeler, Jr., N.D. Dudey and M.J. Fluss, "Report of the Working Group on Displacement Models and Procedures for Damage Calculations", HEDL-TME 73-76; UC-79 b, d.

37. R.L. Anderson and T. A. Bancroft, Statistical Theory in Research, McGraw-Hill, 1952.

38. M.G. Bulmer, Principles of Statistics, MIT Press, 1967.

39. J.M. Leitnaker, E.E. Bloom and J.O. Steigler, "The Effect of Minor Constituents on Swelling in Stainless Steel," J.N.M., 49 (1973/74), 57.

40. E.D. Hondros, "Interfacial Energies and Composition in Solids," in Precipitation in Solids, ed. K.C. Russell and H.I. Aaronson, TMS, AIME, N.Y. (in press).

41. K.C. Russell, personal communication.

42. M. Hadji-Mirzai, Masters Thesis, MIT, June 1978.